

INFORMATION TO USERS

This manuscript has been reproduced from the microfilm master. UMI films the text directly from the original or copy submitted. Thus, some thesis and dissertation copies are in typewriter face, while others may be from any type of computer printer.

The quality of this reproduction is dependent upon the quality of the copy submitted. Broken or indistinct print, colored or poor quality illustrations and photographs, print bleedthrough, substandard margins, and improper alignment can adversely affect reproduction.

In the unlikely event that the author did not send UMI a complete manuscript and there are missing pages, these will be noted. Also, if unauthorized copyright material had to be removed, a note will indicate the deletion.

Oversize materials (e.g., maps, drawings, charts) are reproduced by sectioning the original, beginning at the upper left-hand corner and continuing from left to right in equal sections with small overlaps. Each original is also photographed in one exposure and is included in reduced form at the back of the book.

Photographs included in the original manuscript have been reproduced xerographically in this copy. Higher quality 6" x 9" black and white photographic prints are available for any photographs or illustrations appearing in this copy for an additional charge. Contact UMI directly to order.

UMI

A Bell & Howell Information Company
300 North Zeeb Road, Ann Arbor MI 48106-1346 USA
313/761-4700 800/521-0600

Seismic Velocity Structure of the Puget Sound Region from

3-D

Non-Linear Tomography

by

Neill Symons

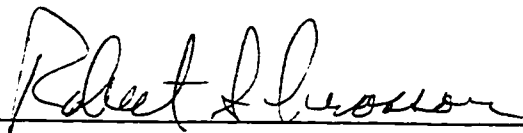
A dissertation submitted in partial fulfillment of
the requirements for the degree of

Doctor of Philosophy

University of Washington

1998

Approved by



(Chairperson of Supervisory Committee)

Program Authorized

to Offer Degree Geophysics Program

Date October 21, 1998

UMI Number: 9916727

**Copyright 1998 by
Symons, Neill Philip**

All rights reserved.

**UMI Microform 9916727
Copyright 1999, by UMI Company. All rights reserved.**

**This microform edition is protected against unauthorized
copying under Title 17, United States Code.**

UMI
300 North Zeeb Road
Ann Arbor, MI 48103

**©Copyright 1998
Neill P. Symons**

In presenting this dissertation in partial fulfillment of the requirements for the Doctoral degree at the University of Washington, I agree that the Library shall make its copies freely available for inspection. I further agree that extensive copying of this dissertation is allowable only for scholarly purposes, consistent with "fair use" as prescribed in the U.S. Copyright Law. Requests for copying or reproduction of this dissertation may be referred to University Microfilms, 1490 Eisenhower Place, P.O. Box 975, Ann Arbor, MI 48106, to whom the author has granted "the right to reproduce and sell (a) copies of the manuscript in microform and/or (b) printed copies of the manuscript made from microform."

Signature Neill Brown

Date 10/20/98

University of Washington

Abstract

Seismic Velocity Structure of the Puget Sound Region from 3-D
Non-Linear Tomography

by Neill Symons

Chairperson of Supervisory Committee: *Professor Robert S. Crosson*
Geophysics Program

In this dissertation I describe a non-linear seismic tomography experiment in the Greater Puget Sound Region (GPSR). The GPSR contains portions of three distinct geologic provinces: (1) the Coast Range Province—composed of the Olympic Mountains and the Siletzia terrane lying along the Washington Coast (the western edge of the GPSR). (2) The Puget Lowland—an approximately linear depression that stretches from Oregon's Willamette Valley to the Strait of Georgia in Canada. The Puget Lowland lies in the middle of the GPSR. (3) The Cascade Range—lying along the eastern edge of the GPSR and characterized by extensive episodic volcanism since the later Mesozoic.

The result of this study is a three-dimensional model of the P-wave velocity within the GPSR. Interpretation of this model provides information about the subsurface geology in the region. The method used to perform the tomography has been developed as part of this research. The method uses a finite-difference algorithm to calculate seismic travel-times to every point in the region using the full 3-d velocity model. The method is capable of using three different types of data: (1) earthquakes with unknown hypocenters. The earthquake hypocenters are found as part of the

model during solution of the tomography problem. (2) Explosions or other seismic events with known locations. (3) External data constraining the seismic velocity at known locations within the model.

There is a good correlation between the velocity model derived in this experiment and several known geologic structures in the GPSR, including: the core of the Olympic Mountains; high seismic velocity where the basalt that makes up the Siletzia terrane outcrops; and low-velocity regions at basins under the cities of Seattle, Tacoma, Everett, and Chehalis. The data provides sufficient resolution to delineate the geometry of the contacts between these units within a large portion of the GPSR.

TABLE OF CONTENTS

List of Figures	iv
List of Tables	vii
Chapter 1: Introduction	1
1.1 Motivation for this Study	1
1.2 Seismic Hazards	2
1.3 Pacific Northwest Tectonics and Northwest Washington Regional Geology	4
1.4 Previous Regional Velocity Studies	10
1.5 Why This Study is Needed	13
Chapter 2: Method of Analysis	19
2.1 Introduction	19
2.2 Seismology Background	19
2.3 Travel-time Calculation	22
2.4 Example 1: Geiger's Method of Earthquake Location	24
2.5 Non-Linear 3-D Seismic Tomography	29
2.6 Resolution	42
2.7 Error Analysis	43
Chapter 3: Data	57
3.1 Seismic Data	57

3.2	Explosions	63
3.3	External Constraints	64
Chapter 4:	Tomographic Inversion	69
4.1	Inversion Parameters	69
4.2	Comparison of Data Sets	75
4.3	Results	76
4.4	Error Analysis of the Final Model	77
Chapter 5:	Interpretation of Results	94
5.1	Coast Range	94
5.2	Puget Lowland	97
5.3	Subducted Slab	98
5.4	Comparison With Previous Studies	99
5.5	Hypocenter Relocations	99
5.6	Summary	100
Chapter 6:	Additional Data from the SHIPS Experiment	106
6.1	Marine Phase of SHIPS	106
6.2	Data	107
6.3	Stacking	107
6.4	Sample Stack	111
6.5	Selection of Data to Stack	111
Chapter 7:	Velocity Inversion Using SHIPS Data	128
7.1	Resolution	128
7.2	Geologic Interpretation	129

Chapter 8: Conclusions	142
8.1 Data	142
8.2 Features of the Model	144
8.3 Future Work	146
Bibliography	148
Appendix A: Finite-Difference Travel-Time Calculations	159
Appendix B: Pseudo-code for Non-linear Seismic Tomography Using Finite-Difference Travel-times	165
Appendix C: Puget Lowland Seismograph Stations	166
Pocket Material: Maps and Cross Sections Through Final Model	

LIST OF FIGURES

1.1	Study Area Map	15
1.2	Schematic of Juan de Fuca Subduction Zone	16
1.3	Tectonic Map	17
1.4	Geology of the GPSR	18
2.1	Ray-Path Examples	47
2.2	Example Travel-time Curves	48
2.3	Three Travel-time Calculation Methods	49
2.4	Linear Tomography Problem	50
2.5	Illustration of Model Discretization	51
2.6	Mountain Analogy	52
2.7	Travel Times with Ray	53
2.8	Fourier Transform of Laplacian	54
2.9	Complete Matrix Equation	55
2.10	Example Double Minima	56
3.1	Study Area Map	66
3.2	Earthquake Spatial Variance	67
3.3	Comparison of Sampling	68
4.1	Inverted 1-D starting model	81
4.2	Tradeoff Curve	82
4.3	Distribution of Residuals by Station	83

4.4	Comparison of Checkerboard for Full and Reduced Dataset	84
4.5	Comparison of Checkerboard with Proportional Noise	85
4.6	Results of Tomographic Inversion	86
4.7	Checkerboard Test	88
4.8	Jackknife Test	90
4.9	Dependence on Starting Model	92
4.10	Dependence on Starting Model (Differences)	93
5.1	Cross Sections Through the Final Model	101
5.2	Cross Sections Through Checkerboard Test	102
5.3	GPSR Geology	103
5.4	Mechanical Model of the Olympic-Crescent System	104
5.5	CDS Hypocenter Comparison	105
6.1	RV Thomas Thompson	114
6.2	Thompson Track Map	115
6.3	Strong SHIPS Signal	116
6.4	Stacking Example	117
6.5	Example of Straight Stack	118
6.6	Time Offset Across a Single Stack	119
6.7	Example of Slant Stack	120
6.8	Spectral Analysis of Good Arrival	121
6.9	Comparison of Filtered and Un-filtered Stack	122
6.10	Schematic of Stack Water Projection	123
6.11	Example Stack	124
6.12	Map of SHIPS Stack Locations	125
6.13	Best SHIPS Stack	126

6.14 Worst SHIPS Stack	127
7.1 Hit Count Comparison	136
7.2 High Resolution Checkerboard	137
7.3 Interpretations in the Center of the GPSR	138
7.4 Geometry of the Crescent Backstop	139
7.5 Geometry of the Crescent Backstop	140
7.6 Resolution Kernel Test for Seattle and Tacoma	141
A.1 Pictorial Representation of Huygen's Principle	163
A.2 Expansion of the Box in FDTT Calculation	164

LIST OF TABLES

1.1	Ps2 1-D Velocity Model	10
3.1	Declustered Puget Sound Earthquakes	62
3.2	Comparison of the residuals between different data sets using different location methods.	62
3.3	Summary of Puget Sound Explosions	64
4.1	Inverted 1-D Velocity Model	72
5.1	Summary of Rock Velocities from <i>Christensen and Mooney</i> [1995] . .	95
6.1	Summary of SHIPS stacks	112
C.1	Seismic Tomography Pseudo-code	166
D.1	Puget Lowland Seismograph Stations	168

ACKNOWLEDGMENTS

There are many people without whom it would not have been possible for me to have completed this research. I would like to take this opportunity to acknowledge some of these contributions. First, I would like to thank my advisor Robert Crosson, both for his advice on the methods and interpretation developed here and for patiently reading the early drafts of this dissertation. I would like to thank my committee, Jonathan Lees, John Booker, Steve Malone and Eric Kunze. In addition to serving on my committee I would like to thank Jonathan Lees for developing the xmap8 program with which many of the figures in this dissertation were produced. Many conversations with Ken Creager have been helpful in formulating the interpretation of this data. I am grateful to Ruth Ludwin who read and helped me to greatly improve the initial draft of this dissertation. I would like to thank my office mates George Thomas and Shawn Dewberry for their companionship in graduate school. There are a large number of people responsible for gathering the data used in this experiment, I would like to offer special thanks to Steve Malone, Pete Lombard, Ruth Ludwin, Sandro Coso, and Bill Steele for maintaining the PNSN. Siting of the stations for the SHIPS experiment was performed by Tom Yelin, Bob Norris, and George Thomas. Conversations with Tom Pratt and Craig Weaver helped me to understand the complicated tectonics of the Puget Sound Region. Conversations with Martyn Unsworth and Ron Merrill helped me understand important factors about graduate studies outside of scientific

research.

Graduate school is a stressful time and I am grateful to the members of the University Kayak Club for helping me to blow off steam occasionally. I would especially like to thank Ed Mulligan, Pete Matson, and Mitch Kaplan for pulling me out of the river when I “fell” out my boat on more than one occasion.

Finally, I would like to thank my wife Tamara who has not only supported me with love and friendship through my graduate career, but has also put up with me during the completion of this dissertation.

Chapter 1

INTRODUCTION

1.1 Motivation for this Study

Several studies in the past 10 years have lead to a greatly increased concern over the seismic hazards faced in the Pacific Northwest. For instance *Bucknam et al.* [1992] and *Satake* [1996] provide evidence for, respectively, a large Seattle crustal earthquake (estimated magnitude greater than or equal to 7) approximately 1100 *years* ago and a large Cascadia subduction zone earthquake (estimated magnitude 9) about 300 *years* ago. To understand and prepare for a large earthquake in the Pacific Northwest we require an improvement in at least two areas of knowledge. First, we need better tectonic models to assess where and when an earthquake is most likely to occur. And second, we need better models for the geology of the subsurface to determine the specific portions of the region that will be the most susceptible to damage when an earthquake does occur.

This study is concentrated on a rectangular region from latitude $46.15^{\circ}N$ to $48.80^{\circ}N$, longitude $121.35^{\circ}W$ to $124.00^{\circ}W$, and from 0 to 60 *km* in depth (figure 1.1). For the remainder of this thesis I will refer to the entire study area as the Greater Puget Sound Region (GPSR). Eight of Washington's ten largest cities are contained within the GPSR with a total population of approximately three million people.

In this study I use seismic tomography to generate a three-dimensional model of the seismic P-wave velocity within the study area. Interpretation of this model provides information about the subsurface geology. Once we know the geology it is

possible to evaluate proposed tectonic models for the region.

1.2 Seismic Hazards

The study region lies to the east of a major tectonic boundary. The Juan de Fuca plate is subducting under the North American plate. There are three major types of earthquakes which present a risk within the GPSR (figure 1.2). First, a subduction zone earthquake: paleo-earthquake studies based on buried tree stumps near the Washington coast and analysis of tsunami records suggests that there was a great subduction zone earthquake from the Juan de Fuca plate in January 1700. This earthquake is estimated to have a magnitude of 9 [Satake, 1996] which would correspond to a rupture of the entire length of the zone; from Cape Mendicino to southern British Columbia. Earthquakes of this size have an estimated recurrence interval of 300-600 years [Atwater, 1996] in this subduction zone, so, another such earthquake could occur at any time.

A second type of earthquake is also related to the subduction zone. These are earthquakes that occur in the Benioff zone (within the subducted slab). This type of earthquake has already occurred several times in this century. Most notably, there was a 7.1 M_c under Olympia in 1949 and a 6.5 M_c under Tacoma in 1965 [Thorsen, 1986]. These events occurred within the descending slab at depths of approximately 45 km. Although these events are much smaller than rupture of the entire subduction zone they present a significant hazard since they may be more frequent and are closer to the population centers in the Puget Sound.

The third type of earthquake hazard in the GPSR is produced by crustal earthquakes. There has been only one crustal earthquake estimated to be over magnitude 6 in historical times, the 1872 North Cascades event [Malone and Bor, 1979; Ludwin et al., 1991]. Since the fault dimensions are likely to be more limited in the crust, the maximum magnitude of type this of earthquake is probably smaller than for a

subduction zone event. However, the epicenter could be much closer to populated areas. Because of heavy deposits of glacial overburden, few, if any, faults can be identified in this region from surface geology so geophysical techniques are required.

An example of this is the Seattle Fault which was first postulated based on large gravity and magnetic anomalies but has now been imaged on several seismic reflection surveys [e.g. *Pratt et al.*, 1997]. The trace of the Seattle fault runs through downtown Seattle and follows Interstate 90 to at least Lake Sammamish. This fault is believed to be responsible for an earthquake with an estimated magnitude of 7.4 which generated a tsunami in the Puget Sound ~ 1100 years ago [*Atwater*, 1992].

South of the GPSR, there are distinct bands of crustal earthquakes near to Mount Saint Helens and west of Mount Rainier; however, in the central GPSR the seismicity is dispersed in an arcuate pattern (when viewed in an east-west cross section) down to a depth of ~ 30 km (figure 1.1). There is a gradual termination of seismicity on the eastern edge of the arc and a more abrupt termination to the west. The crustal earthquakes in the Puget Lowland do not appear to be oriented along distinct fault zones (figure 1.1).

Another geologic hazard related to crustal earthquakes in the GPSR is volcanism. Although the study area contains only one major strato-volcano (Mount Rainier), there are two others (Mount Saint Helens, and Glacier Peak) just outside the boundaries. Although any of these volcanos is capable of producing a moderate earthquake, which could cause damage in the nearby populated areas, the primary hazard is a catastrophic mud-flow. The 1980 eruption of Mount Saint Helens is a good example of the type of damage expected from a large mud-flow. After the eruption a mud flow down the Toutle River reached as far as the Columbia River where it silted up and temporarily closed the Port of Portland (a distance of ~ 100 km).

1.3 Pacific Northwest Tectonics and Northwest Washington Regional Geology

1.3.1 Regional Plate Tectonics

To quote from *Duncan and Kulm* [1989], “The geological development of the Pacific Northwest from earliest Tertiary time to the present has been dominated by the effects of plate convergence.” At present subduction occurs at $3.5-5 \frac{\text{cm}}{\text{year}}$ [*Engelbretson et al.*, 1985] along the Juan de Fuca-Gorda-Explorer plate system which extends from the Mendicino triple junction to the Queen Charlotte transform fault [*Riddihough*, 1984] (figure 1.3 A); the Juan de Fuca plate is flanked on the north by the smaller Explorer plate to the north and the Gorda plate on the the south.

There are 3 major characteristics of the Juan de Fuca subduction system that make it unusual. (1) There are virtually no earthquakes deeper than 100 km associated with the subducting slab nor are there earthquakes in the toe of the slab shallower than 20 km (figure 1.1). This is probably related to the fact that (2) the spreading ridge is very close (150 – 300 km) to the subduction zone; as a result the subducted slab is hot, buoyant, and thin. This is also the reason for the relatively shallow subduction angle of about 11° [*Crosson and Owens*, 1987]. (3) There is almost no expression of a trench; high sedimentation rates fill any trench that would exist [*Duncan and Kulm*, 1989].

The present day Juan de Fuca plate is only a small remnant of the larger Farallon plate which, 65 Ma, is thought to have extended from the present day Pacific Northwest to Mexico [*Atwater*, 1970] (figure 1.3 B). At 65 Ma it is also thought that the Kula plate subducted along the upper portion of North America from the Pacific Northwest to Alaska. There was a triple junction east of the Pacific Northwest between the Farallon, Kula, and the Pacific plates. Over time the Kula plate was entirely subducted (Kula means “all gone”) and the southern portion of the Farallon plate was subducted beneath California forming the San Andreas fault system [*At-*

water, 1970]. The breakup of the Farralon plate is still ongoing: the Explorer plate is believed to have split off the Juan de Fuca plate along the Nootka fault about 4 Ma; the Gorda plate only shows evidence for motion independent from the Juan de Fuca plate for 3 Ma [Riddihough, 1984].

1.3.2 Regional Geology

Geologically the study area contains parts of three major physiographic provinces: from west to east; the Coast Range, the Puget Lowland, and the Cascade Range (figure 1.4). The geology of the Pacific Northwest is complicated for a number of reasons. First, the Coast Range, the Cascade Range and the underlying bedrock in the Puget Lowland comprise of accreted terranes brought in on the subducting slab according to interpretations by *Duncan* [1982] and *Wells et al.* [1984]. The relationships between the different terranes are complex and difficult to decipher. Second, large areas of the surface are covered by young sediment. Rapid uplift of the Cascade and Olympic Mountains provides a good source of sediments. Furthermore, several continental glaciations have deposited a heavy layer of glacial sediment. In most of the GPSR heavy sedimentary cover completely covers the bedrock and leaves little evidence of the underlying geology to be found on the surface [*Hall and Othberg*, 1974]. In the central portion of the GPSR, the Puget Lowland, this sediment has been mapped to a depth of several kilometers.

In the next section, will describe the three major units out of geographic order. First the western portion, the Coast Range; then a jump to the eastern portion, or the Cascade Range; and finally the middle unit, the Puget Lowland. Sediment blanketing the Puget Lowland conceals the contact between the other two units; in fact it is not clearly known if the basement underlying the Puget Lowland is from the Coast Range, the Cascade Range, or another unique unit.

Coast Range

Starting at the coastline and moving inland west to east, the first geologic province is the Coast Range. The Coast Range can be further divided into two distinct geologic terranes, the core rocks of the Olympic Mountains and the Siletzia terrane [Babcock *et al.*, 1992]. The core rocks of the Olympic mountains comprise an accretionary wedge of material scraped off the down-going Juan de Fuca slab. The Olympic core is composed of melange and heavily faulted marine sedimentary rocks. It also contains some minor pillow basalts that have been metamorphosed to prehnite-pumpellyite and greenschist facies [Tabor, 1987]. Siletzia is a thick sequence of basalt known as the Crescent Formation where it outcrops on the eastern edge of the Olympic Mountains (fig 1.4), as the Siletz River Volcanics in Northwestern Oregon, and as the Metchosin Volcanics in southern British Columbia [Snavely and Baldwin, 1948; Duncan and Kulm, 1989; Tabor and Cady, 1978].

Duncan and Kulm [1989] have estimated a total volume of approximately 250,000 km³ for the Siletzia terrane, roughly 5 times the volume of the island of Hawaii. Furthermore, Babcock *et al.* [1992] have measured a composite section in the Crescent Formation with a total depth of 16.2 km which contains no geologically detectable faults or folds. Observations of fore-arc deformation suggest that crustal strength may be heavily dependent on the thickness of the Siletzia terrane [Trehu *et al.*, 1994] making the configuration of this unit an important factor in seismic hazard.

The section of the Crescent formation (Siletzia) measured by Babcock *et al.* [1992] is composed of two units. The lower unit is 8.4 km of pillowed to massive submarine basalts. There are inter-beds of basaltic sandstone, siltstone, and conglomerate, with minor turbidites, Hyaloclastites, and fossiliferous limestones. The inter-beds contain clasts, up to 3 m in diameter, of quartz diorite Cady [1975]. This indicates a close proximity to North America at the time of the basalt extrusion. The bottom of the lower unit is inter-bedded, in places, with the underlying terrigenous Blue Mountain

unit. The upper unit is 7.8 km of sub-aerial flows, mostly columnar to randomly jointed. With sills and occasional dikes. There are inter-beds of basaltic breccia, sandstone, and siltstone, with minor foraminiferal limestone

There are two competing hypothesis for the origin of Siletzia. *Babcock et al.* [1992] argue that the terrane formed *in situ* due to rupture of the down-going Farralon slab. They note that plate motion reconstructions rule out formation of the terrane on either the Farralon or the Kula plates. Furthermore, their palomagnetic measurements show that the terrane has not been significantly rotated or translated since formation. Alternatively, *Duncan and Kulm* [1989] expand on the idea originally proposed by *Snively et al.* [1968] that this formation originated as a chain of islands and seamounts. If so, the presence of sedimentary inter-beds indicates that this must have taken place close to the North American continent. They cite petrological, geochemical, geochronological, and field studies which indicate a decrease in the age of the formation from the east to the west from 62 to 48 Ma [*Duncan*, 1982]. This indicates progressive eruption and accretion of the islands or seamounts to North America. They also cite paloemagnetic evidence for large clockwise rotations of 35 – 70° [*Simpson and Cox*, 1977; *Wells and Coe*, 1985] which are not consistent with the complex forming in place. The volcanism could have been the product of the Yellowstone hotspot either coincident with a segment of the Kula-Farralon plate boundary [*Duncan*, 1982]; or during reorganizations of the spreading geometry [*Wells et al.*, 1984]; or behind the trench in the wake of oblique rifting of the continental margin [*Moore et al.*, 1983].

Tabor and Cady [1978] describe the western edge of the Crescent formation in the Olympic Mountains to be steeply dipping to the east where Tertiary marine sedimentary rocks are thrust below the Siletz terrane. The resulting uplift is estimated by *Brandon and Calderwood* [1990] to be about 10 km. At the eastern edge of the Olympic Peninsula the Siletz terrane contacts the pre-Tertiary crystalline and metamorphic rocks which make up the base of the Puget Sound region [*MacQueen*,

1982]. The contact is covered by a thick layer of glacial sediments [Hall and Othberg, 1974] but there is some constraint on the location from the magnetic data of Stanley *et al.* [1992] and the gravity data of Bonini *et al.* [1974] and Finn [1990].

Cascade Range

The eastern portion of the study area lies on the western flank of the Cascade Mountain Range where volcanics of late Mesozoic to Holocene age over-lie a pre-Tertiary basement of varied composition. The basement rocks include metamorphic, igneous, and sedimentary rocks from several exotic crustal terranes [Tabor, 1994]. Accretion of the Cascade basement was complete by late Cretaceous or earliest Tertiary, after which these rocks formed the stable framework of the Pacific Northwest margin. Johnson [1985] describes episodes of significant strike-slip and transtensional deformation in the Cascade basement during the early to early-middle Tertiary. The present period of extensive episodic volcanism began during the later Mesozoic [McBirney, 1978]. A thick layer of volcanic rocks dating from the late Eocene or Oligocene to the present [Stanley, 1984] over-lie the basement. There are a number of exposed plutons near Mount Rainier [Cowan and Potter, 1986; Walsh, 1987] and also near Mount St. Helens [Everts *et al.*, 1987].

Puget Lowland

The Puget Lowland is the low-lying region in central western Washington between the Coast Range and the Cascade Range. This depression is the northern part of a generally north-south lowland that is almost linear and stretches from Oregon's Willamette Valley to the Strait of Georgia in Canada [Johnson *et al.*, 1996]. The Puget Lowland includes the waterways of the Puget Sound and the major population concentration within the GPSR. Because the underlying bedrock is covered by a thick layer of late Tertiary and Quaternary sediment, heavy urban development,

and numerous large waterways it is difficult to ascertain the location of the contact between the Coast Range province to the west and the Cascade province to the east.

A number of recent papers [e.g. *Johnson*, 1984; *Johnson et al.*, 1996; *Pratt et al.*, 1997] have advanced the idea that the Puget Lowland is a long narrow thrust sheet being pushed to the north. Basins filled with thicker than "normal" accumulations of sediment under the cities of Chehalis, Olympia, Tacoma, and Seattle are bounded either by antiforms or thrust faults that form as the thrust sheet is compressed [*Johnson*, 1985; *Pratt et al.*, 1997]. This is consistent with the north-south major axis of compression which predominates in crustal earthquakes in the region [*Ma et al.*, 1996].

According to *Johnson* [1984, 1985], the Puget Lowland is a long narrow thrust sheet that lies between the right lateral fault system along the western edge of the Cascade Range (possibly the Straight Creek Fault in figure 1.4) and the right lateral fault system along the eastern edge of the Olympic Range (Puget Fault in figure 1.4). *Johnson* [1984] hypothesizes a right-lateral transcurrent fault which truncates the former western margin of North America under the Puget Lowland. This fault is a continuation of the west trending San Juan and the northwest trending Survey Mountain faults on southern Vancouver Island. These are the faults that separate the Metchosin formation (the Canadian name for Siletzia) from the rest of Vancouver Island. Therefore, it is assumed that the continuation of these faults would separate the Crescent formation (Crescent is the Olympic Peninsula name for Siletzia) from the basement under the Puget Lowland. Slightly to the east there is right-lateral motion along another large strike-slip fault system which includes the Straight Creek fault, the Entiat-Levenworth fault system and the hypothesized Puget fault [*Johnson*, 1985].

In Washington, the northern end of the thrust sheet may lie at the southern Whidbey Island fault zone (SWIF) [*Johnson et al.*, 1996]. This structure could serve as a step-over zone connecting the eastern and the western right lateral faults, terminating the block caught between these two fault systems (the Puget Lowland).

Kinematically the thrust sheet hypothesis can be explained as a block of crustal material caught between two right lateral fault systems, with the fault to the west moving faster than the fault to the east. If the sliver ends at a strong backstop, the SWIF, then the material to the south starts to pile up near the backstop (much like a train wreck). Dynamically it is still unclear what drives the right lateral motion. However, *Wang* [1996] has modeled subduction zones with oblique convergence and buttressed ends (such as this one). The results of *Wang* [1996] indicate that margin parallel compressive stress increases toward the fixed end of the fore-arc sliver. This is consistent with kinematic model for the northwestern portion of the U.S. coast advanced by *Wells et al.* [1998].

There is a right lateral oblique component to the subduction of the Juan de Fuca slab, but it unclear how the margin-parallel stress could be transmitted into North America without also transmitting the margin-perpendicular stress.

1.4 Previous Regional Velocity Studies

1.4.1 1-D Models

It was recognized in early structure studies by *Neumann* [1957] that an accurate crustal structure model was necessary for good earthquake locations in western Washington; although *Neumann* [1957] recognized that crustal thickness was greater than “normal” in western Washington; his results were inconclusive with only limited observational data. Crustal and sub-crustal earthquakes were used by *Crosson* [1976a, b] in a formal joint hypocenter/station correction/velocity model inversion to estimate a one-dimensional (1-D) crustal structure model. This model has a 40km thick crust and a small low velocity zone near the base of the crust (Table 1.1). A derivative of this model is still used for routine (PNSN) earthquake locations in the Puget Sound region.

Table 1.1: Ps2 1-D Velocity Model

Depth km	P-Velocity $\frac{km}{sec}$	S-Velocity $\frac{km}{sec}$
0.0	5.40	3.07
4.0	6.38	3.63
9.0	6.59	3.75
16.0	6.73	3.83
20.0	6.86	3.90
25.0	6.95	3.95
32.0	6.90	3.93
41.0	7.80	4.44

1.4.2 Previous Tomography

The Puget lowland has been the subject of several previous seismic velocity studies. *Lees and Crosson* [1989] performed a one step linear tomographic study. The linear tomographic inversion is limited by the assumption of source locations and ray-paths that are obtained with the 1-D velocity model. Nevertheless, this initial study indicated that large 3-D velocity variations exist in the Puget lowland and can be correlated with local geological structure. For example, the results suggest that the Crescent terrane (Siletzia) persists to a depth of between 10 to 20 km and forms the basement beneath the central basin.

More recently, the study region of *Moran* [1995] (figure 1.1) extends as far north as the city of Seattle. This is a non-linear tomographic inversion utilizing the method of *Lees and Crosson* [1989], but modified to find rays through the perturbed model using the ray bending technique of *Um and Thurber* [1987]. However, the Puget Lowland is on the edge of *Moran* [1995] region, and tomography studies typically have poor resolution near the edges. Work in the Puget Sound region by *Stanley* [1996] and *Villasenor* [1996] is at a lower resolution (larger spatial area) than this study, and is also limited by the inclusion of some earthquakes of low quality.

1.4.3 Refraction and Reflection Lines

The Puget Sound region has also been the target of several active and passive reflection and refraction studies aimed at determining the crustal structure. Early work by *Spence et al.* [1985] off the Southern tip of Vancouver island was unable to image the subducting slab, but did provide controls on the dip of oceanic crust and the distance at which subduction begins in this region, as well as constraining the velocity gradient beneath the oceanic Moho and the depth of the continental Moho. A later study by *Tabor and Lewis* [1986] showed a similar result for the dip of the plate off the Washington coast and a similar velocity gradient beneath the oceanic Moho although it was unable to detect the continental Moho, possibly due to a less distinct transition. *Johnson et al.* [1994, 1996] and *Pratt et al.* [1997] studied the structure of the Puget Lowland during several seismic reflection studies.

Schultz and Crosson [1996] analyzed earthquake arrival times along a profile that extends from near Hood Canal on the west side of the Puget lowland to Walla Walla in eastern Washington. The focus of their investigation was the deep structure beneath the Cascade Range, but the west end of the profile crosses the Puget lowland. The main result of their research is the discovery of a seismic "root" beneath the Cascade range, which is postulated to arise from subduction driven magmatic under-plating. At the west end of this profile, the Moho was interpreted to dip at 4.4° to the east; numerical experiments with a 1-D inversion suggest that this Moho dip could cause the apparent low velocity zone at the base of the crust in the 1-D velocity inversions [e.g. *Crosson*, 1976b].

Two major seismic refraction-wide-angle reflection profiles, in 1991 and 1995, have been conducted near the edges of our target region. In 1991 the USGS and several university collaborators conducted a major N-S refraction line along the west margin of the Cascade Range. Interpretation of data from the 1991 experiment has been presented in papers by *Miller et al.* [1998]; *Gridley* [1993]. The explosion locations

along the profile are shown in figure 1.1, and these were recorded at a large number of PNSN stations as well as on temporary recorders deployed for the experiment. The 1991 experiment provided data to constrain the shallow crustal structure on the east side of our target quite well, although the deep crustal structure may not be as well imaged along the entire profile. In 1995, the USGS and university collaborators conducted an E-W profile about the latitude of Grays Harbor, Washington [Luetgert *et al.*, 1995; Parsons *et al.*, 1996]. The shot locations for the 1995 profile are also shown on figure 1.1, and several of the shots were also widely recorded on the PNSN stations.

In March of 1998 the Puget Sound region was the target of the large-scale active-source Seismic Hazard in the Puget Sound (SHIPS) project. The source was a large (6500 in^3) airgun array towed off of the University of Washington Research Vessel, Thomas Thompson. The SHIPS project was a cooperative effort between the United States Geological Survey (USGS), the University of Washington (UW), the University of Oregon (UO), and the Geological Survey of Canada (GSC). Seismic energy, provided by the UW Research Vessel Thomas Thompson, was recorded at a temporary array of ~ 250 seismographs and also at the permanent stations of the PNSN. Although the data from the temporary deployment is not yet available, the data from the permanent stations is analyzed in the final chapters of this dissertation to bolster the resolution of our tomographic model near the surface of the earth.

1.5 Why This Study is Needed

I have undertaken this study to overcome problems with the previous work. Lees and Crosson [1989] was an excellent first cut at the seismic tomography problem in the GPSR, but the one-step linear inversion cannot adequately model the expected high seismic velocity contrasts between the varied geologic units. There are two major factors that contribute to our ability to generate a higher resolution and more accurate

model for the seismic velocity in the GPSR since the study of *Lees and Crosson* [1989]. First, advances in computing power and algorithms have made it possible to use new techniques, such as the 3-D finite-difference travel-time tomography developed in this thesis. Second, there is now a much larger database containing both high quality earthquakes and explosions, including data collected during the recent SHIPS experiment (discussed in Chapters 6 and 7). While *Moran* [1995] did perform a non-linear inversion his focus was on the Mount Rainier area and the resolution is limited in the GPSR, precisely the region of greatest interest from a seismic hazard perspective.

The various refraction and reflection studies provide high resolution models but they are all 2-D studies. The geology changes rapidly in all directions in the GPSR and a 3-D model is required to gain a regional perspective. This is a particular problem in the Puget Lowland. There have been a large number of studies [e.g. *Johnson*, 1984, 1985] that attempt to interpret large scale features based on small scale studies. This has made it difficult to form a coherent model for either the kinematics or the dynamics of the terrane interaction in the region.

Our study provides a high resolution 3-D model of the seismic velocity in the GPSR. This model can be used for more accurate earthquake location and for evaluation of the regional geology and seismic hazards. It is also hoped that the high-resolution of this study will allow us better formulate kinematic and dynamic models for the enigmatic Puget Lowland.

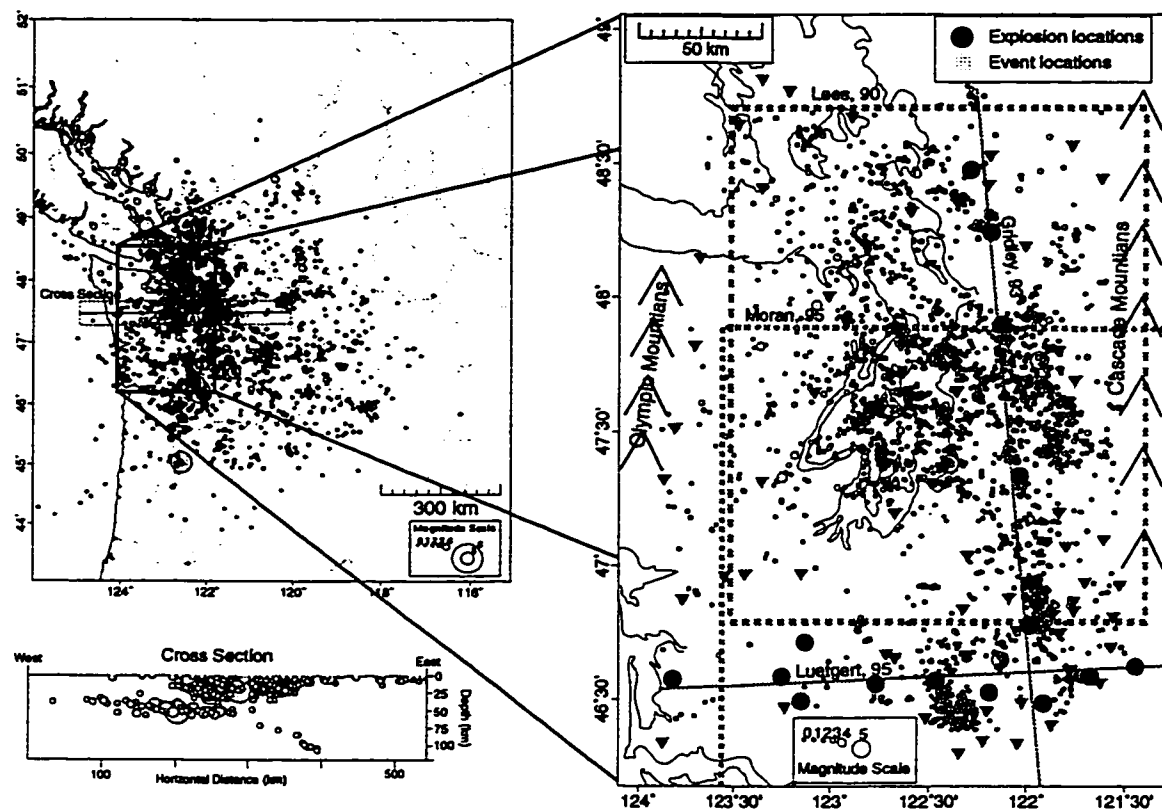


Figure 1.1: (Left) Map of regional seismicity and cross section showing two distinct seismically active regions in the Puget Sound. *The earthquakes in this map are from the PNSN catalog only, this is not meant to imply that seismicity ends at the Oregon or Canadian borders.* (Right) Map, showing the region of this study. Triangles are the locations of PNSN seismograph stations. Light circles are well located earthquakes from the PNSN catalog, scaled by magnitude, and the dark circles are explosions with known locations. Also shown are the locations of several refraction profiles and other tomography projects. Maps and cross section created with Xmap8 [Lees, 1995].

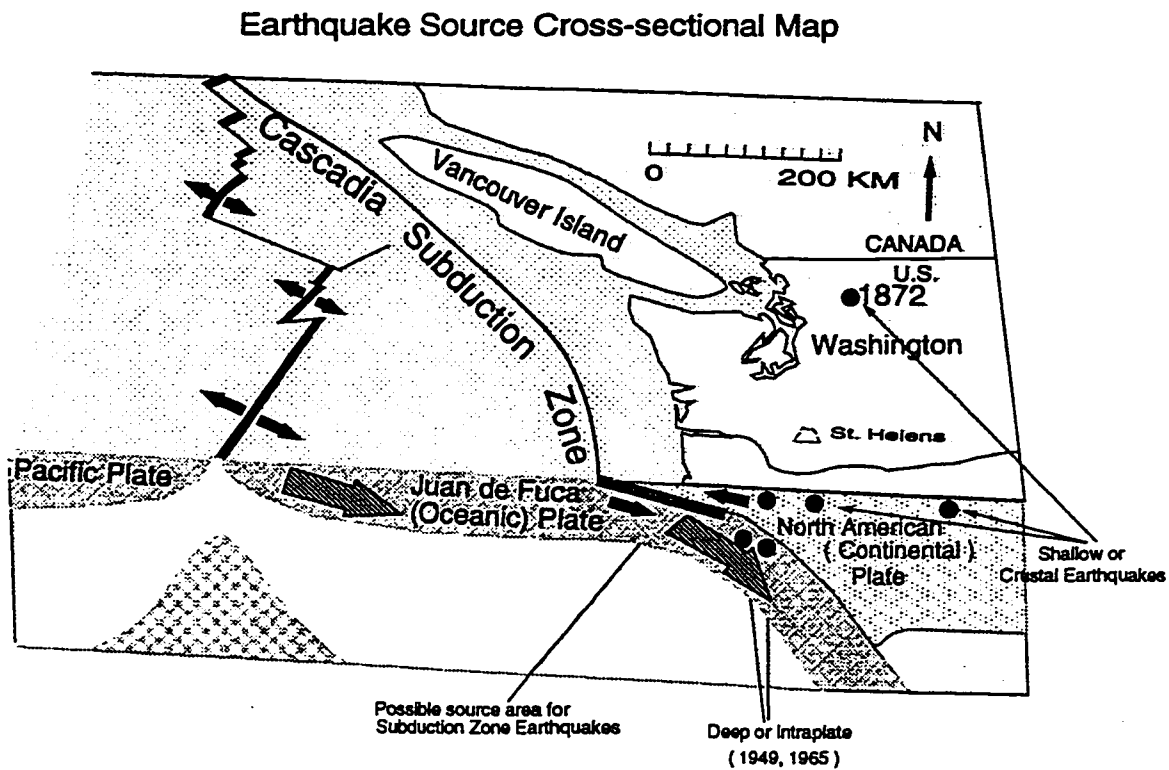


Figure 1.2: Schematic cross section through the Juan de Fuca subduction zone. The cross section shows the 3 general types of earthquakes that pose a hazard to the Pacific Northwest; subduction zone, subducted slab, and crustal.

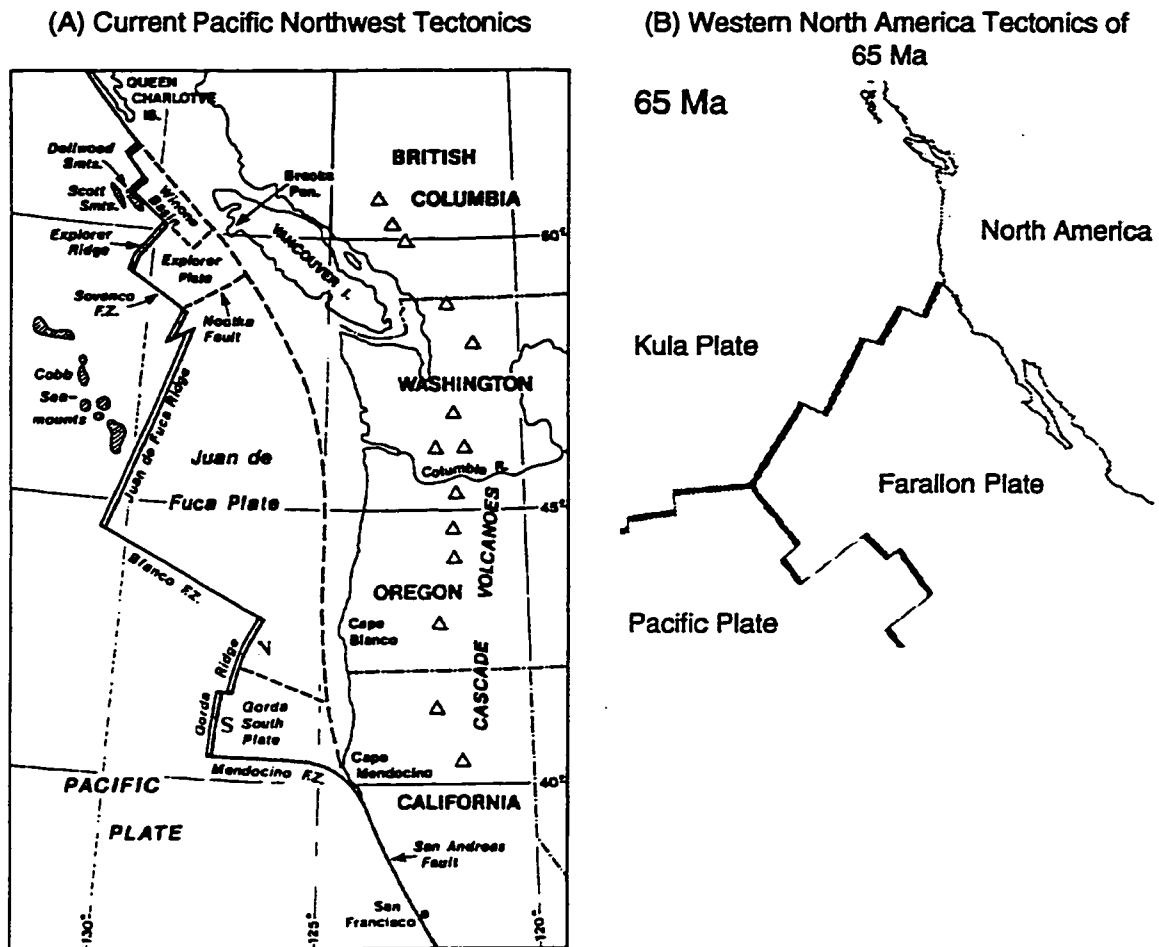


Figure 1.3: (A) Map, adapted from *Riddihough* [1984], showing the general tectonics of Western North America. (B) Map, adapted from *Babcock et al.* [1992] showing the geometry of the North American subduction zone 65 Ma.

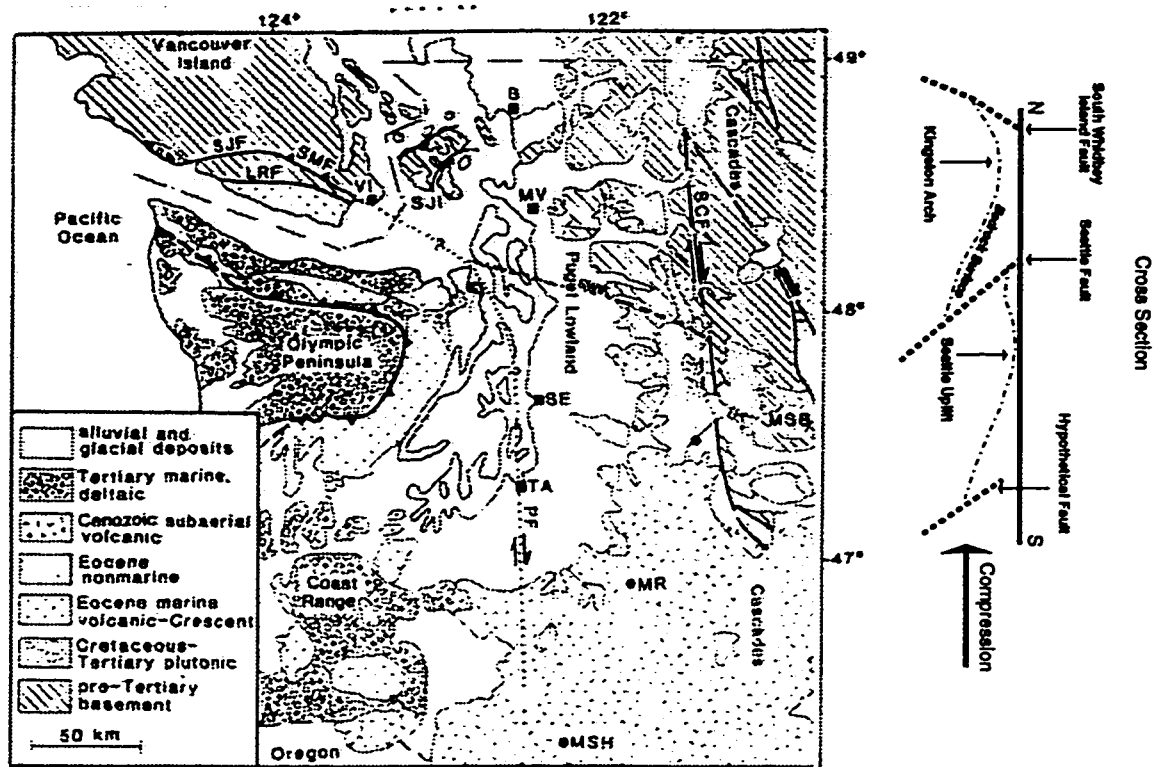


Figure 1.4: (Left) Map, modified from *Johnson* [1985] showing the major geologic provinces in the region. The three major provinces are: the Coast Range this is shown on the map as the Coast Range and the Olympic Peninsula; the Puget Lowland; and the Cascades. The map also shows some known or hypothesized faults. Abbreviations used on map: B, Bellingham; LRF, Leech River Fault; MR, Mount Rainier; MSH, Mount Saint Helens; MSB, Mount Stewart Batholith; MV, Mount Vernon; PF, Puget Fault; SCF, Straight Creek Fault; SE, Seattle; SJF, San Juan Fault; SJI, San Juan Islands; SMF, Survey Mountain Fault; SWIF, Southern Whidbey Island Fault; TA, Tacoma; VI, Vancouver Island. (Right) Cartoon cross section through the Puget Lowland, showing faults and other structures, bedrock topography, and the major direction of compression.

Chapter 2

METHOD OF ANALYSIS

2.1 Introduction

The major result in this dissertation is a 3-D image of the P-wave velocity in the Puget Lowland to a depth of approximately 60 *km*. This image has been created using seismic tomography. Seismic tomography is one of the broad class of geophysical inverse problems. In Greek *Tomo* means slice and *graph* means picture. The word tomography is usually reserved for problems which generate an image, either in 2 or 3 dimensions, by analyzing observations that can be interpreted as path integrals through the model. This is in contrast to, for example, than an inverse problem which might try to determine the density profile of the earth through analysis of the mass and moment of inertia.

This chapter begins with a review of some basic seismological concepts, such as a ray-path, which are necessary to discuss the tomography problem. Then there are two examples which serve as building blocks for the main part of the chapter which describes, in detail, the general mathematics of the seismic tomography problem and the specific method used to solve the problem in this study.

2.2 Seismology Background

When the earth ruptures along a fault the elastic wave energy propagates outward from the source, in wavefronts (surfaces along which the wave motion has the same phase). The ray-path between the source (called the earthquake hypocenter) and any other point in the earth can be thought of as the path along which the “signal”

between the two points travels. In isotropic media ray-paths and wavefronts are always perpendicular for a particular type of body wave motion (figure 2.1 A). The travel-time is the amount of time it takes for the signal to move between a specific source and receiver, and the arrival time at the receiver is the earthquake origin time plus the travel-time. Then the seismic velocity is the speed at which the signal propagates, in general a function of position. In seismological problems it is often more convenient to formulate problems in terms of the slowness, defined as the inverse of velocity (*i.e.* time per distance). Fermat's principle states that a ray-path will be a stationary point of the travel-time with respect to changes in path. As a simple example we can use Fermat's principle to derive Snell's law which describes the angle of refraction for a ray traveling through an interface between two materials with different velocities. Given the geometry in figure 2.1 B, the travel time from point A to point B is the sum of the path lengths in the two media divided by the velocity in the respective media

$$T = \frac{\sqrt{(x_i - x_A)^2 + (y_i - y_A)^2}}{v_1} + \frac{\sqrt{(x_B - x_i)^2 + (y_B - y_i)^2}}{v_2} \quad (2.1)$$

(see figure 2.1 B for a description of the variables). Since the layers have constant velocity the only way the path can change is through the intersection point x_i . Taking the derivative

$$\frac{dT}{dx_i} = \frac{x_i - x_A}{v_1 \sqrt{(x_i - x_A)^2 + (y_i - y_A)^2}} - \frac{x_B - x_i}{v_2 \sqrt{(x_B - x_i)^2 + (y_B - y_i)^2}} \quad (2.2)$$

Now we can make the substitutions

$$\begin{aligned} \sin(\Theta_1) &= \frac{x_A - x_i}{\sqrt{(x_A - x_i)^2 + (y_A - y_i)^2}} \\ \sin(\Theta_2) &= \frac{x_B - x_i}{\sqrt{(x_B - x_i)^2 + (y_B - y_i)^2}} \end{aligned} \quad (2.3)$$

and set equation 2.2 equal to zero to find the stationary points. With minor simplifications the result is

$$\frac{\sin(\Theta_1)}{v_1} = \frac{\sin(\Theta_2)}{v_2} \quad (2.4)$$

Snell's law.

A major approximation that we make in this study is that the earthquake can be considered a point source in both space and time. Define this 4 dimensional location as the earthquake hypocenter. In reality the earthquake takes place on a fault which occupies a finite amount of space. Furthermore, the fault ruptures over a finite amount of time. A larger earthquake typically has a larger fault area, and thus it will occupy more space, and will usually have a longer duration. However, the largest crustal earthquakes used in this study have magnitude of about 5 with a typical fault area of 15 km^2 and a duration of 5 sec [e.g. Dewberry and Crosson, 1996]. Since we will only be using the first arrival signals (defined momentarily) the duration of the earthquake is not important. First arrival signals are assumed to originate near the point of initiation of rupture of an earthquake. Since the stations we are using for analysis are usually at distances of more than 10 km and the earthquake does not rupture across the entire fault simultaneously the point source approximation is a good one.

For any given source receiver geometry, signals can propagate along many different paths (e.g. reflections or refractions) and can travel in different modes (e.g. P or S-body waves, surface waves). Both P and S body waves propagate through the interior of the earth, with P waves traveling faster than S waves. First arriving P waves are normally observed most accurately, since they arrive before any other complicating body and surface wave signals. Therefore only P wave observations are used in this study.

After an earthquake is recorded an analyst picks the arrival-times off the seismogram and these become the observations for the tomography problem. It is often possible for the analyst to pick several different arrivals from a given earthquake, however, the first arrival is almost always the least ambiguous since later arrivals must be picked from within the envelope of energy arriving at the receiver. After picking, the data are reduced from a recording of the ground motion at the receiving

seismograph to two numbers, the arrival-time and an associated error estimate.

The result of the tomography process is a 3-D image showing the estimated velocity at which a signal would travel through the earth. This is the seismic velocity structure of the region containing the sources. Since the data are observations of the P-wave arrival-time the model is for the P-wave velocity.

2.3 Travel-time Calculation

Solution of any inverse problem requires that we are able to calculate observations from a given model. In the seismic tomography problem this corresponds to the calculation of arrival-times given an estimate of the seismic velocity in the region and the location of the sources (earthquakes) and receivers (seismographs). This is known as the forward problem for the tomography process. Solution of any inverse problem first requires that we have a method of performing the forward problem. There are three common method of calculating seismic arrival-times in a 3-D model; shooting, bending, and finite-difference methods.

First, the shooting method gets its name from the similarity to a ballistics problem. The travel-time calculator picks a dip and azimuth and traces a ray through the model (bending the path to obey Snell's law at all interfaces). The travel-time calculator then attempts to adjust the dip and azimuth until the ray connects the source and receiver (figure 2.3). This method can be used for 2-D problems where the computation is much simpler since there is only one parameter, the takeoff angle (dip), to adjust. Shooting has the benefit of being easy to understand and simple to implement. It has two major flaws, first, there may be more than one ray connecting the source receiver pair, and only one is the first arrival. In a complicated geometry it may be difficult to find the one unique ray which represents the first arrival. This problem is illustrated in figure 2.2, even for this relatively simple geometry the distance range from 75 – 175 *km* has multiple arrivals. Figure 2.2 also illustrates the

second major problem with the shooting method, the distance range from 50 – 75 *km* at 10 *km* has almost no arrivals. This figure was produced by shooting rays at increments of $\frac{1}{1000}^\circ$. In this distance range this increment in takeoff angle produces a change in the distance traveled by a ray of 5 *km*. Energy from an earthquake does reach this distance range but because of the approximations used to reach the ray formulation this portion of the signal is lost.

The second method, ray bending has commonly been used for most tomography problems. This method starts with a path connecting the source receiver pair which is not a ray (it is not stationary and it does not obey Snell's law at interfaces). The algorithm then attempts to adjust this path into a physical ray. During the adjustment, or bending, process some form of approximation is usually employed. These methods are usually quite fast, but like the shooting method there is no guarantee that the path found is the true first arrival path. The approximations inherent to this method can also result in substantial errors in the calculated times in a complex geometry. The method of *Um and Thurber* [1987] is a ray bending method that has commonly been used in regional tomography problems.

The final method is the one used in this project. A finite-difference scheme [*Vidale*, 1990; *Hole and Zelt*, 1995] is used to calculate the travel-time to every point in a grid from a given source location. These methods solve the eikonal equation on an expanding subset of nodes in a box around the source location (see Appendix A for details of the method). Finite difference methods have the advantages of being fast (when large numbers of travel-times must be calculated) and accurate. Since the travel-time is calculated to all points in the grid we can always find a travel-time between any two points. With finite-difference methods the solution is always guaranteed to be a global rather than a local extremal path. This is an improvement over either the bending or the shooting method.

We can divide inverse problems into two broad classes, linear and non-linear. A linear problem must pass a single test with regards to the changes in the observations

when the model changes. First define the functional F as a process which acts on a given model \mathbf{m} to produce an estimated observation. In the case of the seismic tomography problem the functional is the travel-time calculator. Then a linear problem must satisfy

$$F[\alpha\mathbf{m}_1 + \beta\mathbf{m}_2] = \alpha F[\mathbf{m}_1] + \beta F[\mathbf{m}_2] \quad (2.5)$$

where α and β are non-zero scalars [*Parker*, 1994, p. 11]. Given this definition seismic tomography, and earthquake location, are non-linear problems.

If we define the forward problem as the prediction of the observations for a given model then the inverse problem is just the opposite. Given the data, observations of arrival times at a set of seismograph stations, can we determine the model (the locations of the earthquakes and the velocity of the earth in the region containing the earthquakes and the seismographs)? A general framework for solution to a geophysical inverse problem was laid out in *Backus and Gilbert* [1968] but the basic idea was known well before that, for instance Geiger's Method of earthquake location has been used since the early 1900's. It is useful to start with two examples that can be thought of as building blocks for the full problem and also serve to introduce some terminology.

2.4 Elementary Examples

2.4.1 Geiger's Method of Earthquake Location

The earthquake location problem is a geophysical inverse problem in which we consider the hypocenter of the earthquake to be the only unknown. The location of the seismographs is of course known to the people who do the installation but the derivation of a velocity model for the earth is a complex problem which we will assume has already been solved. Since this example relates to the seismic tomography problem which solves for the P-wave velocity only, we will simplify the problem further by considering only P-waves (there is only a single velocity model instead of one for each

type of wave).

This is a non-linear problem, and for any reasonable velocity structure the dependence of the travel-time on the model (the hypocenter location) is a complex one. Figure 2.2 shows an example of the travel-time as a function of distance from source to receiver for several event depths using an approximation to the current 1-D velocity model used by the PNSN in the Puget Sound region (table 1.1). Although there are alternative methods of solution, here we present a standard perturbation formulation of the solution known as “Geiger’s Method”. The observations are a vector of arrival times τ_i picked by an analyst; assume there are p picks. We start with a guess for an initial hypocenter

$$\mathbf{m}^{(0)} = \begin{bmatrix} m_1 \\ m_2 \\ m_3 \\ m_4 \end{bmatrix} \quad (2.6)$$

where

$$\begin{aligned} m_1 &= x \\ m_2 &= y \\ m_3 &= z \\ m_4 &= t \end{aligned} \quad (2.7)$$

are the hypocenter parameters; x , y , and z are the Cartesian coordinates and t is the earthquake origin time.

Then the estimated travel-time from the hypocenter to the i th station is given by a functional (the travel-time calculator) acting on the starting model

$$\hat{\tau}_i = T_i[\mathbf{m}^{(0)}]; \quad i = 1, \dots, p \quad (2.8)$$

Here, of course, the functional also includes information relating to the velocity model and station location. Now, the residual for the i th station is defined as the observed

arrival time minus the calculated arrival time

$$r_i = \tau_i - \hat{\tau}_i; \quad i = 1, \dots, p \quad (2.9)$$

Clearly if the r_i are small, then the predicted arrival-times closely match the observed arrival-times and we consider that the solution is good. Conversely, if the r_i are large, then the predicted arrival-times are a poor match to the observed arrival-times and the solution is likely to be far from the “true” earthquake location. However, caution should be taken in interpreting residuals. For example, if there are only four independent observations, then in general a solution can always be found which reduces all residuals to zero. This does not mean that the solution in this case is exact. Similarly, in the case of a large number of observations the residual vector can never be reduced to zero length due to velocity model errors and observational uncertainty.

Finding the earthquake location involves finding the model that reduces some measure of the residual vector (a vector of the r_i across the p stations recording the event). The “standard” method of earthquake location minimizes the L_2 norm of the residual vector

$$L_2 = \sum_{i=1}^p r_i^2 \quad (2.10)$$

Since this is the best analogy to the method used later in the seismic tomography problem it is the convention that I will follow here.

Considering the arrival-time problem in isolation, it is possible to expand the arrival-time evaluated at an arbitrary model \mathbf{m} about $\mathbf{m}^{(0)}$

$$T_i[\mathbf{m}] = T_i[\mathbf{m}^{(0)}] + \sum_{k=1}^4 \left. \frac{\partial T_i}{\partial m_k} \right|_{\mathbf{m}^{(0)}} \delta m_k + \text{higher order terms} \quad (2.11)$$

where

$$\delta \mathbf{m} = \mathbf{m} - \mathbf{m}^{(0)} \quad (2.12)$$

Assuming that a travel-time calculation algorithm is a good approximation to the actual travel-time function the partial derivatives may be found analytically during the calculation of the travel-times or if all else fails they can be approximated

empirically by perturbing the model parameters. The choice depends on the exact implementation of the model and the algorithm used to calculate the arrival time.

Now associate the observations with the “true” arrival-times, and the arrival-time calculator for the initial model with the “estimated” arrival time. Equations 2.9 and 2.11 may be combined to give

$$r_i = \sum_{k=1}^4 \left. \frac{\partial T_i}{\partial m_k} \right|_{\mathbf{m}^{(0)}} \delta m_k; \quad i = 1..p \quad (2.13)$$

In this equation we have neglected higher order terms involving squares and higher powers of $\delta \mathbf{m}$. This neglect is valid if $\mathbf{m}^{(0)}$ is close to the true model. Equation 2.13 represents a set of p equations in 4 unknowns representing the perturbation from the present model ($\mathbf{m}^{(0)}$) to the true model (\mathbf{m}). Since this system of equations represent only a linear approximation to a non-linear problem, we cannot expect to solve for the true earthquake hypocenter directly.

We can restate the system of p equations in a single matrix equation by defining

$$\mathbf{J} = \begin{bmatrix} \left. \frac{\partial T_1}{\partial m_1} \right|_{\mathbf{m}^{(0)}} & \left. \frac{\partial T_1}{\partial m_2} \right|_{\mathbf{m}^{(0)}} & \left. \frac{\partial T_1}{\partial m_3} \right|_{\mathbf{m}^{(0)}} & \left. \frac{\partial T_1}{\partial m_4} \right|_{\mathbf{m}^{(0)}} \\ \left. \frac{\partial T_2}{\partial m_1} \right|_{\mathbf{m}^{(0)}} & \left. \frac{\partial T_2}{\partial m_2} \right|_{\mathbf{m}^{(0)}} & \left. \frac{\partial T_2}{\partial m_3} \right|_{\mathbf{m}^{(0)}} & \left. \frac{\partial T_2}{\partial m_4} \right|_{\mathbf{m}^{(0)}} \\ \vdots & \vdots & \vdots & \vdots \\ \left. \frac{\partial T_p}{\partial m_1} \right|_{\mathbf{m}^{(0)}} & \left. \frac{\partial T_p}{\partial m_2} \right|_{\mathbf{m}^{(0)}} & \left. \frac{\partial T_p}{\partial m_3} \right|_{\mathbf{m}^{(0)}} & \left. \frac{\partial T_p}{\partial m_4} \right|_{\mathbf{m}^{(0)}} \end{bmatrix} \quad (2.14)$$

Then if we could solve the equation

$$\mathbf{J} \delta \mathbf{m} = \mathbf{r} \quad (2.15)$$

the model $\mathbf{m}^{(0)} + \delta \mathbf{m}$ would (to the limits of the linearization) result in a residual vector with a magnitude of zero. In all practical cases there are more stations than the four model parameters so equation 2.15 does not, in general, have a solution. However, if we solve the corresponding normal equations

$$\mathbf{J}^t \mathbf{J} \delta \mathbf{m} = \mathbf{J}^t \mathbf{r} \quad (2.16)$$

we end up with the model which produces the minimum L_2 norm of the residual vector [*Press et al.*, 1986, p. 511].

Since equation 2.11 is based on a linearization of the full travel-time equation one iteration of equation 2.16 will not, in general, provide a good solution to this problem. However, if we perform a loop, repeatedly solving equation 2.16 and then recalculating the travel-times we should approach the best solution for the earthquake hypocenter location. In practice, although we have more equations than unknowns in the matrix (equation 2.14) there are often very low eigenvalues in the normal matrix $\mathbf{J}^t\mathbf{J}$. This is commonly manifested as a “tradeoff” between the origin time and the earthquake depth. To reduce the effects of small eigenvalues some form of Levenburg-Marquardt damping is usually used during on each iteration.

2.4.2 *The Linear Seismic Tomography Problem*

This example will show a very simplified 2-D seismic tomography problem. In order to simplify the problem we will make 2 major assumptions (neither one of which is very good in the real world). (1) Assume there are sources and receivers with known locations distributed around the edge of the space we are interested in. (2) Assume all the ray paths are straight lines that do not obey Snell’s law. Taken together these two assumptions, known sources and straight ray-paths, make this a linear problem.

The model is broken up into a set of cells and each is assigned a variable describing the inverse of it’s velocity known as the slowness. The contribution of each cell to the travel-time of a specific ray is just the ray length in that cell multiplied by the slowness. Since we have control over the source and the receiver locations we can select rays to form a complete system of equations and then solve for the characteristics of each cell based on the ray lengths and the values of all the rays. For the four node four ray system shown in figure 2.4, define the travel-time of the i th ray as t_i , the slowness of the j th cell as s_j and the path length of the i th ray in the j th cell as P_{ij} .

Then the geometry in figure 2.4 leads to 4 equations in 4 unknowns

$$\begin{aligned}
 t_1 &= P_{11}s_1 + P_{12}s_2 \\
 t_2 &= P_{23}s_3 + P_{24}s_4 \\
 t_3 &= P_{32}s_2 + P_{34}s_4 \\
 t_4 &= P_{42}s_2 + P_{43}s_3 + P_{44}s_4
 \end{aligned} \tag{2.17}$$

This can also be expressed in a matrix form as

$$\mathbf{As} = \mathbf{t} \tag{2.18}$$

if we define the quantities

$$\begin{aligned}
 \mathbf{t} &= \begin{bmatrix} t_1 \\ t_2 \\ t_3 \\ t_4 \end{bmatrix} \\
 \mathbf{s} &= \begin{bmatrix} s_1 \\ s_2 \\ s_3 \\ s_4 \end{bmatrix} \\
 \mathbf{A} &= \begin{bmatrix} P_{11} & P_{12} & P_{13} & P_{14} \\ P_{21} & P_{22} & P_{23} & P_{24} \\ P_{31} & P_{32} & P_{33} & P_{34} \\ P_{41} & P_{42} & P_{43} & P_{44} \end{bmatrix}
 \end{aligned} \tag{2.19}$$

where, in this case, almost half of the P_{ij} are exactly zero.

The assumptions made at the beginning of this example make this a linear and fully constrained problem. Therefore, solution of equation 2.18 provides a model which exactly fits the data in one step, there is no need for iteration.

2.5 Non-Linear 3-D Seismic Tomography

The full non-linear seismic tomography problem is considerably more difficult for three reasons. (1) The medium properties vary strongly so that seismic source travel-times are predicted by rays that may be strongly curved in the earth. (2) In regional seismic tomography the receivers are only on one side of the model (at or very close to the surface of the earth). (3) The source and receiver geometry is very sparse and irregular. In fact many (or all) of the source locations (hypocenters) are unknown and must be determined as part of the model.

2.5.1 The Forward Problem

Assume we have q sources (earthquakes) each recorded at p receivers (seismographs). For simplicity of notation assume all sources are recorded at all receivers. From each recording we extract the P-wave travel time. We define the observed arrival time from the i th earthquake to the j th seismograph as τ_{ij} . The notation τ_{ij} is somewhat confusing; this actually represents a vector of length i by j not a matrix. We also define

$$\mathbf{x}_i = \begin{bmatrix} x_i \\ y_i \\ z_i \\ \tau_i \end{bmatrix} \quad (2.20)$$

as the set of four dimensional earthquake location (the hypocenter) of the i th earthquake. Then the arrival time of a seismic signal can be written as

$$\tau_{ij} = \tau_i + \int_{l[v(\underline{\xi}), \mathbf{x}_i]} \frac{1}{v(\underline{\xi})} dl(\underline{\xi}) \quad (2.21)$$

where $v(\underline{\xi})$ is the true earth seismic velocity as a function of position and l is the minimum travel-time path of the signal from the earthquake hypocenter to the seismograph station (the ray-path). The ray-path depends on both the velocity structure of the earth and the location of the hypocenter.

It is convenient to define our model in terms of the inverse of velocity, $s = \frac{1}{v}$, termed the slowness. The slowness as a function of position, $s(\underline{\xi})$, is approximated; since we cannot define the slowness at every location in the earth we choose to define it a set of n known points on a regular grid,

$$\mathbf{s} = \begin{bmatrix} s_1 \\ s_2 \\ \vdots \\ s_n \end{bmatrix} \quad (2.22)$$

The slowness at any point within the model is then given by tri-linear interpolation using the 8 nodes surrounding any point that lies within the model. If we define $c_k(\underline{\xi})$ as the interpolation coefficient for the k th node for a point $\underline{\xi}$ (for any given $\underline{\xi}$ only 8 of the c_k will be non-zero). Then we can write

$$s(\underline{\xi}) = \sum_{k=1}^n s_k c_k(\underline{\xi}) \quad (2.23)$$

this is the relationship between the discretized slowness model and an estimate for the true slowness at the point $\underline{\xi}$.

This is one of three common methods to approximate a complex earth with a finite number of variables, the other two are: (1) expansion in orthogonal functions. This method is often used by the global seismological community for the definition of 3-D whole earth velocity models where the expansion functions are spherical harmonics. (2) The representation by 3-D constant velocity blocks or voxels. The voxel and the node methods are similar but there are important differences. The voxel method can represent a true discontinuity in the slowness field but can only approximate a continuous field; the node method with linear interpolation can represent a continuous field but can only approximate a discontinuity through a high gradient across a small distance (figure 2.5).

We now define the full model as the combination of the slowness model and the

unknown hypocenters

$$\mathbf{m} = \begin{bmatrix} \mathbf{s} \\ \mathbf{x}_1 \\ \mathbf{x}_2 \\ \vdots \\ \mathbf{x}_q \end{bmatrix} \quad (2.24)$$

Notice that this is single vector of length $n + 4q$. The arrival-time for the i th event at the j th station can be approximated as a function of \mathbf{m} which is accurate to the degree that our discrete model representation (\mathbf{s}) and the hypocenter assumptions match the real earth.

$$\widehat{\tau}_{ij} = T_{ij}[\mathbf{m}]; \quad i = 1, \dots, p; \quad j = 1, \dots, q \quad (2.25)$$

\mathbf{m} is the full model including both the discrete approximation to the slowness of the earth and the hypocenter coordinates; and $T_{ij}[\mathbf{m}]$ is a functional which calculates the seismic travel-time based on the model (and also incorporating known portions of the model such as the receiver locations); and $\widehat{\tau}_{ij}$ is an estimate for the arrival time from the i th earthquake to the j th seismograph based on the current model.

2.5.2 Inverse Problem

The inverse problem is defined as the construction of a model that fits a set of observational data in a prescribed manner. There are many ways in which an inverse model can be constructed including selection from a randomly generated set of models (so-called "Monte Carlo" methods) and systematic generation using linear analysis methods. The earth may be thought of as comprising a highly complex system requiring a large number of "parameters" to describe. In fact the real earth is complex on so many different length scales that the description of any significant volume of the earth would effectively require an enumerable number of parameters. On the other hand our observational capability is quite limited and based on a relatively small

number of observations. Therefore we can not expect to determine (or “invert” for) every detail of the earth structure. We see some necessarily simplified version of the true earth that adequately explains our observations.

In seeking our inverse model we may impose various constraints; for example, we may require that the P-wave velocity (or slowness) at a point in the model approximate an appropriate weighted average of the true earth over some volume taken about the observation point. This type of constraint is an example of a “smoothing constraint”.

In the travel-time problem as noted earlier, the observed travel-times are not a linear function of slowness structure or hypocenter parameters. As a result, we cannot formulate a linear approximation to the inverse problem that will allow us to compute the inverse model in one step. Therefore, a perturbation formulation is required which allows us to compute an improved model (in the sense of fitting the data better) from an existing approximation.

The “model” in our problem comprises a finite number of numerical parameters describing the P-wave slowness and hypocenters of the events within our model space. The model space is the 3-D volume of the earth within which we will estimate the slowness and hypocenter parameters. Define an initial reference model estimate, $\mathbf{m}^{(0)}$, which is a composite vector of model and hypocenter sub-vectors

$$\mathbf{m}^{(0)} = \begin{bmatrix} \mathbf{s}^{(0)} \\ \mathbf{x}_1^{(0)} \\ \mathbf{x}_2^{(0)} \\ \vdots \\ \mathbf{x}_q^{(0)} \end{bmatrix} \quad (2.26)$$

where \mathbf{s} is the model vector and \mathbf{x}_k are the hypocenter vectors. For the tomography problem the starting model can be obtained from an existing 1-D model or may be a 3-D model derived from earlier work [e.g. *Symons and Crosson, 1995a*]. Depending on whether we are calculating travel-time (using a finite difference method) or whether

we are estimating the slowness values, we are free to use different parameterizations or coarseness of grid spacing in the slowness representation. This is an important detail in practice which can be ignored at this point in the mathematical formulation.

If we perform a Taylor expansion about the reference model $\mathbf{m}^{(0)}$, then equation 2.25 becomes

$$T_{ij}[\mathbf{m}] = T_{ij}[\mathbf{m}^{(0)}] + \sum_{k=1}^{n+4q} \left. \frac{\partial T_{ij}}{\partial m_k} \right|_{\mathbf{m}^{(0)}} \delta m_k + \text{higher order terms} \quad (2.27)$$

where δm_k is the change in the k th model parameter, $\left. \frac{\partial T_{ij}}{\partial m_k} \right|_{\mathbf{m}^{(0)}}$ is a derivative relating changes in the k th model parameter to changes in the calculated arrival-time of the i th event at the j th station.

Now, we can define the residual as the observed minus the calculated arrival time

$$r_{ij} = \tau_{ij} - \widehat{\tau}_{ij}^{(0)} \quad (2.28)$$

and, substituting equation 2.27 into equation 2.28 for τ_{ij} , to first order

$$r_{ij} = \sum_{k=1}^{n+4q} \left. \frac{\partial T_{ij}}{\partial m_k} \right|_{\mathbf{m}^{(0)}} \delta m_k \quad (2.29)$$

If we define the residual vector

$$\mathbf{r} = \begin{bmatrix} r_{1,1} \\ r_{1,2} \\ \vdots \\ r_{1,p} \\ r_{2,1} \\ \vdots \\ r_{q,p} \end{bmatrix} \quad (2.30)$$

and the Jacobian matrix

$$\mathbf{J} = \begin{bmatrix} \left. \frac{\partial T_{11}}{\partial m_1} \right|_{\mathbf{m}^{(0)}} & \left. \frac{\partial T_{11}}{\partial m_2} \right|_{\mathbf{m}^{(0)}} & \dots & \left. \frac{\partial T_{11}}{\partial m_{n+4q}} \right|_{\mathbf{m}^{(0)}} \\ \left. \frac{\partial T_{12}}{\partial m_1} \right|_{\mathbf{m}^{(0)}} & \left. \frac{\partial T_{12}}{\partial m_2} \right|_{\mathbf{m}^{(0)}} & \dots & \left. \frac{\partial T_{12}}{\partial m_{n+4q}} \right|_{\mathbf{m}^{(0)}} \\ \vdots & \vdots & & \vdots \\ \left. \frac{\partial T_{1p}}{\partial m_1} \right|_{\mathbf{m}^{(0)}} & \left. \frac{\partial T_{1p}}{\partial m_2} \right|_{\mathbf{m}^{(0)}} & \dots & \left. \frac{\partial T_{1p}}{\partial m_{n+4q}} \right|_{\mathbf{m}^{(0)}} \\ \left. \frac{\partial T_{21}}{\partial m_1} \right|_{\mathbf{m}^{(0)}} & \left. \frac{\partial T_{21}}{\partial m_2} \right|_{\mathbf{m}^{(0)}} & \dots & \left. \frac{\partial T_{21}}{\partial m_{n+4q}} \right|_{\mathbf{m}^{(0)}} \\ \vdots & \vdots & & \vdots \\ \left. \frac{\partial T_{qp}}{\partial m_1} \right|_{\mathbf{m}^{(0)}} & \left. \frac{\partial T_{qp}}{\partial m_2} \right|_{\mathbf{m}^{(0)}} & \dots & \left. \frac{\partial T_{qp}}{\partial m_{n+4q}} \right|_{\mathbf{m}^{(0)}} \end{bmatrix} \quad (2.31)$$

Then, to the limitations of the linearization approximation, if there is a solution to the equation

$$\mathbf{J}\delta\mathbf{m} = \mathbf{r} \quad (2.32)$$

$\mathbf{m}^{(0)} + \delta\mathbf{m}$ will precisely fit the data.

As with the Geiger's method example, since equation 2.32 is only a linearization of the full problem, finding a model requires a number of iterations. On each iteration we calculate travel-times and residuals using the non-linear calculator then solve equation 2.32 and update the model. As the model gets closer to the "true earth" the linearization approximation gets better and the calculated perturbations get smaller.

Computation of the Frechêt Kernels

The partial derivatives are also known as Frechêt kernels; $\frac{\partial T_{ij}}{\partial m_k}$ is the derivative of the arrival time of the i th earthquake at the j th station with respect to the k th model parameter. An obvious, but very inefficient, method of approximating the kernels is by a forward difference operator in which individual model parameters are changed and travel-times are recalculated. This method has been used for small 2-D problems [Ammon and Vidale, 1993], but it rapidly becomes intractable for larger 2-D or for any 3-D problems since the number of parameters grows rapidly for larger problems,

we would have to perturb $\sim 100,000$ individual parameters, and recalculate $\sim 50,000$ travel-times for each perturbation.

The solution adopted here is to use a semi-analytical approach based on ray theory. Finding the ray-path is normally a difficult problem in it's own right. It is done by either the shooting or the bending method of finding a seismic travel-time. In this case, however, the finite difference travel-time calculator (FDTT) has already done most of the work; the travel-time has been calculated to all of the model space, and surfaces with equal travel-time are analogous to wavefronts. Since the ray-path is always perpendicular to the wavefronts, if we start from the receiver the quickest way to the source is just the negative gradient of the travel-time field (figure 2.6). Since the travel-times are calculated on a finite difference grid we can use a numerical first difference operator to find the gradient at any point. We can then take a small step in the direction of the negative gradient and repeat the process, building up the ray-path as a set of straight line segments as we go (figure 2.7). Fermat's Principle states that the travel-time is stationary with respect to small changes in the ray-path. This implies that to first order, travel-time perturbations depend only on velocity model perturbations, not on ray-path perturbations. A small change in velocity will not move the ray-path and the change in travel-time is just the product of the length of the segment and the change in slowness along the segment. If the segments are short then the velocity of a segment is approximately constant and the slowness of the segment is just the slowness at the center of the segment as determined by trilinear interpolation from the 8 nodes surrounding the point. If the center of the m th segment is at the point $\underline{\xi}_m$ then we use equation 2.23 and the Frechét kernels are the products of the ray segment length and the interpolation coefficients.

$$\frac{\partial T_{ij}}{\partial m_k} = \sum_{m=1}^q l_m^{(ij)} c_k(\underline{\xi}_m) \quad (2.33)$$

where $l_m^{(ij)}$ is the path length of the m th segment of the ray between the i th earthquake and the j th station; and $c_k(\underline{\xi}_m)$ is the interpolation coefficient for of the k th model

parameter for the m th segment.

In practice I have found that $\frac{1}{10}$ of a cell side length is a good value for the length of the segments. There is an important distinction to be made here between the grid used to calculate the travel-times and the grid used to perform the inversion. The travel-time gradients are calculated using the travel-time grid but the Frechêt kernels are accumulated segment by segment on the inversion grid.

External Constraints

In the same manner we can add external constraints, based on known velocities from wells or refraction profiles. Assume we have u constraints, the i th constraint is for a slowness of V_i at location $\underline{\xi}_i$. Then if the current model is $\mathbf{m}^{(0)}$, with elements $m_k^{(0)}$, we can calculate the slowness at $\underline{\xi}_i$ with the current model

$$V_i[\mathbf{m}^{(0)}] = \sum_{k=1}^n c_k(\underline{\xi}_i) m_k^{(0)} \quad (2.34)$$

Equation 2.34 is linear and has the analytic derivative

$$\left. \frac{\partial V_i}{\partial m_k} \right|_{\mathbf{m}^{(0)}} = c_k(\underline{\xi}_i) \quad (2.35)$$

so the slowness for a model, \mathbf{m} , can be expressed exactly in a linear expansion

$$V_i[\mathbf{m}] = V_i[\mathbf{m}^{(0)}] + \sum_{k=1}^n \left. \frac{\partial V_i}{\partial m_k} \right|_{\mathbf{m}^{(0)}} \delta m_k \quad (2.36)$$

where as previously $\delta \mathbf{m} = \mathbf{m} - \mathbf{m}^{(0)}$. If we define the residual for the i th external constraint as $\delta V_i = V_i[\mathbf{m}] - V_i[\mathbf{m}^{(0)}]$ then a re-arrangement of equation 2.36 yields a linear equation to eliminate the external constraint residuals by perturbing the current model

$$\delta V_i = \sum_{k=1}^n \left. \frac{\partial V_i}{\partial m_k} \right|_{\mathbf{m}^{(0)}} \delta m_k \quad (2.37)$$

Each external constraint generates a single equation of this form.

Matrix Formulation

We can combine the ray and the external constraints into a single matrix equation. Recall that there are n slowness parameters in the model and $4q$ hypocenter parameters (equations 2.20 and 2.22).

$$\mathbf{J} = \begin{bmatrix}
 \frac{\partial \tau_{11}}{\partial m_1} \dots \frac{\partial \tau_{11}}{\partial m_n} & \frac{\partial \tau_{11}}{\partial m_{n+1}} \dots \frac{\partial \tau_{11}}{\partial m_{n+4}} & 0 & \dots & 0 \\
 \vdots & \vdots & \vdots & \vdots & \vdots \\
 \frac{\partial \tau_{1p}}{\partial m_1} \dots \frac{\partial \tau_{1p}}{\partial m_n} & \frac{\partial \tau_{1p}}{\partial m_{n+1}} \dots \frac{\partial \tau_{1p}}{\partial m_{n+4}} & 0 & \dots & 0 \\
 \frac{\partial \tau_{21}}{\partial m_1} \dots \frac{\partial \tau_{21}}{\partial m_n} & 0 \dots 0 & \frac{\partial \tau_{21}}{\partial m_{n+5}} \dots \frac{\partial \tau_{21}}{\partial m_{n+8}} & 0 \dots 0 & 0 \\
 \vdots & \vdots & \vdots & \vdots & \vdots \\
 \frac{\partial \tau_{2p}}{\partial m_1} \dots \frac{\partial \tau_{2p}}{\partial m_n} & 0 \dots 0 & \frac{\partial \tau_{2p}}{\partial m_{n+5}} \dots \frac{\partial \tau_{2p}}{\partial m_{n+8}} & 0 \dots 0 & 0 \\
 \vdots & \vdots & \vdots & \ddots & \vdots \\
 \frac{\partial \tau_{q1}}{\partial m_1} \dots \frac{\partial \tau_{q1}}{\partial m_n} & 0 & \dots & 0 & \frac{\partial \tau_{q1}}{\partial m_{n+4q+1}} \dots \frac{\partial \tau_{q1}}{\partial m_{n+4q+4}} \\
 \vdots & \vdots & \vdots & \vdots & \vdots \\
 \frac{\partial \tau_{qp}}{\partial m_1} \dots \frac{\partial \tau_{qp}}{\partial m_n} & 0 & \dots & 0 & \frac{\partial \tau_{qp}}{\partial m_{n+4q+1}} \dots \frac{\partial \tau_{qp}}{\partial m_{n+4q+4}} \\
 \frac{\partial V_1}{\partial m_1} \dots \frac{\partial V_1}{\partial m_n} & 0 & \dots & \dots & 0 \\
 \vdots & \vdots & \vdots & \vdots & \vdots \\
 \frac{\partial V_q}{\partial m_1} \dots \frac{\partial V_q}{\partial m_n} & 0 & \dots & \dots & 0
 \end{bmatrix} \quad (2.38)$$

If the matrix equation

$$\mathbf{r} = \mathbf{J} \delta \mathbf{m} \quad (2.39)$$

has a solution, then $\mathbf{m}^{(0)} + \delta \mathbf{m}$ will simultaneously satisfy all of the observations (to the limits of the linearization in equation 2.29). Of course since the linearization is only an approximation we are required to iterate to a solution.

Weighting of Equations

In the final solution the data will not be perfectly fit and it is desirable to weight the rows of equation 2.39 so some rays are preferentially fit over others. At the time

an event is picked all picks are assigned a numerical factor according to the analysts confidence in the true location of the pick. Most seismographs operated by the PNSN are digitized with a 100Hz sample frequency and so the minimum confidence interval is 0.01s . However, most arrivals cannot be picked to nearly this precision and the confidence interval will almost always be higher than this. We also wish to weight the events, events with many picks are better located than events with few picks but some of the picks may contain redundant information. To weight the individual picks we pre-multiply equation 2.39 by a diagonal weighting matrix,

$$\mathbf{W} = \begin{bmatrix} w_1 \frac{1}{\mu_{1,1}} & 0 & \dots & 0 \\ 0 & w_1 \frac{1}{\mu_{1,2}} & 0 & \dots & 0 \\ 0 & \dots & 0 & w_1 \frac{1}{\mu_{1,n_1}} & 0 & 0 & \dots & 0 \\ 0 & \dots & 0 & 0 & w_2 \frac{1}{\mu_{2,1}} & 0 & \dots & 0 \\ 0 & & \dots & & & 0 & w_m \frac{1}{\mu_{m,n_m}} & \end{bmatrix} \quad (2.40)$$

where w_i is the weighting adjustment for the i th event, and $\mu_{i,j}$ is the analyst picked error for the j th pick in the i th event. If all of the w_i are 1, then the picks are just inversely weighted by their error and the events are weighted by the cumulative inverse error of their picks. If the w_i are $\frac{1}{\sum_{j=1}^{n_i} \frac{1}{\mu_{i,j}}}$ then events with more picks are normalized with respect to events with fewer picks. The optimal weight could seem to be somewhere in-between these two extremes, but numerical experiments have indicated little difference between the final model inverted using these two end members so we have chosen to use the former option. After pre-multiplication by the weighting matrix the equation 2.39 is transformed to

$$\mathbf{W}\mathbf{r} = \mathbf{W}\mathbf{J}\delta\mathbf{m} \quad (2.41)$$

2.5.3 Regularization

In general, Equation 2.39 will be inconsistent (not all equations can be simultaneously satisfied) and under-constrained (some model parameters will not be constrained by

the equations). Mathematically this is manifested by the non-existence of \mathbf{J}^{-1} . The normal approach taken in tomography is the application of additional constraints to coerce the system to fit some *a priori* assumptions in the absence of data to the contrary, this process is known as “regularization”. We use the common method of looking for the smoothest model [Lees and Crosson, 1990]. This can be thought of as an application of Occam’s Razer [Constable et al., 1987], the result is the simplest possible model consistent with a prescribed fit to the data. The true earth is certainly more complex, but it must have at least as much structure as the model we generate. A smoothness constraint is applied by requiring the discrete Laplacian operator

$$\begin{aligned} \nabla_{discrete}^2 m_{i,j,k} = & (m_{i-1,j,k} - 2m_{i,j,k} + m_{i+1,j,k}) + \\ & (m_{i,j-1,k} - 2m_{i,j,k} + m_{i,j+1,k}) + \\ & a(m_{i,j,k-1} - 2m_{i,j,k} + m_{i,j,k+1}) \end{aligned} \quad (2.42)$$

at every point in the model to be small; for a totally smooth model the second derivative would be zero at every node. The factor a multiplying the last term of Equation 2.43 allows for the introduction of an anisotropic operator. We think of the Laplacian as a filter on the model [Crosson and Lees, 1989], the filter passes the high wavenumber portion and this is minimized by the regularization equations. Setting a to one results in a filter symmetric along the coordinate axes (figure 2.8 1a-c); setting a to zero results in a 2-D filter, with adjacent layers of the model completely de-coupled; any value between one and zero results in an anisotropic operator (figure 2.8 2a-c) which allows more model variability in the vertical direction than in the horizontal directions. The true Laplacian operator is symmetric in all dimensions while the seven point operator (Equation 2.43) has higher smoothing along the three coordinate axes. A 27 point discrete operator including cross terms can be made which is almost completely symmetric (figure 2.8 3a-c). Numerical experiments with this data set indicate that the 27 point operator produces a result that is no different from the seven point operator. However, since the smoothing for the 7 point operator is strongest

along the coordinate axes, which are typically aligned in the horizontal and vertical directions, models with strong diagonal structure might require the full operator.

There are two common approaches to generating a smooth model: (1) creeping: start with a smooth model and add smooth perturbations ($\delta\mathbf{m}$ from Equation 2.39) on every iteration; (2) jumping: we start with any model and attempt to generate a solution that removes existing roughness from the final model [Chapman and Orcutt, 1985]. Jumping is the strongly preferred method for this problem since the ray-paths change from one iteration to the next and smoothness of the final model is paramount. If we use creeping it is possible to introduce structure into the model in places where it is not required by the final model (figure 2.7). With the jumping formulation any unnecessary structure is immediately removed from the model.

After the addition of the jumping version of the regularization constraints we solve the modified problem

$$\begin{bmatrix} \mathbf{WJ} \\ \lambda\mathbf{L} \end{bmatrix} \delta\mathbf{m} = \begin{bmatrix} \mathbf{W}\mathbf{r} \\ -\lambda\mathbf{b} \end{bmatrix} \quad (2.43)$$

where λ is an arbitrary regularization weighting factor, \mathbf{L} is the regularization matrix, and \mathbf{b} is the roughness of the existing model obtained from

$$\mathbf{b} = \mathbf{L}\mathbf{m}^{(0)} \quad (2.44)$$

2.5.4 Solution of the System

A graphic view of the complete matrix system is shown in figure 2.9. A typical inversion with 2991 events and an inversion grid spacing of 4 km horizontal by 2 km vertical yields a model with 144,144 nodes and 11,964 free hypocenter coordinates. The events generate 51,809 rays and with the addition of the regularization constraints the total system is 207,543 equations for 156,108 variables for a total of 32,399,122,644 elements in the matrix. This system would be impossible to store, let alone solve, on any present computer; however, only 7,257,455 elements in the

matrix have non-zero values for a sparsity of 99.98% (only 0.02% of the elements are non-zero). The system is solved iteratively using the Conjugate Gradient Least Squares method [*Paige and Saunders, 1982*] which allows solution without storing the full matrix or forming the normal equations.

After solution of Equation 2.43 we update the model using

$$\mathbf{m}^{(i+1)} = \mu \delta \mathbf{m}^{(i)} + \mathbf{m}^{(i)} \quad (2.45)$$

where μ is a weight factor. The solution is initially tried with a μ of one and the norm of the system is checked. Since the matrix equation is only a linearization of the true system there is no guarantee that the solution will improve the fit of the model to the data. However, there must exist a value of μ which does improve the overall fit of the model [*Parker, 1994*] unless we have reached an exact local minimum for the non-linear system in which case the norm of the solution vector should be very small.

At the end of each iteration we examine the norm of the solution vector. If the norm falls below a specified value, typically on the order of 1, we consider the solution to have converged to a local minima. There can be no guarantee in a non-linear problem that a global minimum is found.

See Appendix B for a pseudo-code implementation of the code used to solve the full non-linear seismic tomography problem in this research.

2.6 Resolution

There is an eloquent statement of the problem of model resolution in *Parker [1994]*. “When we are confronted with a solution to an inverse problem deliberately built to be as featureless as possible ... we are entitled to ask whether the flat places are merely manifestations of our ignorance of the true structure. If the inversion process is in principle incapable of creating undulations or other structure with a scale finer than that of the constant plateau, this must cast doubt on the necessity of a featureless zone. The alternative is of course that the Earth really is quite smooth in those

regions.” *Parker* [1994] also lays out a qualitative scheme to determine the resolution of a particular data set to specific model features in a linear inverse problem which we call the “spike test”. First we create an artificial model chosen to be a delta function (or a close approximation) at some point. We solve the forward problem and create synthetic data based on this artificial model. Then we invert the synthetic data and see the smallest-scale feature allowed to appear in the model with the current value of the regularization. *Parker* [1994] calls this the resolving function. The width to which this function spreads out tells the scale of resolution for the problem at the point tested.

In the case of the tomography problem we have to make one minor change to this methodology. It would make no sense to define a model which is a delta function, but we can add an approximate delta function as a perturbation to an existing model. Since the portions of the model sampled by the data change as the model changes (the rays take different paths) it is important that the perturbation be small relative to the base model. It is also clear that the resolution varies with the model we choose as well as with position. For example if we choose a constant velocity half-space as the base model, the ray-paths will be nearly straight lines (slightly bent by the perturbation). These rays would sample very different parts of space than rays in a model with large velocity contrasts and sharply bent rays. For this reason, we always perform a resolution analysis after we have chosen a best model, then a perturbation is added to that model. We calculate arrival-times using the finite-difference travel-time calculator and these calculated times become the synthetic data. We invert for a model using the synthetic data and subtract the starting model. We then compare the resulting difference to the perturbation to get an approximation to the resolving function.

The model covers a large amount of space and it is impractical to perform resolution tests over the full space of the model. However, we can approximate the functionality of the “spike test” by applying a variable perturbation across the entire

model. *Spakman and Nolet* [1988] call this a checkerboard test. If we can recover a checkerboard perturbation in a specific portion of the model than we can assume the data is able to resolve features of that size in that area of the model.

2.7 Error Analysis

A fundamental feature of smoothest model inversions such as this one is that any model which fits the data to the same or better tolerance than the one we select must have at least as much structure as the model we present [*Constable et al.*, 1987], however, *there is no guarantee that the structure will be the same as in the model we select*. Since we will take the step of interpreting the features of the model in terms of the geologic structures they represent it is necessary to quantify how the model features depend on the methodology and possible errors in the inversion. In this section I explore two methods on analyzing the “robustness” of a model. A jackknife test is used to assess the dependence of model features on specific portions of the data. And a suite of different starting models are used to check for the existence of local minima in the model and possible different interpretations of the results.

2.7.1 The Jackknife Test

A simple and intuitive, if inefficient, method of determining the dependence of a non-linear model on the data would be to perturb each individual data point and re-derive the model. We could then empirically construct an $n \times m$ (n number of data, m number of model parameters) matrix showing how each model parameter depended on each data point (the variance-co-variance matrix). If we have structures that depend on one, or a very few, data points, then care must be taken in interpretation of those features, we can only be as sure of them as we are of the small amount of data that indicates their existence. Unfortunately in a model with $\sim 50,000$ data points that takes on the order of a day to invert, it is impractical to take this limiting

case and individually perturb each data point.

The simple jackknife test [*Efron and Tibshirani*, 1993] is a method of approximating this functionality. If we have a sample $\mathbf{x} = (x_1, x_2, \dots, x_n)$ and a functional F which transforms the data into a model parameter $\Theta = F[\mathbf{x}]$. Then the jackknife is formed from samples that leave out one observation at a time

$$\mathbf{x}_{(i)} = (x_1, x_2, \dots, x_{i-1}, x_{i+1}, \dots, x_n) \quad (2.46)$$

Then

$$\Theta_{(i)} = F[\mathbf{x}_{(i)}] \quad (2.47)$$

is the i th jackknife replication of Θ . And the jackknife estimate of the standard error of Θ is defined by

$$\widehat{se}_{jack} = \left[\frac{n-1}{n} \sum_n (\Theta_{(i)} - \Theta)^2 \right]^{\frac{1}{2}} \quad (2.48)$$

Of course this still requires us to perform n iterations of the inversion process to calculate this estimate of the error. However, *Efron and Tibshirani* [1993] show that this estimate can fail for some data. A better estimate is the “delete- d jackknife”; instead of leaving out 1 observation at a time we leave out d observations. Unfortunately there is little guidance for the magnitude of d . It should be greater than \sqrt{n} but less than n . Using the delete- d jackknife the estimate of the standard error is

$$\widehat{se}_{d-jack} = \left[\frac{n-d}{d \binom{n}{d}} \sum (\Theta_{(s)} - \Theta)^2 \right]^{\frac{1}{2}} \quad (2.49)$$

where $\binom{n}{d}$ is the binomial coefficient (n taken d times), $\Theta_{(s)}$ is F of the data with d elements removed. In terms of the number of iterations that must be performed this is even worse than equation 2.48 since $\binom{n}{d}$ (the permutations of removing d elements from a set of n) is much greater than n . However, *Efron and Tibshirani* [1993] also state that we can just use a randomly selected subset of the $\binom{n}{d}$ permutations. In

this case the delete- d jackknife estimate of the standard error is

$$\widehat{se}_{d-jack} = \left[\frac{n-d}{d} \frac{1}{m} \sum (\Theta_{(s)} - \Theta)^2 \right]^{\frac{1}{2}} \quad (2.50)$$

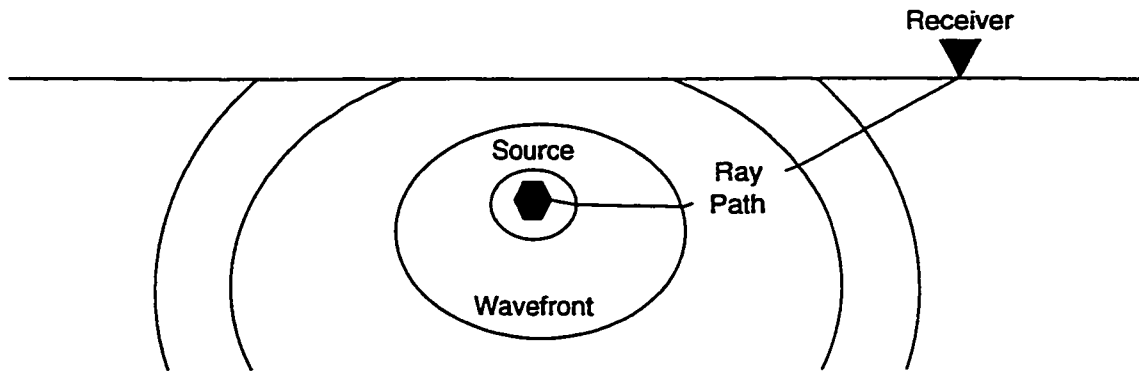
where m is the number of iterations that are performed.

2.7.2 Starting Models

Another fundamental problem with any non-linear problem is the possible existence of multiple minima for the residual vector length. In figure 2.10 I illustrate this problem for a simple two variable model. In the case of a linear problem there will always be a single minima. If we use the perturbation formulation (equation 2.29) then any starting point will eventually lead to this single minima. However, in the non-linear case there are potentially a multitude of minima. Two different starting models, which can be arbitrarily close together, can lead to radically different solutions (figure 2.10 B).

In order to explore the possible effect of local minima and starting model on this problem I will try a number of possible starting models and examine the solutions resulting from each. The three most instructive starting models are; (1) a 6 $\frac{km}{sec}$ half-space. This is the “worst” starting model, it is used to see if the problem will converge to reasonable solution in this region with the available data set. (2) the PNSN standard model (table 1.1), this is the model that was used for the initial location of all of these earthquakes. Derivation of this model is detailed in *Crosson* [1976a, b]. And (3), a 1-D model inverted using a subset of the best of the data that are used for the full tomography problem, this is the “best” starting model for this data set.

(A) Relationship between the source, receiver, wavefronts, and ray path. The wavefronts propagate outwards from the source. The ray path is always perpendicular to the wavefronts and is the path that the signal travels between the source and the receiver.



(B) Geometry for the derivation of Snell's law using Fermat's principle.

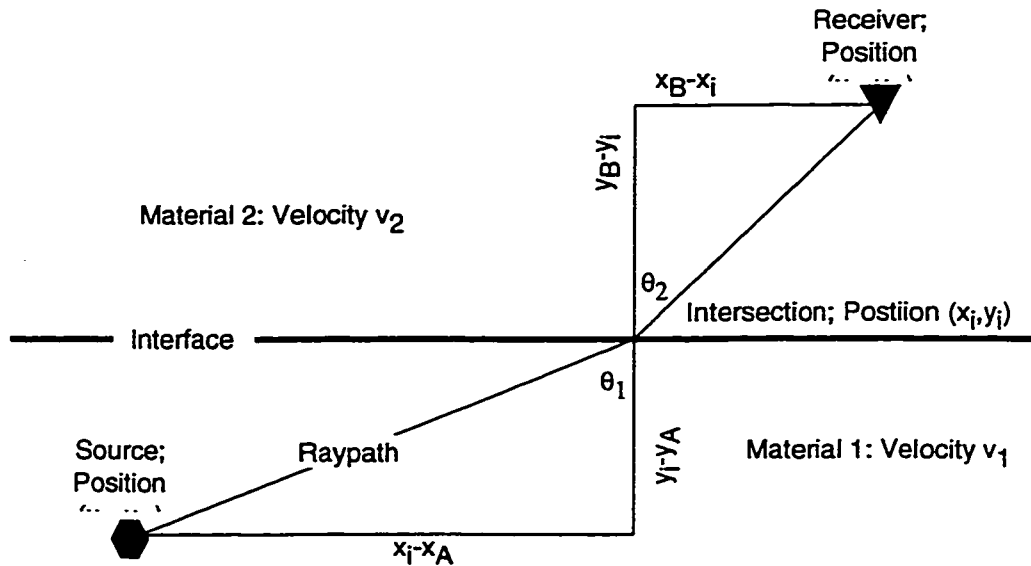


Figure 2.1: (A) Hypothetical wavefronts and ray-path for a specific source-receiver geometry. (B) Geometry for the derivation of Snell's law from Fermat's Principle, derivation discussed in text.

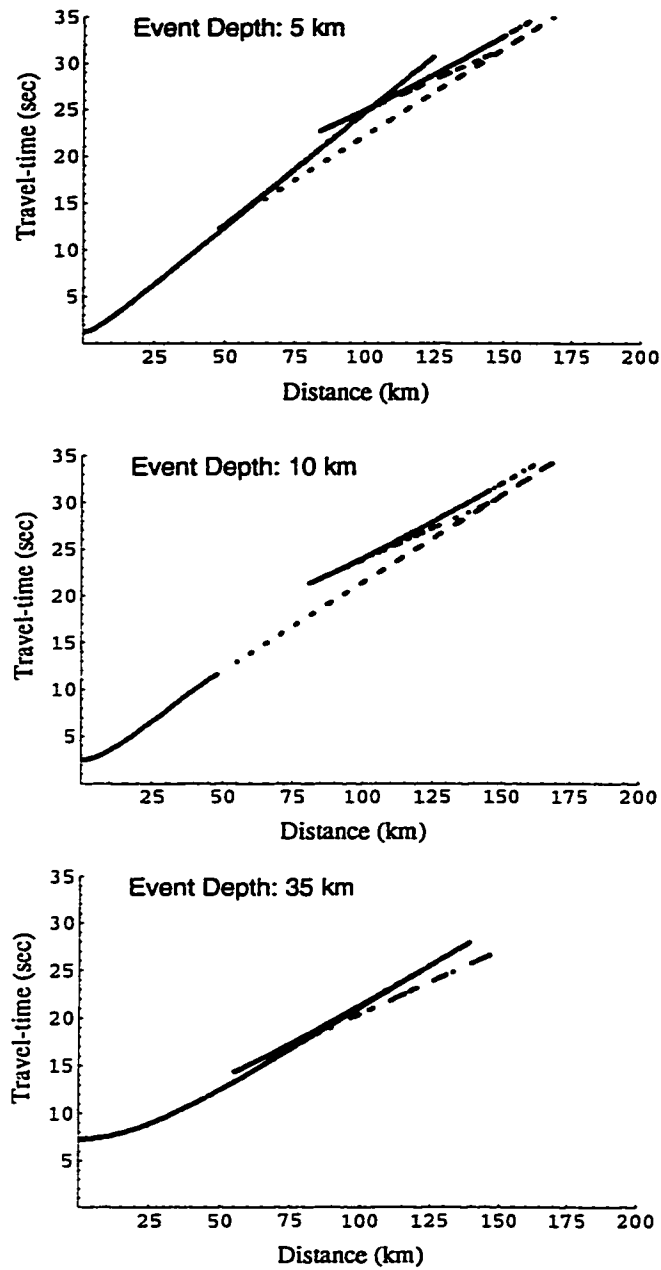


Figure 2.2: Examples of travel-time as function of distance between hypocenter and receiver for hypocenter depths of 5, 10, and 35 *km*.

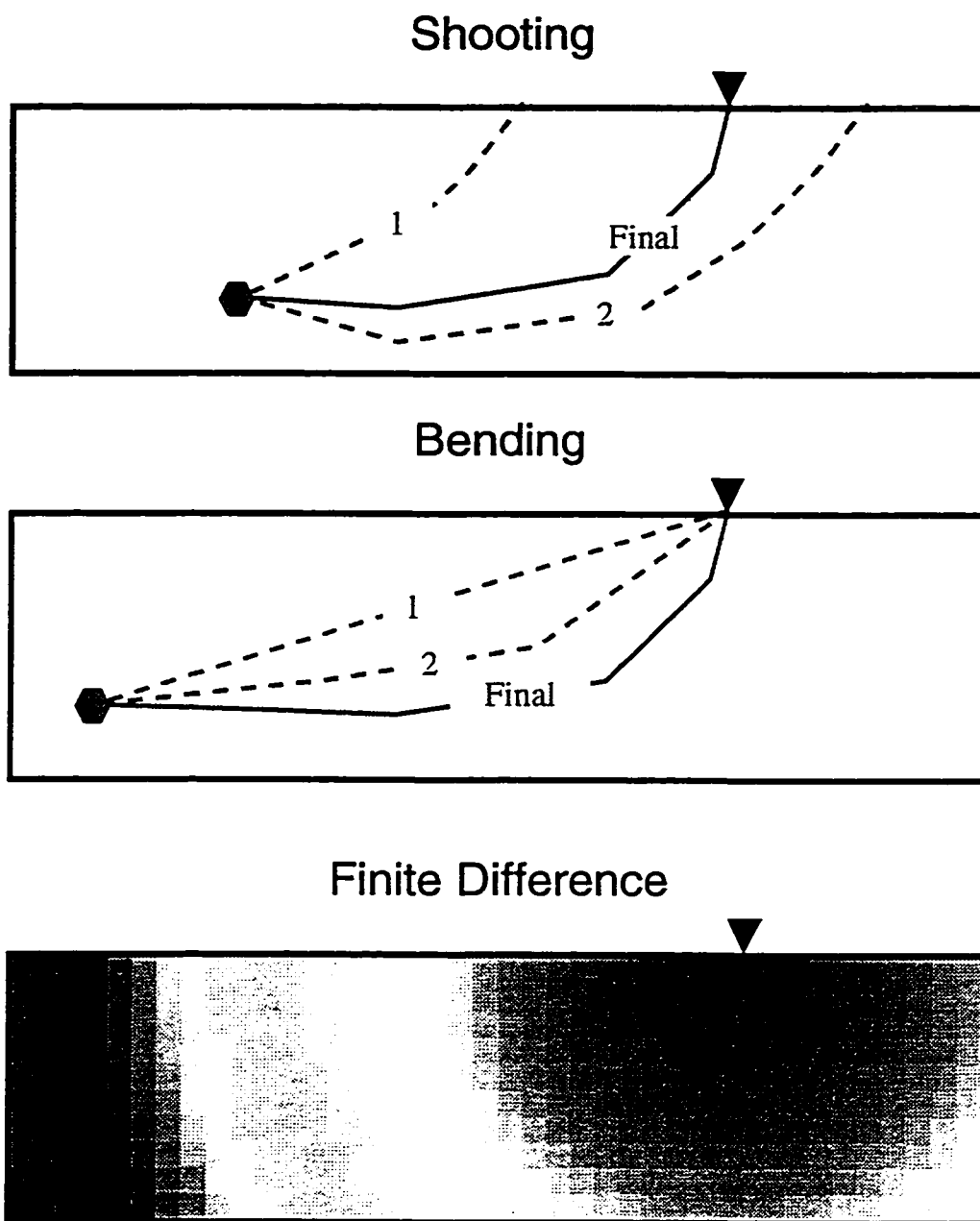


Figure 2.3: Figure showing three methods of calculating travel times. (A) Shooting method, dip (and azimuth in 3-D case) are adjusted until ray connects source and receiver. (B) Bending method, a path is adjusted until it is a ray-path. (C) Finite-difference method, times are calculated to all points on a 3-D grid.

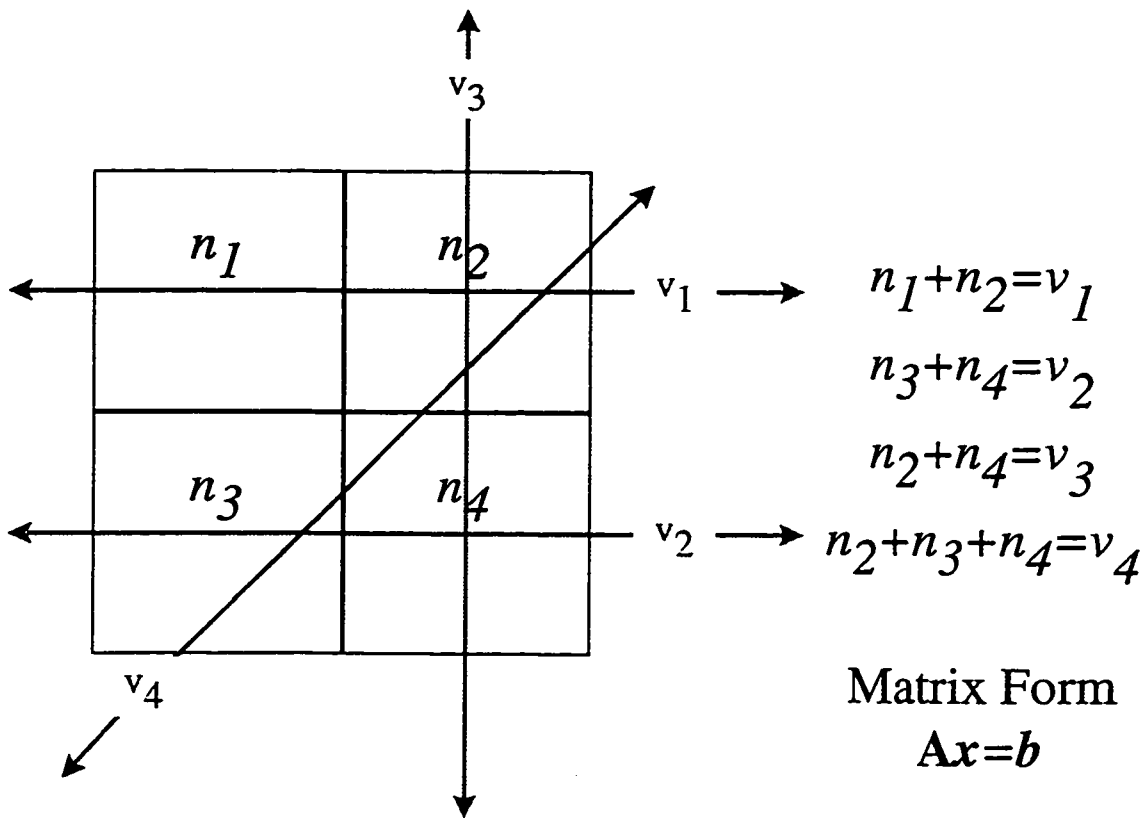


Figure 2.4: Illustration of the linear tomography problem. The problem is linear since the rays are straight lines and the source locations are known.

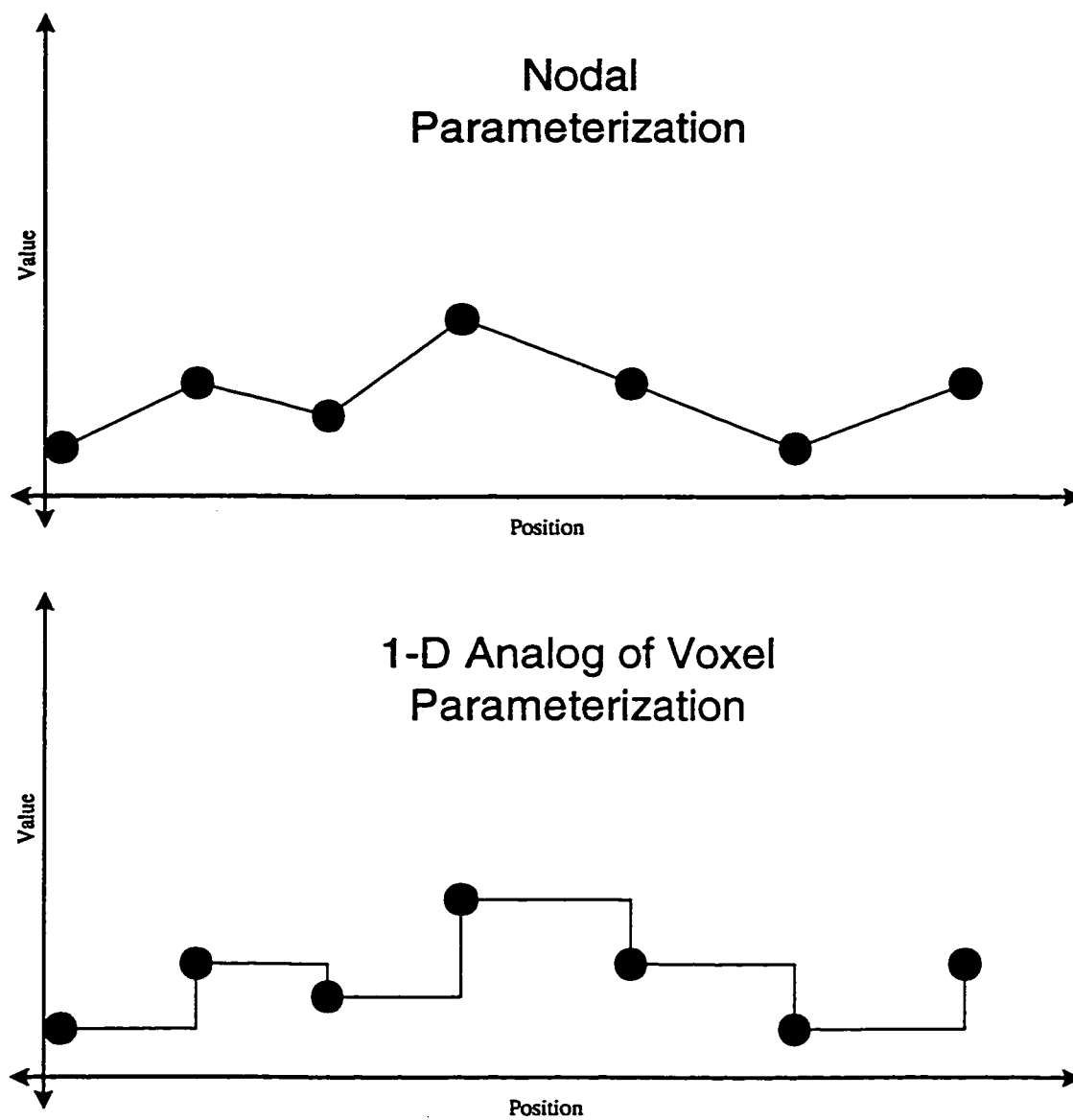


Figure 2.5: Figure showing the models resulting from the 1-D analog of a nodal and a voxel view of a discretized model. Note that the nodal model represents a continuous field while the voxel (in this case pixel) view represents a series of dis-continuities).

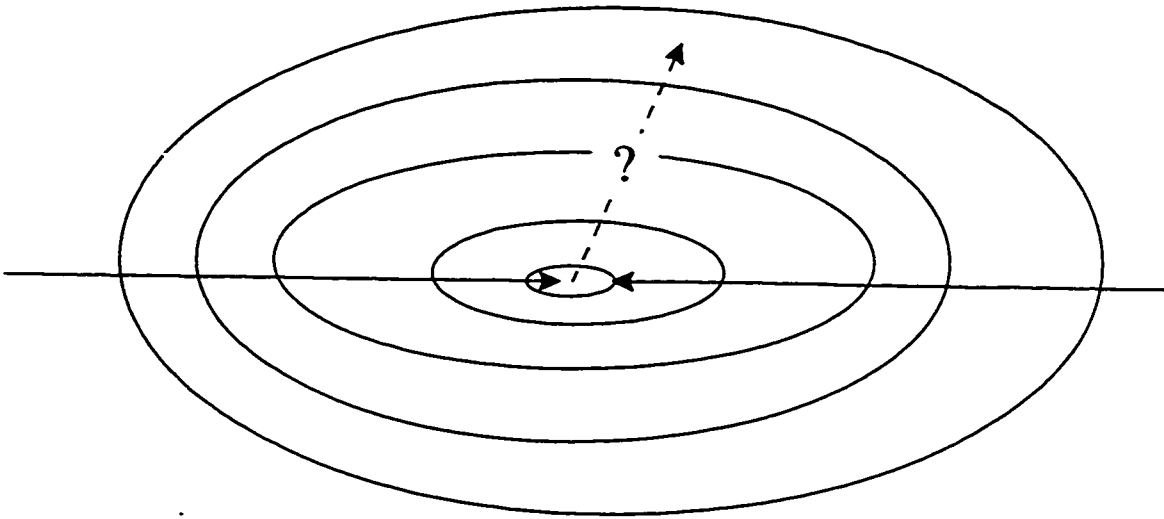


Figure 2.6: Illustration of mountain analogy. To climb the mountain just go uphill, this is the equivalent of finding the ray by back tracing the gradient of the travel-time. To get down the mountain and end up in a specific place is much harder, we do not know which direction to go.

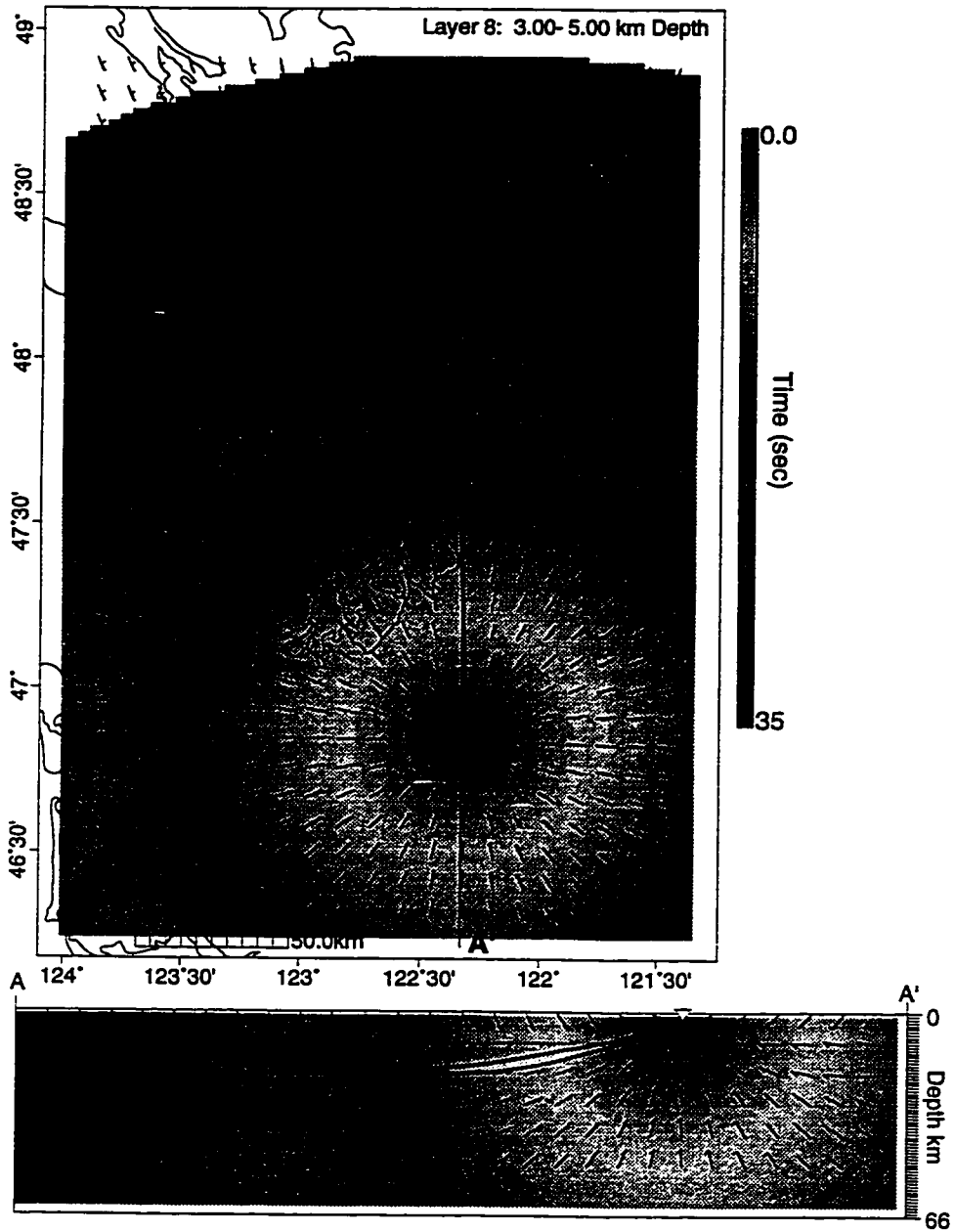


Figure 2.7: Cross section showing a calculated travel-time field and the resulting ray (black ray). Note that the the travel-time minimum is at the station and the gradient of the travel-time (red arrows) always shows the quickest way back to the station. A ray from an event at the same location with an earlier velocity model is shown in green.

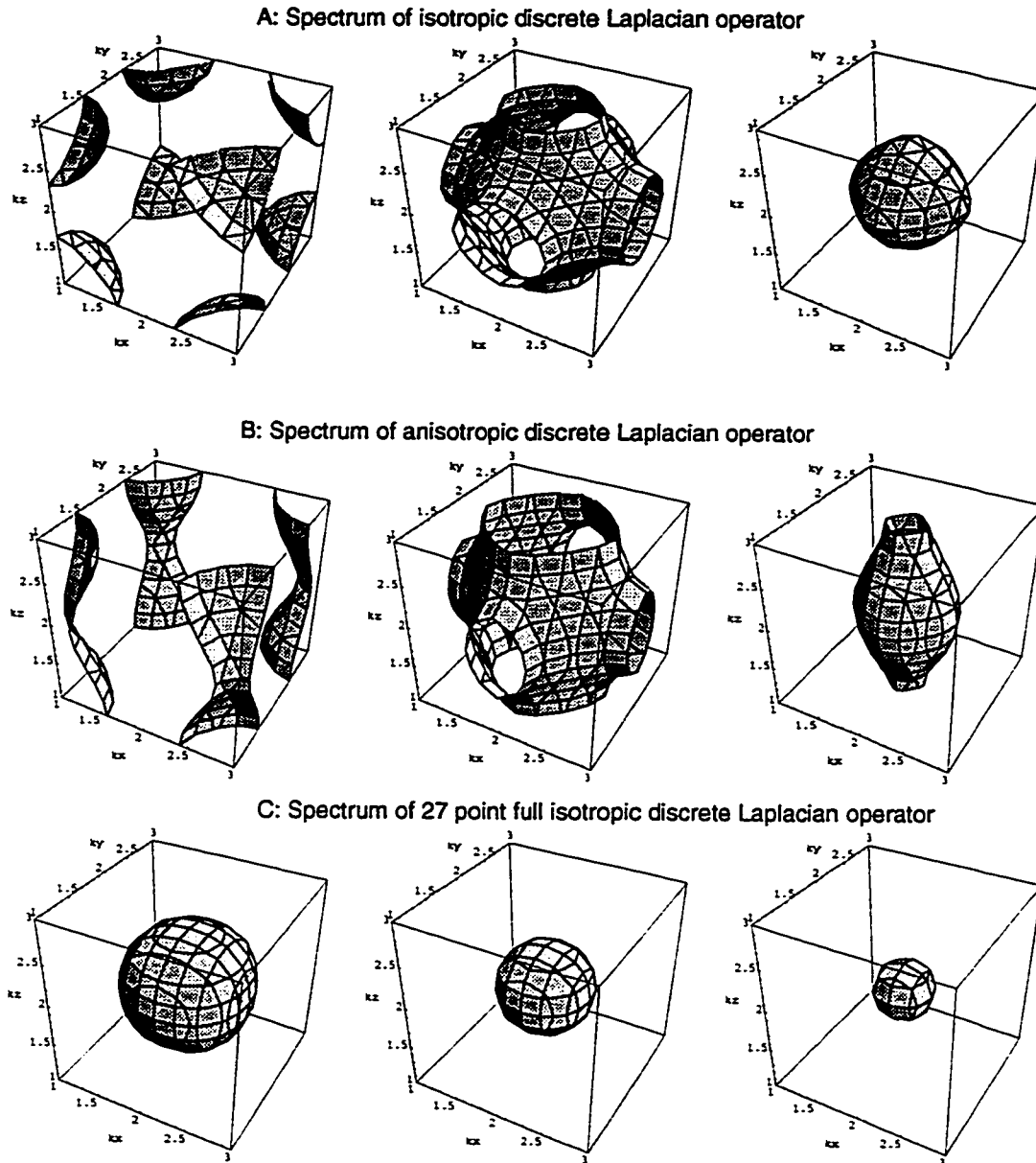


Figure 2.8: (A) Contour plots of 3-D Fourier transform of isotropic Laplacian filter. High wave-numbers are in the middle of the transform and low wave-numbers are on the edges. (B) Contour plots of the transform of an anisotropic filter. (C) Plots of a 27 point fully isotropic discrete Laplacian operator.

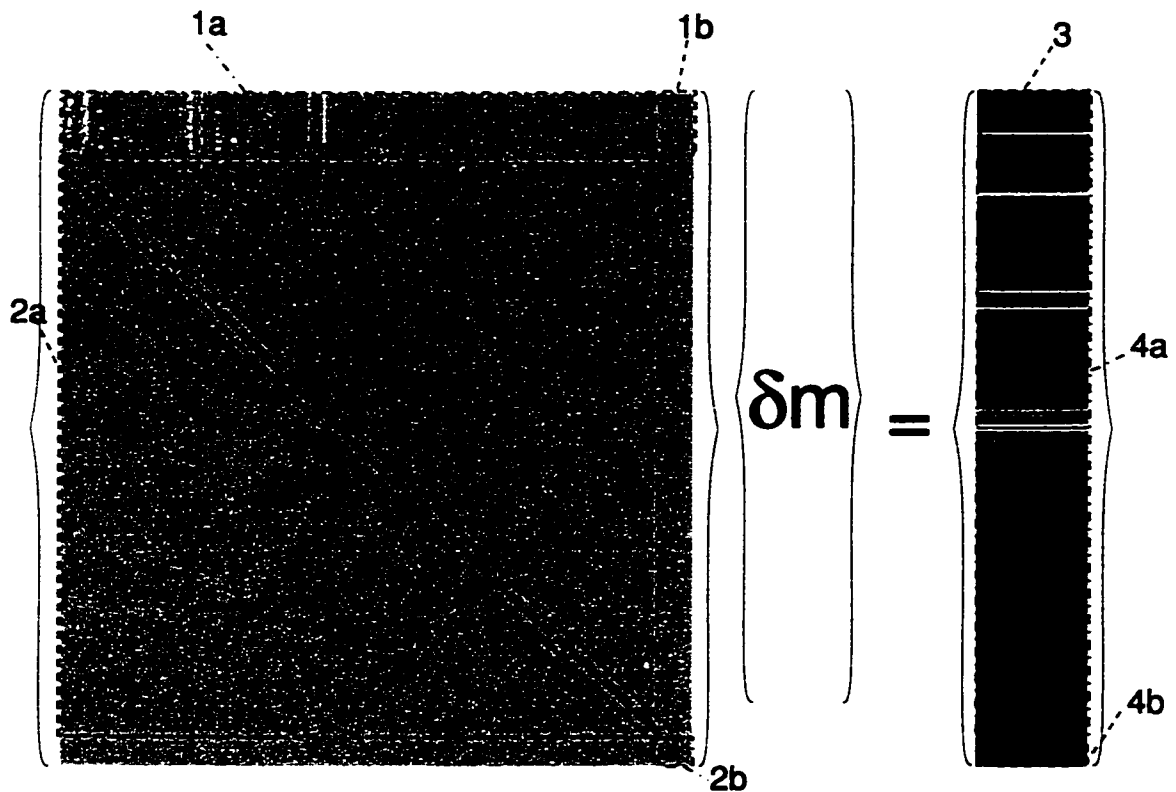


Figure 2.9: Graphic view of the the completely assembled matrix equation illustrating: 1) the sensitivity portion made up of 1a) the slowness sensitivities (all positive) and 1b) the hypocenter sensitivities. 2) the regularization made up of 2a) the slowness Laplacian regularization and 2b) a simple Levenburg-Marquardt regularization to stabilize hypocenter locations. 3) The ray residuals. and 4a) The jumping constraints designed to remove existing roughness from the model. 4b) zero values corresponding to the Levenburg-Marquardt hypocenter stabilization.

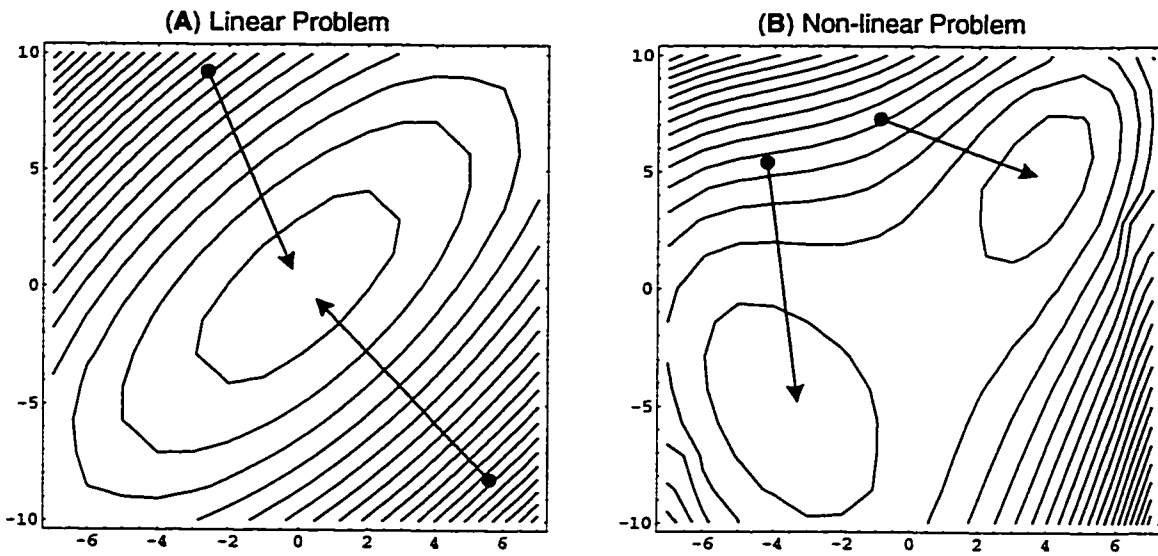


Figure 2.10: The solution to a linear problem will always have a single minima (left). A non-linear problem may have multiple local minima and the starting point can have an effect on choice of final models.

Chapter 3

DATA

This chapter is a description of the data set used to perform a seismic tomography inversion for the GPSR. The data are derived primarily from earthquakes recorded by the Pacific Northwest Seismograph Network (PNSN). Two basic data sets are analyzed. The first data set, which we will label the complete data set (CDS), includes observations of phase arrival-times that are routinely performed by staff seismological analysts. These observations were un-reviewed and were selected using specific quality requirements. The second data set, the high quality data set (HQDS), is generally a subset of the CDS which has been selected for the very highest quality with as much redundancy as possible removed. The HQDS has been completely re-picked and re-analyzed for consistency. Both data sets also include explosions with known hypocenters and external constraint data provided by a 2-D wide angle refraction/reflection line through the eastern part of the study area.

3.1 Seismic Data

The study area (figure 3.1) includes a total of about 100 seismographs operated at various times since 1980. Most are permanent stations of the PNSN. The PNSN is jointly funded by the USGS, DOE, and the State of Washington and monitors seismic activity throughout Washington and in parts of Oregon and Idaho.

Most PNSN seismographs are telemetered to the UW in a multiplexed analog format over phone lines, VHF radio, or microwave links. At the UW the signals are de-multiplexed and digitized at a 100 *Hz* sample rate. At present, incoming signals

are monitored by a local variant of the Earthworm computer program [Johnson *et al.*, 1995]. Other digital acquisition systems have been used during various periods since 1980. All work in basically the same manner. Events are detected based on a change in ratio of the short term average (STA) and long term average (LTA) values of the incoming signals. When an event is detected on an appropriate distribution of stations, the system records all available incoming signals until the STA/LTA ratio decreases below some cutoff value. The event is then available to an analyst. If the event is an earthquake the analyst makes preliminary picks of the arrival-times of P-wave and S-wave phases. If the event is of a moderate to large size ($> 3.0 M_c$) the analyst can sometimes obtain additional data from PNSN broadband stations that are not continuously telemetered or seismographs maintained by other organizations such as the Canadian National Seismograph Network at this time. This analysis produces observed arrival-times and associated errors from the original data.

The seismic data used in this project has all been collected by the PNSN since 1980; prior to 1980 the PNSN data were recorded in an analog format which was of a lower quality than the more recent digital data. Furthermore, the earlier analog records cannot easily be checked for accuracy. Since 1980, the PNSN has recorded a total of approximately 8000 earthquakes within this region.

3.1.1 Construction of CDS

The CDS was selected from a research data set from the PNSN data maintained by Professor Robert Crosson. Cross checks were carried out with the master catalog for the PNSN to ensure that significant data were not overlooked.

In order to select earthquakes with well constrained locations, I included events within the study region that meet the following criteria in the initial data set designated CDS. (1) Events with a magnitude of greater than or equal to $2.5 M_c$. There are 421 events of this size. (2) Events with at least 10 P-picks and having both "quality factors" B or better. Quality B translates to a maximum RMS of 0.3, a

maximum horizontal error of 2.5 *km*, a maximum vertical error of 5.0 *km*, a maximum gap of 135°, and a maximum distance to the nearest station of twice the event depth or 10 *km* whichever is greater. There are 2360 events that meet this criteria. (3) Events with more than 20 P-picks. There are 1858 events that meet this criteria. Some events may meet two or even all three criteria, the union of all these subsets consisted of 3429 earthquakes.

3.1.2 Earthquake Relocation

Routine earthquake location for the PNSN is done using a variation of Geiger's method and a 1-D velocity model with station corrections [Crosson, 1976b]. The 1-D model is parameterized as a set of constant velocity layers with discrete boundaries. Since the layered model is significantly different from the 3-D node parameterization used in the tomographic inversion, it is advantageous to relocate the earthquakes with a method tailored to work with the 3-D model. Nelson and Vidale [1990] have shown how earthquakes can be located without the need for iteration required by Geiger's method. Travel-times are calculated from each station to every point in the model using a finite-difference travel-time calculator (FDTT). Then a grid search can be conducted to minimize errors in the calculated arrival-times. This method was also used by Symons and Crosson [1995b] to relocate earthquakes in the GPSR. Since the entire model is searched for the best location, this has the additional benefit of eliminating the possibility of finding a local rather than a global minimum for the earthquake hypocenter.

Since all earthquakes used in this study have more picks than there are free hypocenter parameters (4 parameters), arrival-time data cannot be exactly fit in general. The residual vector, \mathbf{r} , from equation 2.9, is one measure of the misfit. We will define the residual variance as the L_2 norm of the residual vector

$$\psi_r = \sum_{i=1}^p r_i^2 \quad (3.1)$$

Since event location with FDTT involves a search throughout the volume of the model for a location with the lowest variance, the residual variance can easily be plotted as a function of position (figure 3.2 A). Most earthquake location functions based on Geiger's Method provide an error bound based on the assumption of local linearity and the partial derivatives of the travel-time with respect to hypocenter change at the nominal event location. This is why normal methods of locating earthquakes with 1-D velocity models provide only an error ellipse; the true form of the residual variance is not available.

Sometimes the geometry of stations around an event can result in a large uncertainty in the hypocenter even though the event fits one of our criteria for a well located earthquake. A good example of this problem can be seen with a circular distribution of seismograph stations. If the earth is characterized by a 1-D velocity model and seismographs are located in a circle around an earthquake, changing the earthquake depth will effect the arrival-time at all stations equally; and this change can be absorbed into the earthquake origin time. There is a perfect tradeoff between the depth and the origin time of the earthquake. If the station distribution is not a perfect circle and/or the earth is not 1-D then the depth and origin time can be determined but the problem is likely to be ill-conditioned (the location coefficient matrix in equation 2.14 has one very small eigenvalue). Due to the travel-time geometry, this effect can be seen in the error estimate for the Magnitude 4.9 M_c Bremerton earthquake of June 23, 1997 (figure 3.2 B), in this case the close-in station distribution is close to circular and poorly constrains the depth of the earthquake. A poorly determined hypocenter location may be manifested by a large change in the event location as the model is changed by a small amount (because of picking errors and velocity model inaccuracy the best location may be found at negative depths). For this reason, events exhibiting more than a 5 *km* change in hypocenter depth during the change from a layered to a nodal velocity model were eliminated from the data set, this reduced the initial data set from 3429 to 2997 earthquakes. Explosions are

not affected since their locations are known. The locations of the 2997 comprising the CDS are shown in figure 3.1.

3.1.3 Construction of the HQDS

During the period of time over which the CDS was acquired there were a number of different people processing the data using several different software packages. It is even likely that a single person will exhibit changes in the details of their picking behavior over a long period of time. In order to reduce any possible bias I selected a subset of 1004 of the best earthquakes from the CDS to be re-picked. This is the HQDS, later in this chapter I perform tests to assess the resolving power of the two separate data sets. The next paragraph describes how and why these events were selected.

The CDS has a degree of redundancy due to events with similar locations. Since it is impractical to re-pick the entire data set of 2997 events in the CDS, I used a de-clustering technique to select only the best earthquakes in specific volumes of space to reduce the total size of the data set. The idea behind this method is to remove as much redundant data from the inversion as possible while leaving behind most of the unique characteristics. The de-clustering was done in an iterative fashion. Starting with 2 km on-a-side blocks only the “best” single earthquake in each block was retained in the subset. In this case the best earthquake was defined as the earthquake with the greatest number of P-picks. This step was repeated several times using slightly different origins to reduce the effect of the exact block boundaries. The block size was then increased to 64 km³ (4 km on a side) and the process was repeated retaining only the 2 best earthquakes. This process was repeated with blocks of increasing size until the HQDS contained approximately 1000 earthquakes. Since the study area has a much greater horizontal than a vertical extent the larger blocks were selected to have a horizontal to vertical aspect ratio of greater than one. The number of events to retain and the block sizes are shown in table 3.1. They were chosen empirically to

produce a decimated data set of this approximate size. Since the earthquakes with the largest number of picks were retained in the data set, the total number of rays was only reduced by approximately a factor of 2 (from 52370 in the CDS to 22265 in the HQDS) even though the number of earthquakes was reduced by a factor of nearly 3.

Table 3.1: Declustered Puget Sound Earthquakes

Block Size (H km x V km)	Allowed/Block	Remaining	Deleted
Original Data Set	–	2973	–
2 x 2	1	1918	1055
4 x 4	2	1741	177
8 x 5	3	1436	305
16 x 5	4	1004	432

I then personally re-picked the HQDS in approximately a one month time interval with particular care taken to keep only un-ambiguous high-quality arrivals and to consistently pick reasonable timing error estimates. The timing error estimates are used to assign weights to the individual picks for both the event location and the full tomography problem (equation 2.40). Because of this weighting, it is important that the error bounds on the individual picks be reasonable and consistent.

3.1.4 Comparison of Residuals

During the relocation step the residuals of both data sets increased. This is because there are no station corrections applied to the travel-times when the events were relocated with the 3-D method using the ps2 velocity model. Table 3.2 shows the average RMS for both data sets using both the standard 1-D and the 3-D location methods. There are fewer picks with the 3-D method since only stations that are within the study area are used.

Table 3.2: Comparison of the residuals between different data sets using different location methods.

Data Set	Location Method	Avg. RMS	Max. RMS	Total Picks Used
CDS	1-D	0.274	1.568	109410
CDS	3-D	0.29	1.319	55620
HQDS	1-D	0.27	0.711	46471
HQDS	3-D	0.33	0.685	21853

3.1.5 Comparison of Ray Coverage

Figure 3.3 shows a comparison of the number of rays effecting each node of the inversion grid. The primary difference in the coverage between the two data sets is the maximum number of rays sampling any node. With the CDS, there are nodes that are sampled by over 2500 *rays* (the maximum is 2645 *rays*); with the HQDS, there are no nodes sampled by more than 1000 *rays*. However, the two data sets sample approximately the same portion of the GPSR. This indicates that the HQDS has successfully reduced the redundancy in the CDS without substantially decreasing the amount of unique data.

3.2 Explosions

Both data sets also include 20 explosions recorded by the PNSN with very well determined origin parameters. Explosions are simpler to deal with in the inversion since the origin time and event location are known. There are explosions from two different time periods, the first set of 9 explosions were recorded during the shooting of the UTEP-USGS north-south refraction line in 1991 [Miller *et al.*, 1998; Gridley, 1993] (figure 3.1). The second set of 13 explosions is from the OSU-USGS-UTEP cross Cascades profile shot in 1995 [Luetgert *et al.*, 1995; Parsons *et al.*, 1996]. Both experiments actually used more explosions, but we are able to use only those included within the GPSR. In total there are 373 P-arrival picks from the explosions. Since

these data have small location uncertainties, they are typically given a heavier weight in the inversions.

Table 3.3 shows the explosions used in this study. The table includes, the date, time, and location for each explosion. The table also shows the number of picks, the maximum residual (using the ps2 velocity model) on any pick, and the distance to the furthest station that recorded the explosion.

Table 3.3: Summary of Puget Sound Explosions

Date	Time (GMT)	Lat. (°)	Lon. (°)	Picks	Res. (s)	Mx. Dist. (km)
09/24/1991	05:59	46.776	-121.955	11	0.2	51.4
09/24/1991	06:01	47.338	-121.989	22	0.8	162.1
09/24/1991	06:03	47.899	-122.062	22	2.3	181.4
09/24/1991	06:05	48.478	-122.211	10	0.6	175.7
09/24/1991	08:59	46.492	-121.901	20	1.0	219.6
09/24/1991	09:05	48.242	-122.106	30	0.9	214.1
09/28/1991	07:01	46.715	-123.119	22	0.5	187.7
09/28/1991	09:01	46.495	-123.142	12	0.2	128.5
10/02/1991	09:11	46.715	-123.119	26	0.8	227.6
09/11/1995	07:01	46.587	-123.238	30	0.9	244.5
09/11/1995	07:05	46.487	-121.900	23	0.5	220.1
09/11/1995	07:13	46.557	-122.758	7	0.9	95.7
09/11/1995	10:07	46.584	-121.656	14	0.3	98.0
09/11/1995	10:03	46.568	-122.455	25	0.4	220.9
09/11/1995	10:05	46.525	-122.175	24	0.5	186.8
09/15/1995	07:03	46.568	-122.455	23	0.5	220.9
09/15/1995	07:05	46.487	-121.900	22	0.3	146.7
09/15/1995	10:05	46.525	-122.175	20	0.5	186.8
09/15/1995	10:07	46.584	-121.656	9	0.3	58.1
09/15/1995	10:09	46.573	-123.819	1	0.3	90.6

3.3 External Constraints

A unique feature of this inversion is the inclusion of data from external sources in addition to the seismic data. The Puget Sound region has been the subject of a

number of studies that provide constraints on the seismic velocity structure. The refraction study performed by *Miller et al.* [1998] and *Gridley* [1993] (figure 1.1) provides more than just explosive sources for the travel-time inversion. Multiple arrivals were used during the analysis of this line, providing much more detailed 2-D models than could be inverted from the first arrivals only.

3.3.1 Parameterizing the Miller et al. [1998] Model

The most current model based on the 1991 profile is that of *Miller et al.* [1998]. The *Miller et al.* [1998] model is defined as a continuous P-wave velocity on a vertical plane aligned along the profile. Our first step is to discretize it into observations of velocity at points in space. Then, using the formalism of equation 2.37, we generate one equation for each observation. The density of the interpolation must be chosen to adequately represent the complexity of the 2-D refraction line without causing the matrix (equation 2.38) to become so large that solution of equation 2.43 becomes intractable. I have found empirically that a 2 km grid of points is a good interval at which to discretize this profile with our model resolution.

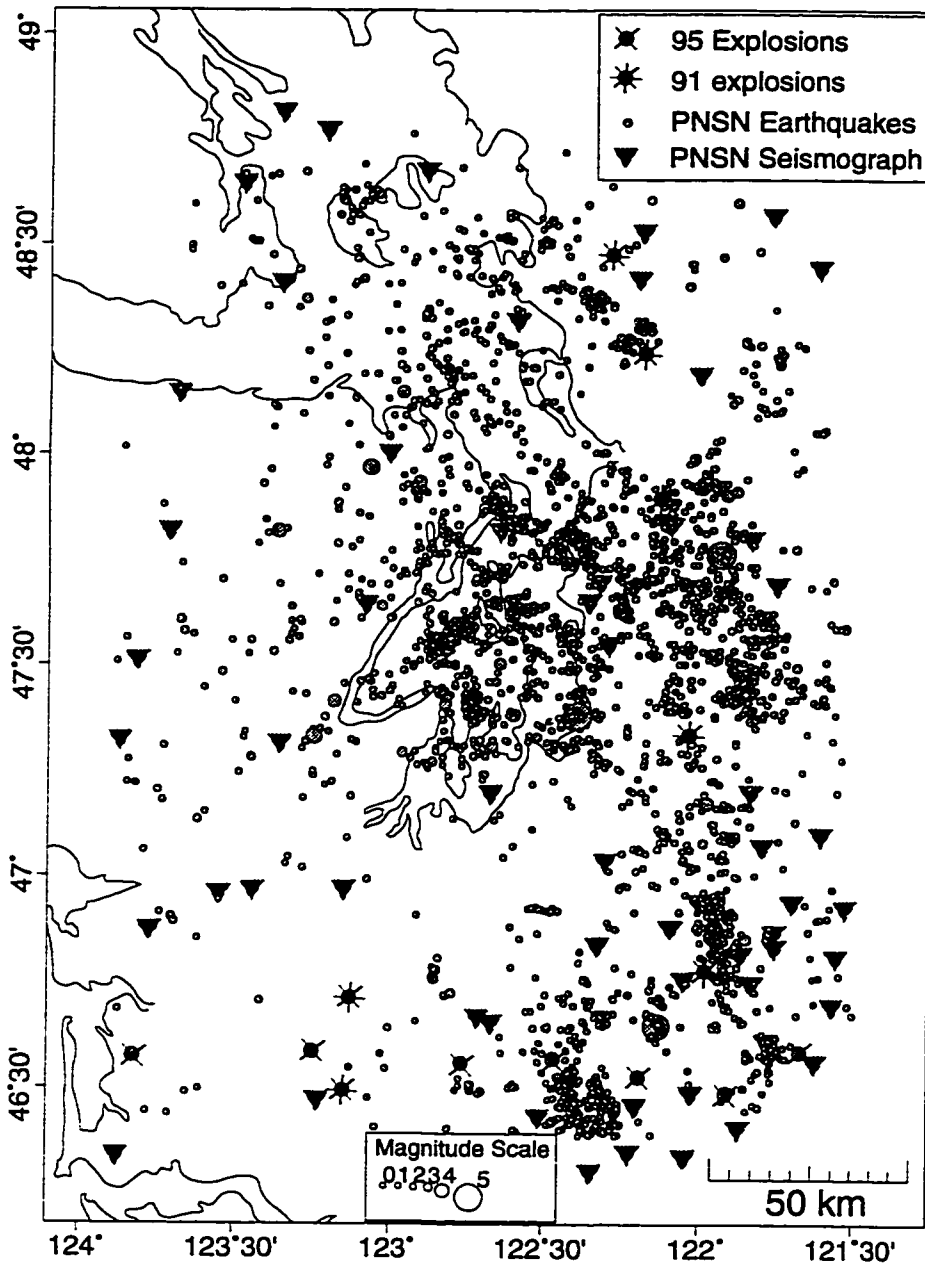


Figure 3.1: Map showing all the stations that have been run by the PNSN during the period from 1980 to 1997. Some stations are temporary and where only run for short periods of time. Also shown are earthquakes and explosions used in the study.

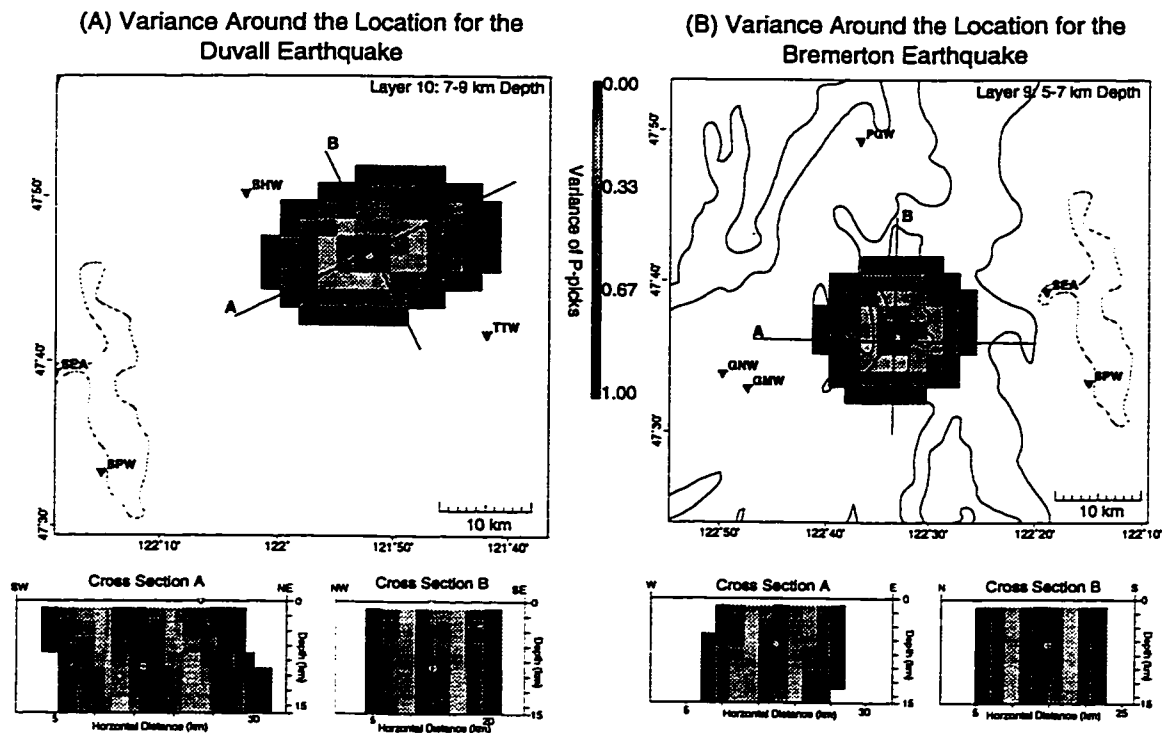


Figure 3.2: Map showing the variance of the May 3, 1996 $5.3M_c$ Duvall earthquake as a function of position (left map and two left cross sections). Right map and two right cross sections are similar plots for the June 23, 1997 $4.9M_c$ Bremerton earthquake. Even though this event is relatively close to the nearest station ($7km$), has a small gap of 45° , and has a total of 29 P-picks within this study area; it still has a poor location estimate (note the “tube” of almost constant variance in the cross section). For comparison I have drawn a black line around the region of constant variance in each of the cross sections.

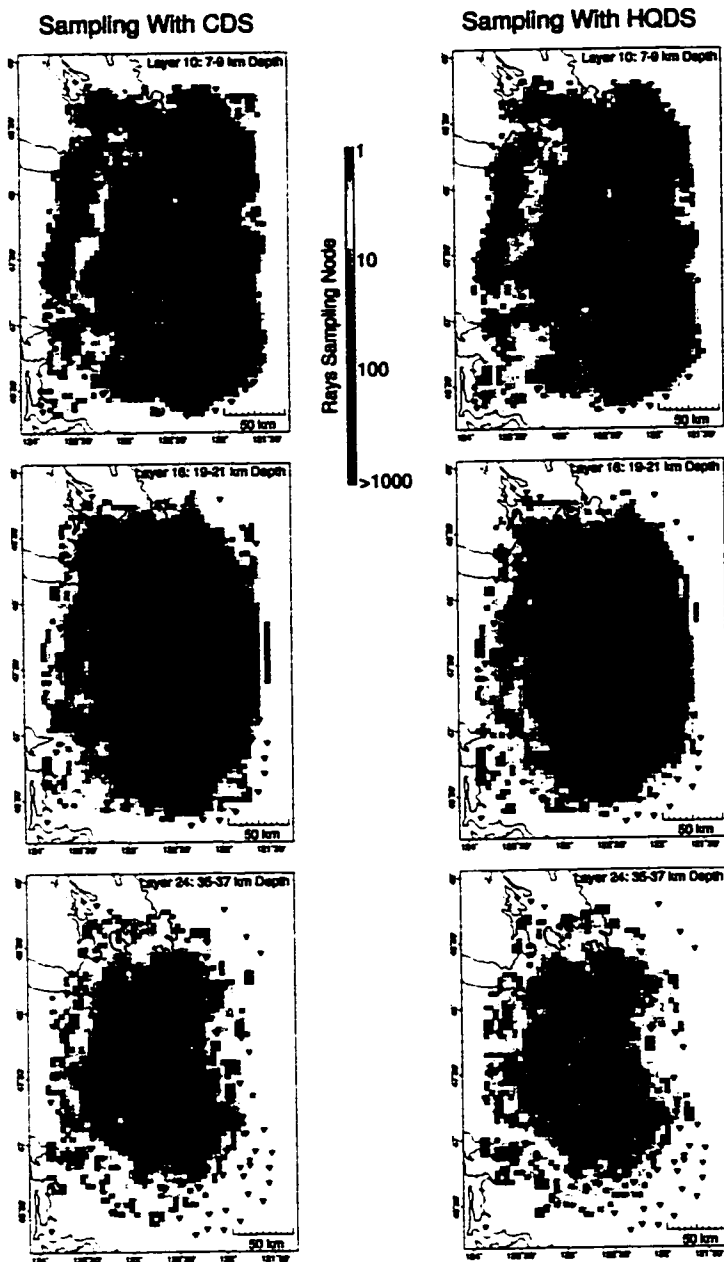


Figure 3.3: Comparison of the sampling between the CDS and the HQDS. The colors show the number of rays sampling a specific node. Note the scale is logarithmic. For the CDS the maximum number of rays sampling any one node was 2645; for the HQDS the maximum was 912. But, the two data sets sample approximately the same portion of the model.

Chapter 4

TOMOGRAPHIC INVERSION

This chapter contains the results of a seismic tomography inversion (described in Chapter 2) on the HQDS described in Chapter 3. We first examine the selection of parameters used in the inversion. Then, we compare the resolution resulting from inversion of the full and reduced data sets described in Chapter 3. Next, we examine the resulting model. Finally, we discuss the resolution and the robustness of the model, critical factors for making a final interpretation of the results.

4.1 Inversion Parameters

As noted in Chapter 2 there are a number of parameters that must be selected before we can perform the tomographic inversion. We have already chosen the study area which defines the spatial size of the model space and determines the source receiver geometry. Three additional important parameters must be selected: (1) The density of the grids used in the travel-time calculation and in the inversion—tighter grids are computationally more intensive, but can provide higher resolution if there is sufficient information. (2) The starting model to use—since this problem is being solved in a perturbation formulation an initial model is required. (3) The value of two regularization constraints—one to control the smoothness of the slowness model, and a Levenburg-Marquardt factor used to stabilize the hypocenter perturbations.

4.1.1 Grid Sizes

As was noted in Section 2.5.2 the grid used to calculate the travel-times and the grid used for the inversion can have different parameterizations. The model is transformed between the grids using tri-linear interpolation.

Travel-Time Grid

Implementation of the finite-difference travel-time calculator (FDTT) used in this process [Hole and Zelt, 1995] requires a cubic grid (the same spacing in the x , y , and z coordinates). Because of computational constraints, I selected a travel-time grid spacing of 2 *km*.

I performed tests comparing the travel-times generated by the FDTT and a 1-D travel-time calculator using a 1-D velocity model. The 1-D model is the ps2 model (table 1.1) which has constant velocity layers with discrete boundaries. As discussed in Section 2.5.1, the discrete boundary can only be approximated with the nodal formulation calculator. As the block size or the node spacing gets smaller to different formulations converge, but for finite spacings the two methods actually represent slightly different models. However, with a 2 *km* grid size, calculated travel-times from the methods appropriate for the different models agreed to within 0.1 *sec* over the central portion of the model with the ps2 velocity model (table 1.1). The 2 *km* square grid uses 567,324 nodes (103x153x36) to represent the target region.

Inversion Grid

The density of the inversion grid is primarily limited by available computer memory. The tomography algorithm is more complex and requires more storage than the travel-time algorithm; for this reason the inversion grid is more sparse than the travel-time grid. The inversion grid used in this study is selected to be compatible with the travel-time calculation grid and has nodes spaced at 4 *km* horizontal and 2 *km* vertical

intervals (a $4 \times 4 \times 2$ km grid). For the GPSR this results in a model consisting of 144,144 slowness parameters ($52 \times 77 \times 36$ nodes). In addition the system will contain $4q$ hypocenter parameters where q is the number of events with unknown locations (earthquakes) included in the problem. For this parameterization, using the HQDS results in a model with a total of 148,160 free parameters. When this project was started in 1994 it was difficult to find a local machine capable of running an inversion with $\sim 150,000$ nodes in a timely manner. In 1998, a desktop PC with a moderate amount of memory can easily run several iterations of an inversion with $\sim 150,000$ nodes in ~ 6 hours.

4.1.2 Starting Model

To find an initial 1-D starting model, we can use the same methodology as we use for the full 3-D seismic tomography problem. Equation 2.43 has no explicit dependence on the type of model. To perform a 1-D inversion, we define the model as a single constant velocity layer for each of the 36 layers of nodes in the inversion grid. No station corrections are applied. We use a 1-D analytic travel-time calculator. Since the layers are constant velocity, the first arrival must either be a direct ray (refracted at each layer interface) or a *critically refracted head wave*. A critically refracted head wave is represented by a ray that travels down from the source to a higher velocity layer and is refracted to travel horizontally along the top of this layer and then back up to the receiver.

The data for the 1-D inversion are earthquakes from the HQDS discussed in Chapter 3. The starting model for this inversion was the ps2 model. The results of the 1-D inversion are shown in table 4.1 and are plotted against the ps2 velocity model [Crosson, 1976b] in figure 4.1. The 1-D inversion converged in 16 iterations. After the inversion the RMS, using the 3-D location method with the 1-D velocity model on the HQDS, dropped from 0.27 sec (ps2 model) to 0.24 sec. Unless otherwise stated, this is the starting model for all subsequent inversions.

Table 4.1: Inverted 1-D Velocity Model

Depth (<i>km</i>)	P-Velocity $\frac{km}{sec}$
0.00	5.89
2.00	5.86
4.00	6.07
6.00	5.98
8.00	6.14
10.00	6.59
12.00	6.43
14.00	6.51
16.00	6.69
18.00	6.61
20.00	6.84
22.00	6.77
24.00	6.81
26.00	6.89
28.00	6.93
30.00	6.68
32.00	6.32
34.00	6.16
36.00	6.37
38.00	7.03
40.00	7.89
42.00	7.90
44.00	7.70
46.00	7.69
48.00	7.82
50.00	7.94

4.1.3 Regularization Parameters

Two regularization parameters are defined for the inversions done in this study: a smoothness constraint λ that controls the tradeoff between the amount of structure of the inverted model and the reduction in misfit; and a Levenburg-Marquardt parameter, ν , used to stabilize the earthquake hypocenters.

Smoothness Constraint

For real inverse problems with errors in the observations, and models that cannot fully represent the real earth, it is important to decide how closely to fit the model to the data. The statistical quantity χ^2 is a useful measure of the misfit of the model to the observations. The χ^2 is defined as

$$\chi^2 = \sum_{k=1}^n \frac{r_k^2}{\mu_k^2} \quad (4.1)$$

where n is the number of observations, r_k is the residual (with mean zero) for the k th observation, and μ_k is the standard deviation about zero of the k th observation. If we assume the residuals are normally distributed with mean zero, then we should choose a model where, on average, the misfit of the observations is equal to the standard deviation of the error in each observation [Parker, 1994]. This corresponds to a $\chi^2 = n$.

Unfortunately, we do not have any *a priori* knowledge of the standard deviation of residuals for a particular observation. However, the estimated uncertainty in the observations is selected by the analyst when the earthquake is picked. Although, it is difficult to determine what these uncertainties actually mean, the units are in seconds. I interpret the uncertainties as the approximate standard deviations of the observations. The actual residuals are not, in general, normally distributed (figure 4.3).

The regularization parameter λ from equation 2.43 controls the tradeoff between how well we fit the data versus smoothness of the inverted model. A higher λ results in a smoother model which normally cannot fit the data as well. For a linear inverse problem, it is always possible to fit the data to the desired χ^2 (given a sufficiently dense parameterization of the model). But finding the correct value of λ to accomplish this task is a subjective process.

Unfortunately, the non-linear problem is more complicated. Different starting models or values of the smoothing parameter can cause the solution to jump into a different local minima. As a result, the tradeoff curve representing the misfit of

the data as a function λ may not be a strictly increasing function. Moreover, the density of the model parameterization is not high enough to allow the reduction of the observation residuals to an arbitrarily low value. Figure 4.2 top shows the tradeoff curve for the tomography problem in this study region using the HQDS. In each case, the inversion was allowed to fully converge. Using this curve I selected a λ of 8, a value at the bottom of the local minimum on the tradeoff curve. This corresponds to a χ^2_n of 11.9, equivalent to an average RMS of 0.11 *seconds*, a reduction from the original 0.24 *seconds* with the best fitting inverted 1-D model (table 4.1). Selection of this value for the regularization parameter was also based on more subjective factors such as the number of iterations required for both the full tomography problem and the CGLS algorithm to converge, as well as the “look” of the model resulting from the various values of λ used in the generation of figure 4.2. The χ^2_n of 11.9 is higher than the optimal χ^2_n of 1. However, given that the error estimates of this data are only approximations picked by the analyst, this is not unreasonably high.

Earthquake Hypocenter Location and Stabilization

Three different earthquake location methods are used in the inversion process: (1) grid search [*Nelson and Vidale, 1990*]-this provides a hypocenter location which is constrained to lie on a node in the travel-time grid. (2) Geiger’s method location-interpolated travel-times are used to refine the hypocenter without constraint to a travel-time node. These first two methods are applied once during a specific application of the tomography process *before entry into the main inversion loop* (appendix C). (3) A perturbation to the hypocenter is then returned as part of the solution to equation 2.43. This refinement to the hypocenter location is calculated on every iteration of the main inversion loop. The last two location methods utilize an Levenburg-Marquardt (LM) regularization factor to stabilize the location. A higher value for this parameter controls the tradeoff between the size of the perturbation to the hypocenter location and the reduction in misfit between the calculated and true

arrival times.

On every iteration of the main inversion loop, the partial derivatives of the travel-times at the current hypocenter location (not constrained to lie on a travel-time node) go into the Jacobian matrix (equation 2.38) and the hypocenter perturbations are returned as part of the solution to equation 2.43. The same LM parameter used in the Geiger's method portion of the location problem is also added to the full matrix (equation 2.43) to stabilize this part of the matrix. This can be seen in the lower right corner of the matrix shown in figure 2.9. For the HQDS, a value in the range of 0.1 to 0.01 provides a good balance between fitting the data and minimizing jumps of the hypocenters. The higher end of this range yields a matrix that converges more rapidly to a solution under the CGLS algorithm [*Paige and Saunders, 1982*].

4.2 Comparison of Data Sets

Because the hypocenters of earthquakes included in the dataset are actually unknown and must be determined in the inversion, more earthquakes mean an increase in the model size (the number of columns in the \mathbf{J} matrix from equation 2.39) and an increase in the number of data (the rows of the \mathbf{J} matrix). For this reason, it is significantly faster to perform an inversion with fewer earthquakes. We would prefer to use the HQDS discussed in Chapter 3 since we are more confident in the observations, but not at the cost of a significant loss of resolution.

Figure 4.4 shows a comparison of a checkerboard test for the full and reduced datasets. There is slightly better recovery of the synthetic model with the full data set, but this comes at the cost of the inversion taking nearly twice as long. With both data sets, the checkerboard is recovered throughout the center of the model to a depth of ~ 55 km.

The results shown in figure 4.4 are for synthetic noise-free data. The checkerboard tests are repeated in figure 4.5 with Gaussian noise proportional to the estimated error

of the actual observed data added to each calculated travel-time. Since the re-picked arrival-times have reduced error because of the more consistent picks the resolution in the re-picked dataset is comparable to the full data set. The higher quality of the data compensates for the reduction in quantity. I use this result to justify the use of the re-picked dataset through the balance of this study.

4.3 Results

Figure 4.6 shows the final inversion results using the HQDS. The regularization weight (λ) for this inversion was 8. The velocity range of the final model is from 4.5 to $8.2 \frac{km}{sec}$. During the course of the inversion, the model roughness ($\| \mathbf{Lm} \|^2$; as defined in equation 2.43) increased in norm from 1.16 to 1.96 (an increase of 70%) and the norm of the data residual vector dropped from 0.00797 to 0.000676 (a decrease to 8.5% of its original value). This is equivalent to a decrease in RMS error from 0.24 to 0.11 s. The drop in the residual vector and the RMS are not consistent because the residual vector is inversely weighted by the estimated errors and the RMS is a simple average. The complete model consists of 36 layers. Rather than display all the layers, I have selected eight representative levels to display here.

In figure 4.7 I show the results of checkerboard tests for the same portions of the model. The results shown in these figures indicate that there is good resolution of features with scales on the order of 20 km throughout the center of the model (only ~ 20 km at the edge of the model is completely un-resolved). The resolution is best at depths between 10 and 30 km, but some large features are resolved from the surface down to a depth of 50 km.

4.4 Error Analysis of the Final Model

4.4.1 Results of a Jackknife Test

In figure 4.8, I show a jackknife estimate of the standard error on the re-picked data set. There are 21019 rays (or observations) in this model so we need to drop between $\sqrt{21019}$ (~ 145) and 21019 data points. I choose to drop $\sim 5\%$ (2400) of the data and perform 20 iterations. In all cases, the results show a generally low estimated standard error of the model in the central portion of the study area. The estimated error at the edges of the model is much larger, but this is expected. In the absence of a ray, the velocity and gradient values of the nearest set of constrained model nodes determine the velocity model values. Since the edges of the model may be some distance from the nearest node, a small change in the value of this gradient can cause a large change in the un-sampled portions of the model.

In figure 4.8 there are two major exceptions to the low estimated model variance through the central portion of the model. In the layer covering 9 to 11 *km* depth (figure 4.8 B) there is region of high error slightly west of the center of the model. Another region of high variance in this figure is seen on three of the four maps in the south central part of the model.

This region is surrounded by 5 PNSN stations: Capitol Peak (CPW); Lucas Creek (LCW); Alpha Peak (APW); Boistfort Mt. 2 (BOW); and Boistfort Mt. 1 (BFW). Figure 4.3 shows the distribution of the residuals for all picks in the HQDS at several of these stations. Of the 5 surrounding stations (only LCW, APW, BOW, and BFW are shown) have an approximately Gaussian distribution of residuals. However, BFW, has a sparse and heavily skewed distribution. It is possible that dropping one or two of these picks could result in a large change in the model, resulting in the high jackknife estimate of variance for this portion of the model.

The location of this spot does correspond with the Centralia coal mine which sets off frequent blasts during the mining process. Unfortunately, for seismologists, the

mining process makes use of what is known as a “ripple blast”. The blast is from several shots each separated by 50 – 100 *m* and the detonation time is staggered. This increases the efficiency for mining, but it makes for an emergent P arrival and a large amount of surface energy which looks very much like an S arrival. Consequently, these blasts are often mis-located. However, with the care taken in the selection of the HQDS we can be relatively certain that none of these blasts remain in the data set.

The lower 2 plots in figure 4.3 show the residual distribution for Snow Dome (OSD) and Port Gamble (PGW), two stations on the outskirts of the region of high error slightly west of the center of the model. These residuals have an an approximately Gaussian distribution and I do not have a good explanation for variance in this portion of the model. However, this does not have a major effect on the interpretation of the results.

Figure 4.8 also shows the results of the jackknife test for the portion of the model below 20 *km* depth. The region of low variance shrinks (and the minimum values increase) in the deep portion of the model. The area with the lowest variance is slightly offset to the west from the center of the model.

4.4.2 *Starting Models*

A fundamental issue with any non-linear problem is the possible existence of more than one solution. In the case of a linear problem there will always be a single minimum. If we use the perturbation formulation (equation 2.29), any starting model will eventually lead to this single minimum (figure 2.10 B). However, in the non-linear case there are potentially a multitude of minima. Two slightly different starting models can lead to radically different solutions (figure 2.10 B).

In order to explore the possible effect of local minima and starting model on this problem I used a number of possible starting models and examined the solutions resulting from each. The three most instructive starting models were: (1) a 6.5 $\frac{km}{sec}$

half-space—this was the “worst” starting model, it was chosen to see if the problem would converge to a reasonable solution with this data set. (2) An approximation to the PNSN standard model, ps2, (table 1.1)—this is the model that was used for the initial location of all of these earthquakes. Derivation of this model is detailed in *Crosson* [1976a, b]. (3) A 1-D model derived in a preliminary inversion as part of this study using a portion of the HQDS—this is the “best” starting model for this data set.

In figure 4.9 the results of inversion performed with these three starting models are displayed. The results are actually remarkably similar. To aid in the comparison, figure 4.10 shows 4 maps and cross sections. The upper left map and section are an average of the inversion results from the three different starting models. The remaining maps and sections show the difference between the average and the individual inversions. The maximum differences in the central portion of the model are $\sim 0.3 \frac{km}{sec}$, slightly higher than predicted by the jackknife estimates. Through most of the model the results from the different starting models are indistinguishable. The major difference is the number of iterations and the amount of time it took the inversion to converge to a solution. For the “best” model (the 1-D inverted model) the inversion converged in 15 iterations and the final average RMS is 0.11. The ps2 model converged in 19 iterations with an RMS of 0.12. The half-space converged in 24 iterations with an RMS of 0.12. The same major structures are present in all three of the final models.

Of course, these models explore only a very small portion of the space of possible starting models. However, I have made an effort to perform tests over as wide as possible a range of starting models.

4.4.3 *Conclusions from Error Analysis*

The results of a jackknife test show that there is generally low standard error through the center of the model in the regions where we attempt geologic interpretation in

Chapter 5. The jackknife estimated variance through the center of the model is typically 0.05 – 0.15 corresponding to expected standard deviations from 0.22 – 0.38 $\frac{km}{sec}$. Where there are exceptions to these low estimates, they are localized and do not affect the overall geologic interpretation. In the upper 20 *km* of the model the highest variance is isolated to two portions of the model where the variance reaches a high of ~ 0.42 corresponding to a standard deviation of 0.64 $\frac{km}{sec}$.

Tests with three different starting models show that the final inverted model has very little dependence on the initial model. The features that I will interpret seem to be very robust.

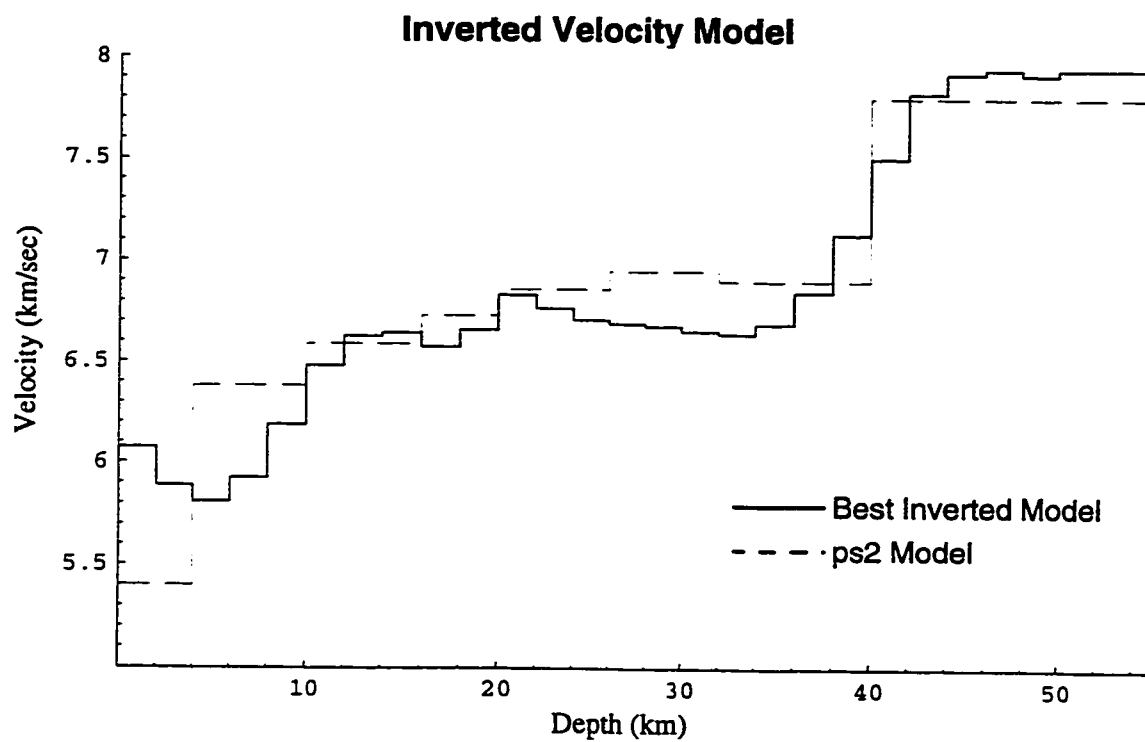


Figure 4.1: Plot of the 1-D velocity model inverted from 100 earthquakes chosen from the HQDS.

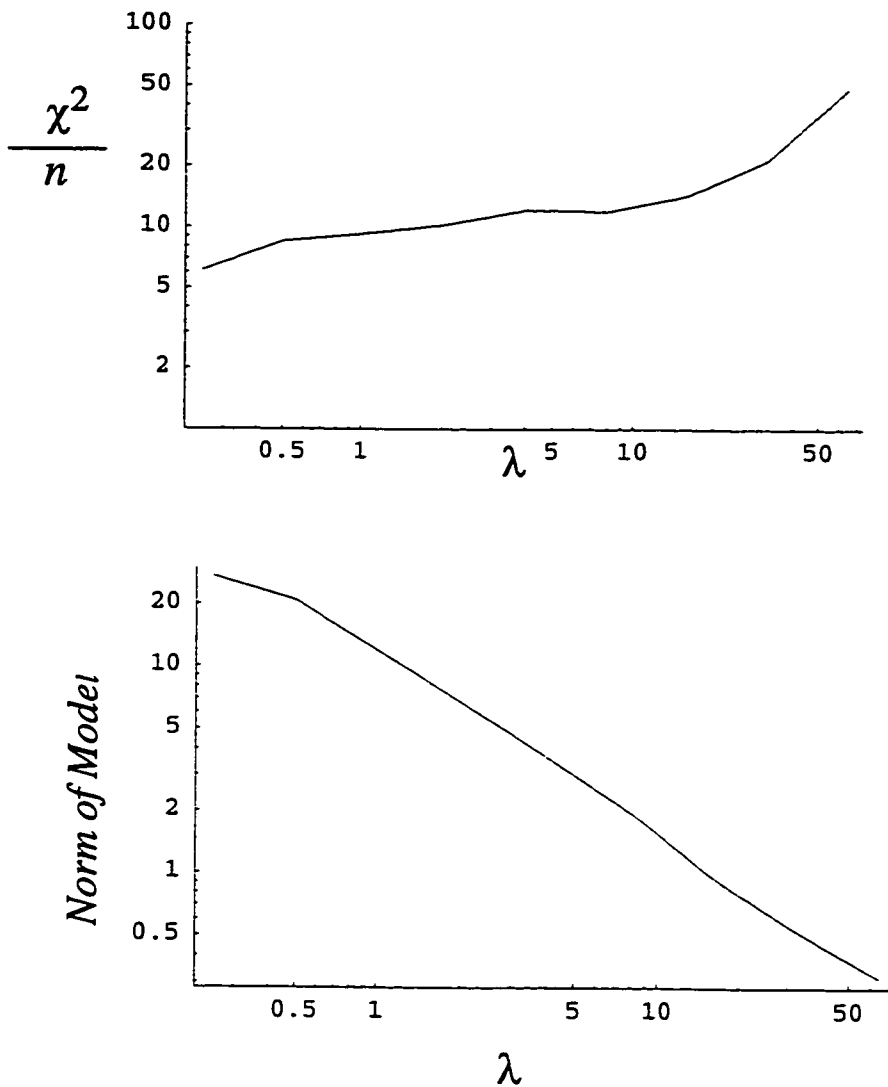


Figure 4.2: Plots of the tradeoff curve.

(Upper) Data misfit, as measured by the $\frac{\chi^2}{n}$, versus smoothing parameter (λ). For a linear problem this would be a strictly increasing function.

(Lower) Model roughness ($\| \mathbf{Lm} \|^2$) versus smoothing parameter (λ).

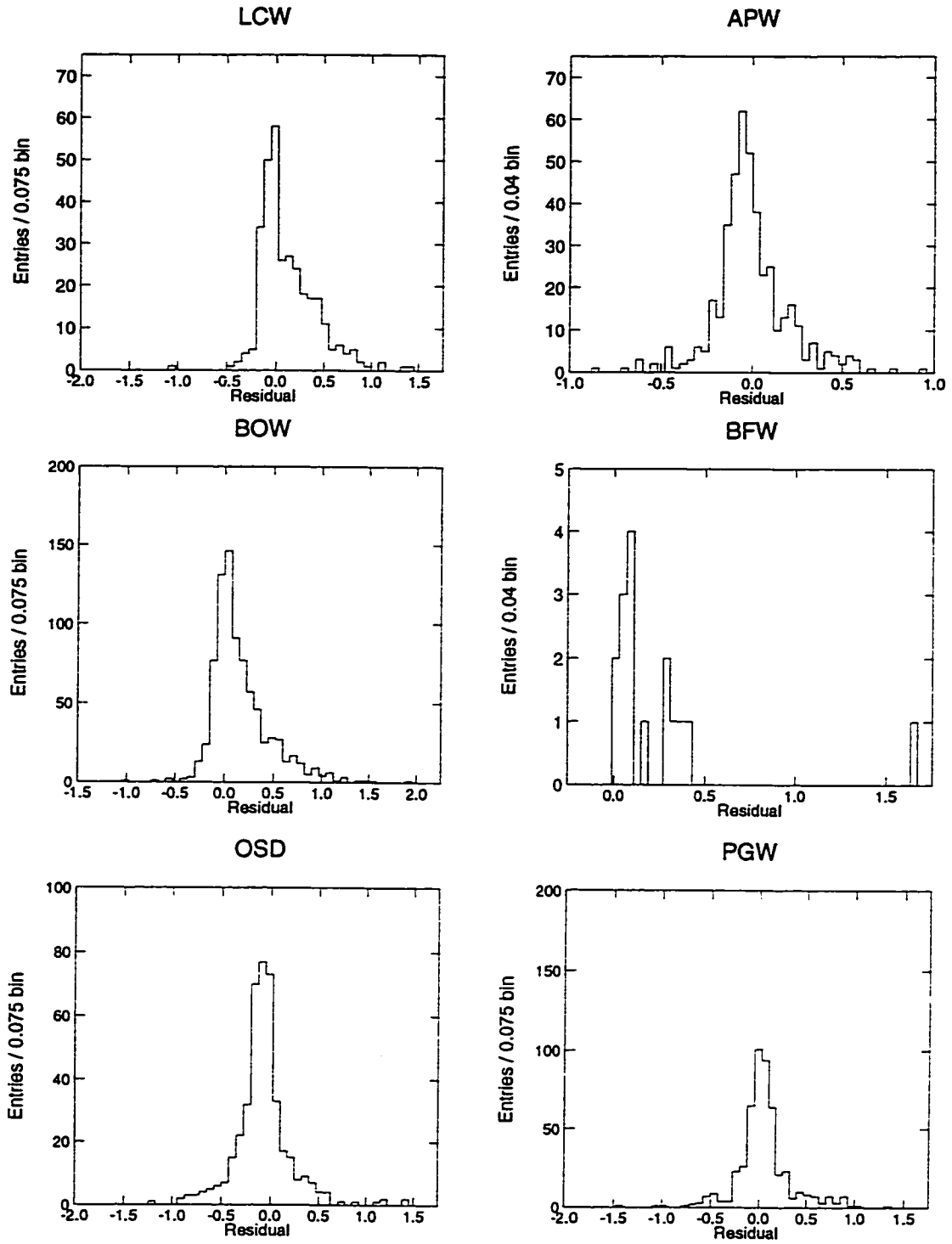


Figure 4.3: Distribution of residuals by station for 6 PNSN stations.

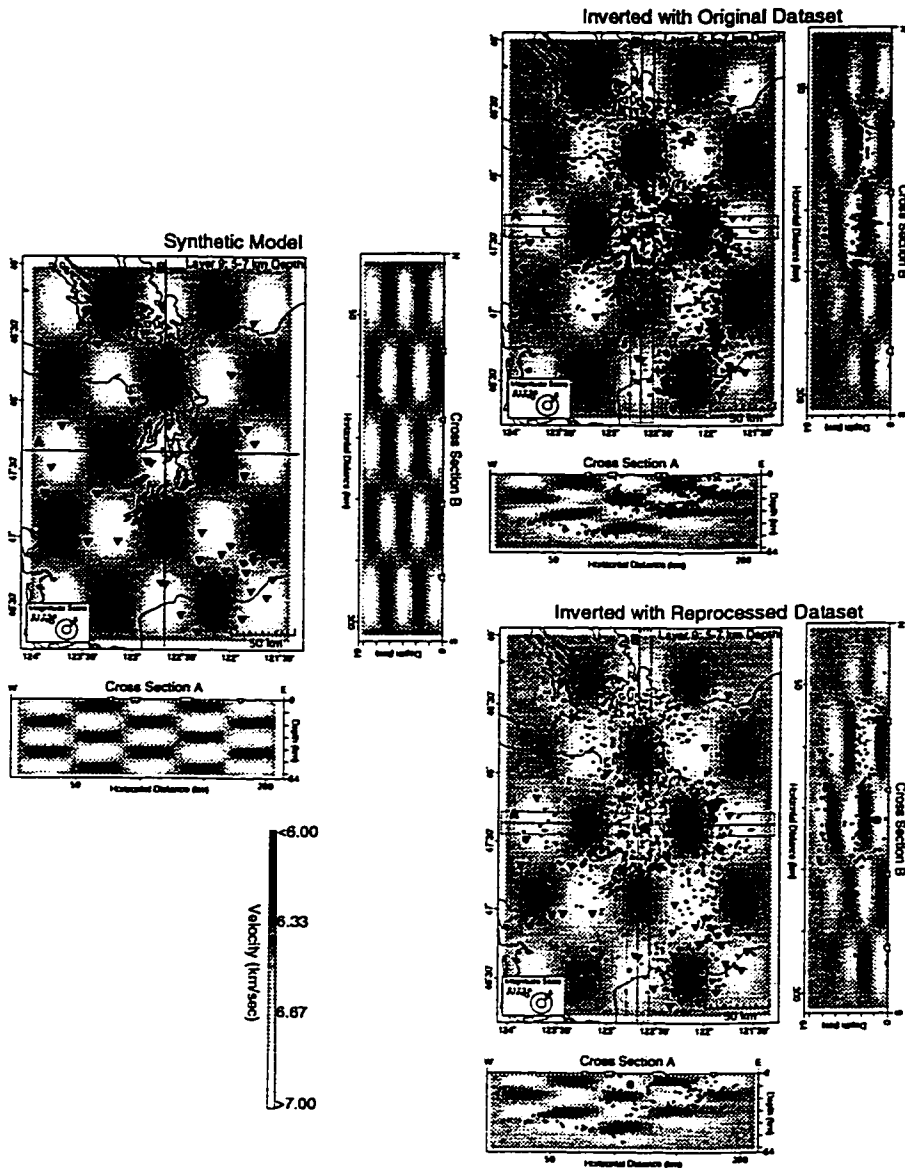


Figure 4.4: Comparison of the results of a checkerboard test using the full and reduced data sets with no noise. Left, synthetic model; upper right, inversion from the full data set; and lower right, inversion from the reduced data set. Note that the resolution in the synthetic model is higher than either of the inversions so a perfect reproduction is impossible.

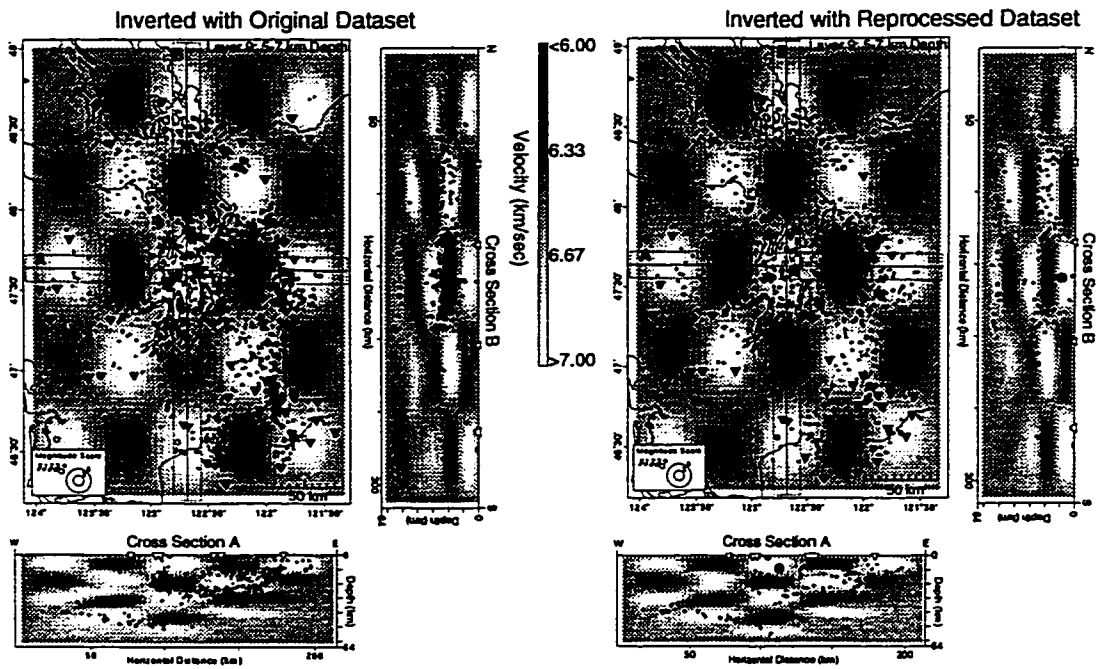


Figure 4.5: Comparison of the results of a checkerboard test between the full and reduced data sets with noise added to each pick. Left, inversion from the full data set; and right, inversion from the reduced data set (see figure 4.4 for synthetic model). Note that the resolution in the synthetic model is higher than either of the inversions so a perfect reproduction is impossible.

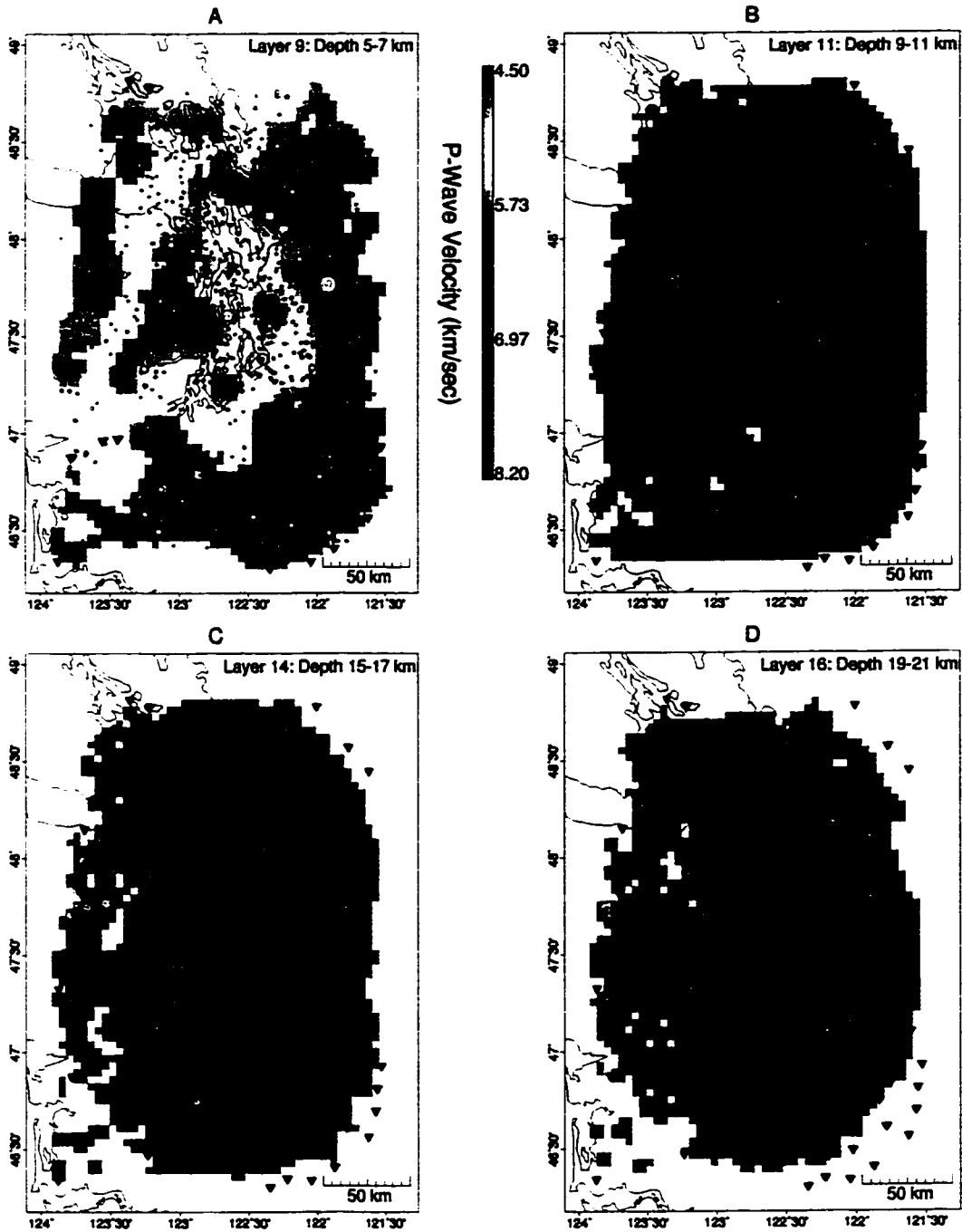


Figure 4.6: Maps showing various layers of the the final model.

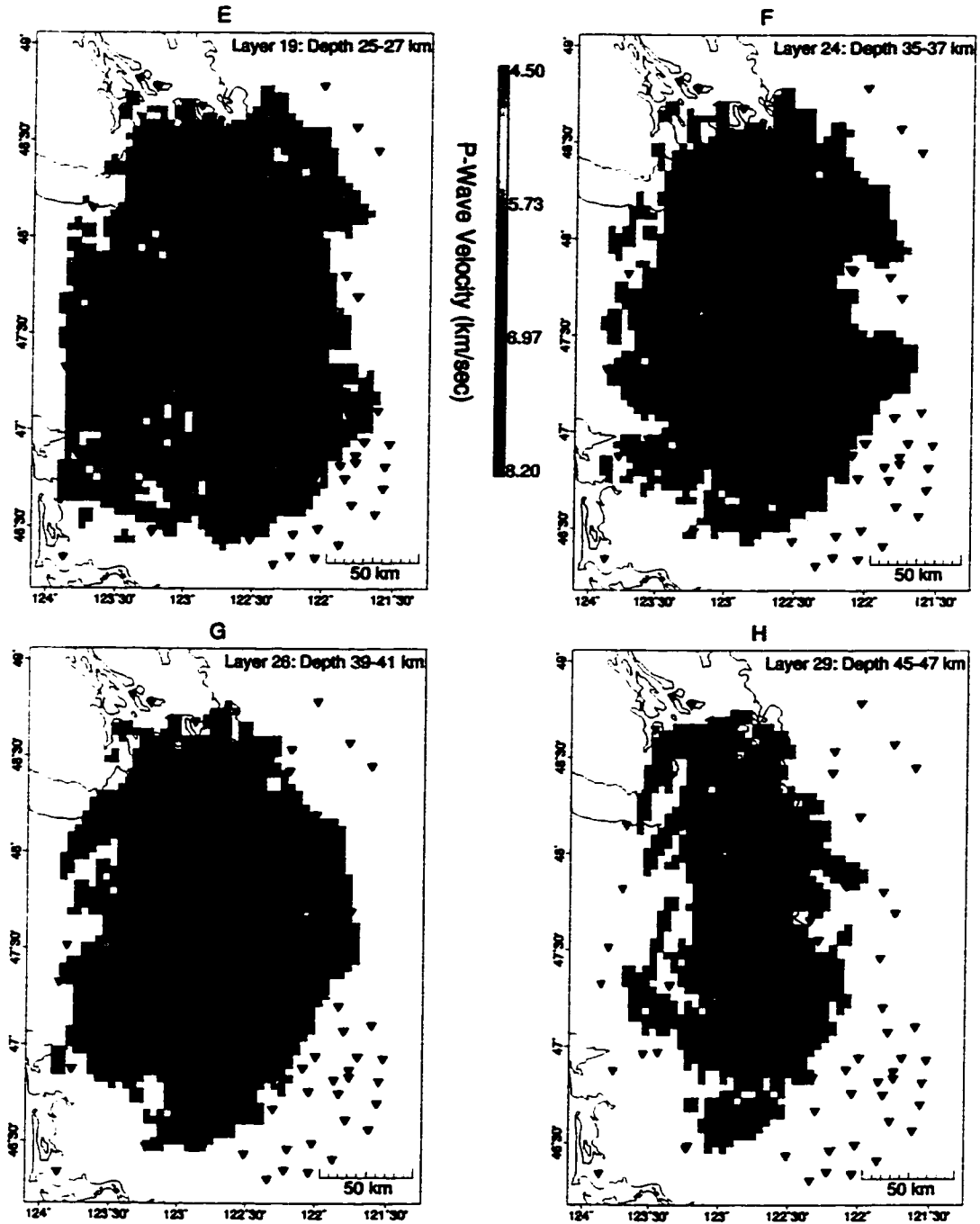


Figure 4.6: (continued)

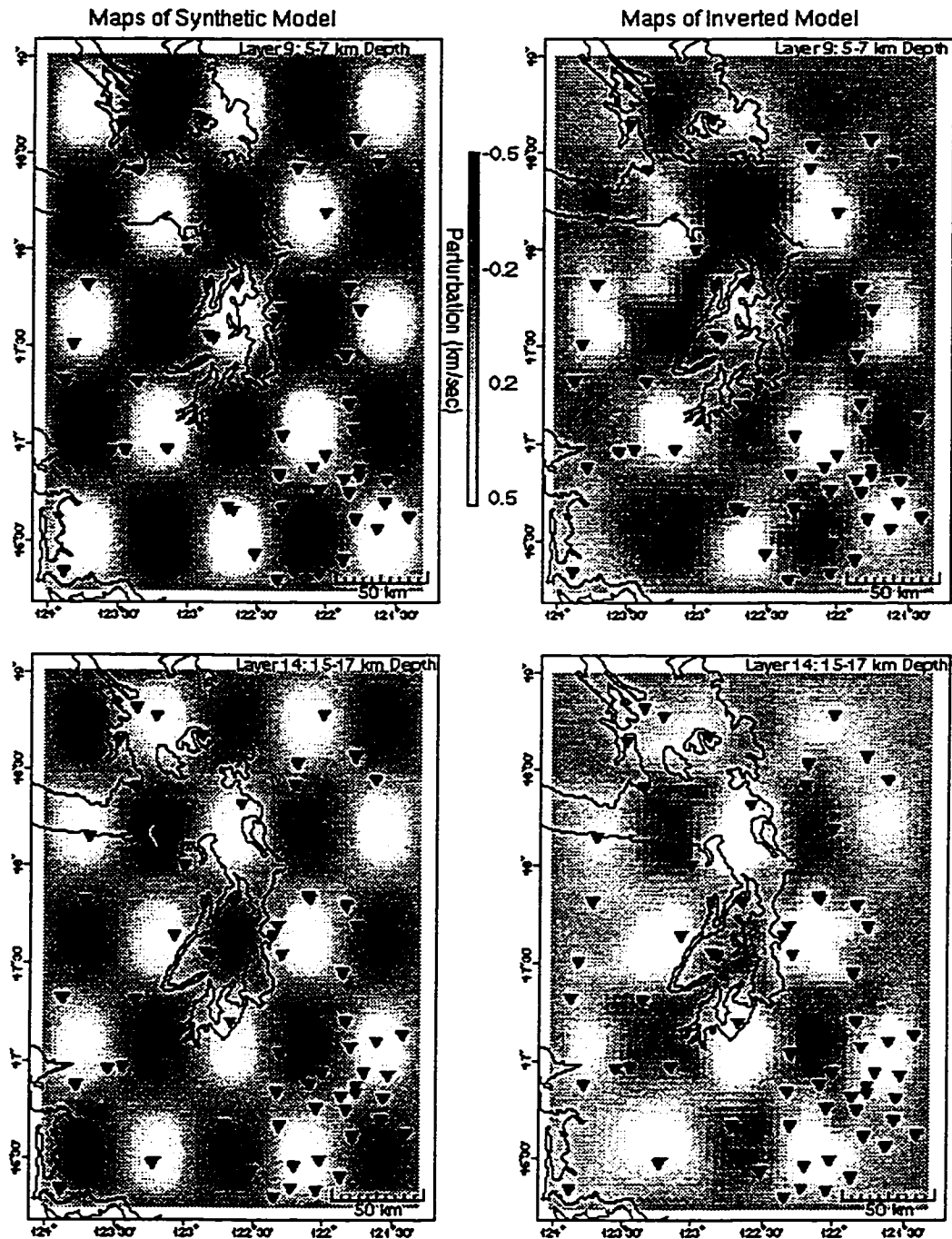


Figure 4.7: Maps showing various layers of a checkerboard test performed on the final model.

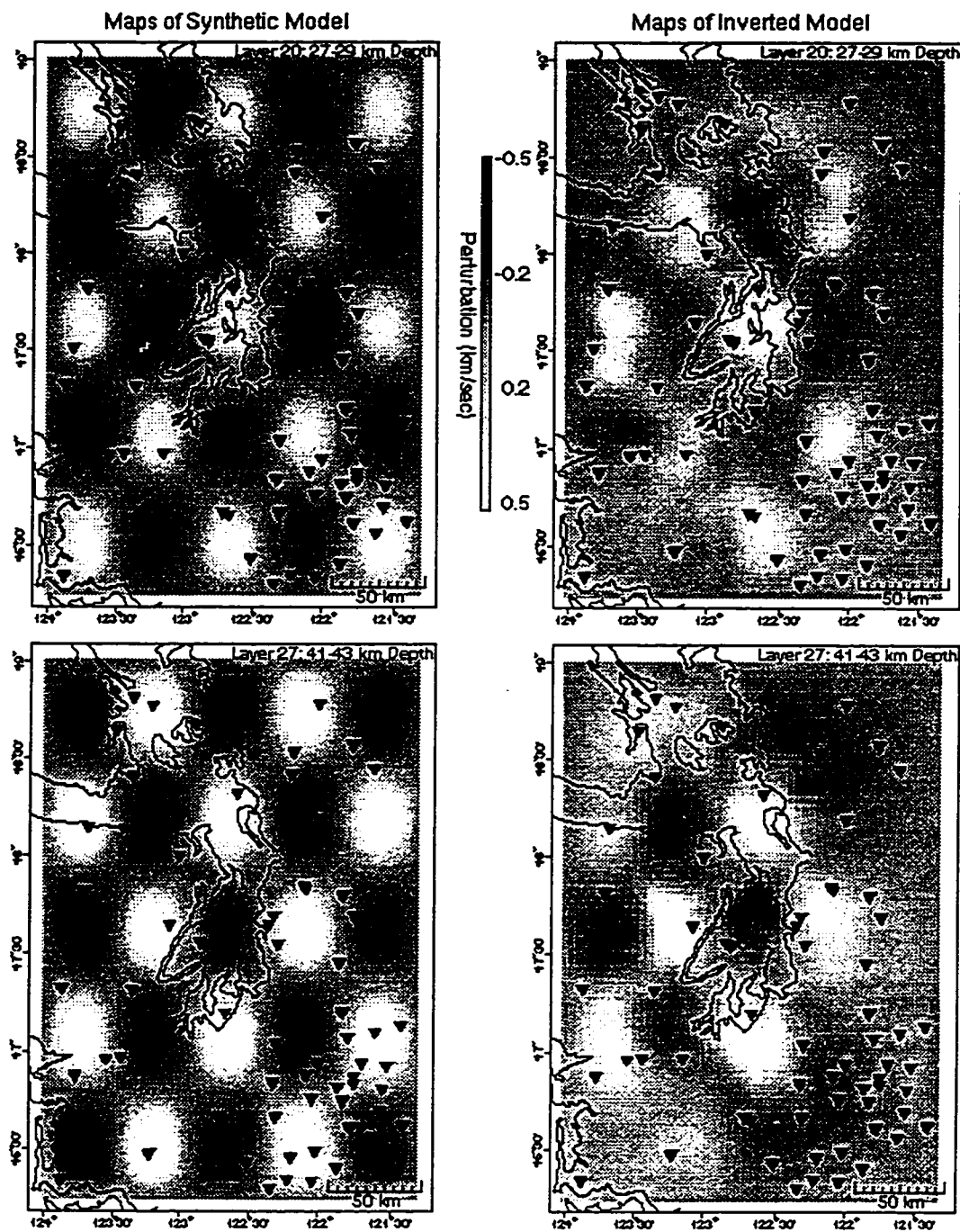


Figure 4.7: (continued)

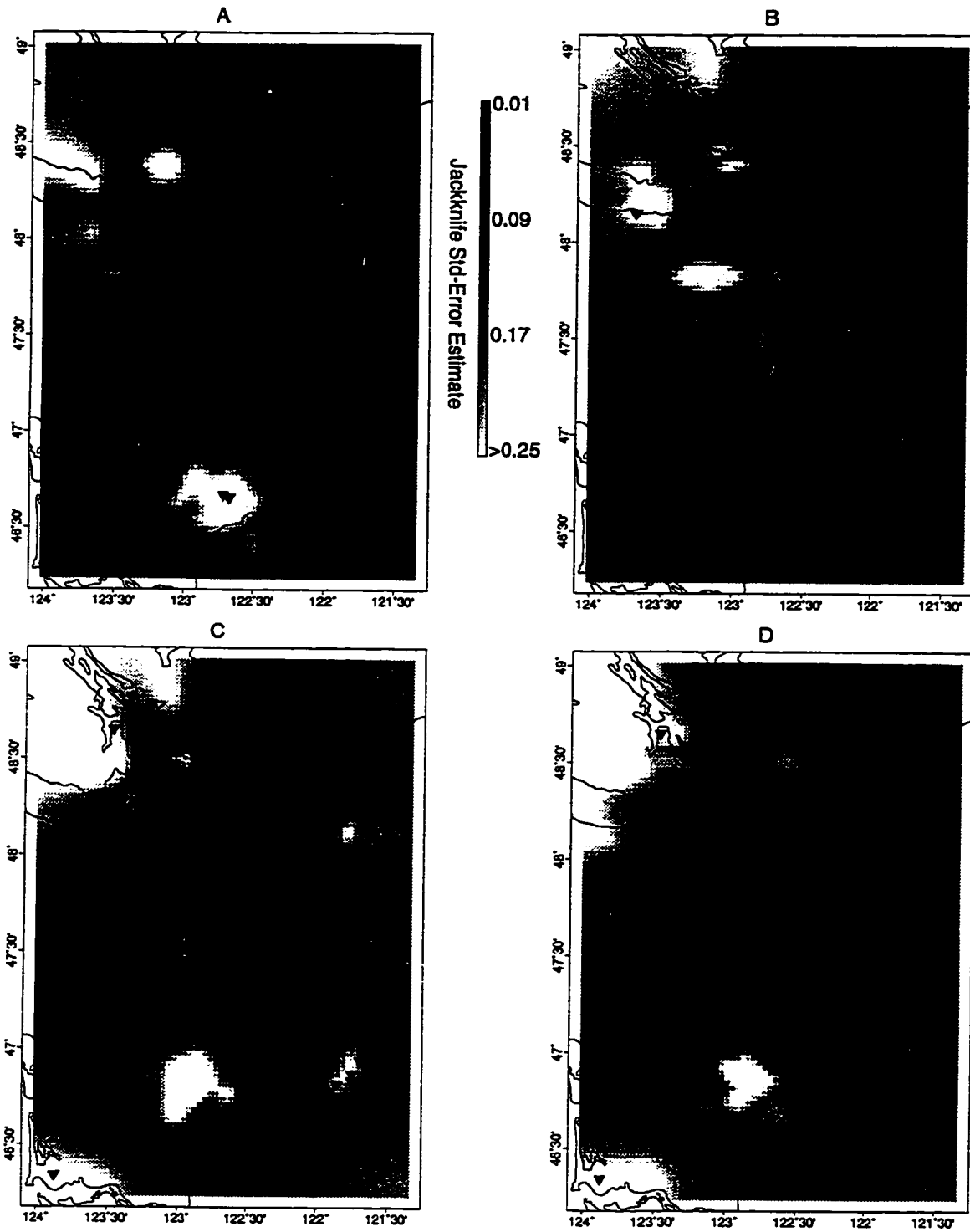


Figure 4.8: Several maps of the jackknife estimate of the standard error. See text for details.

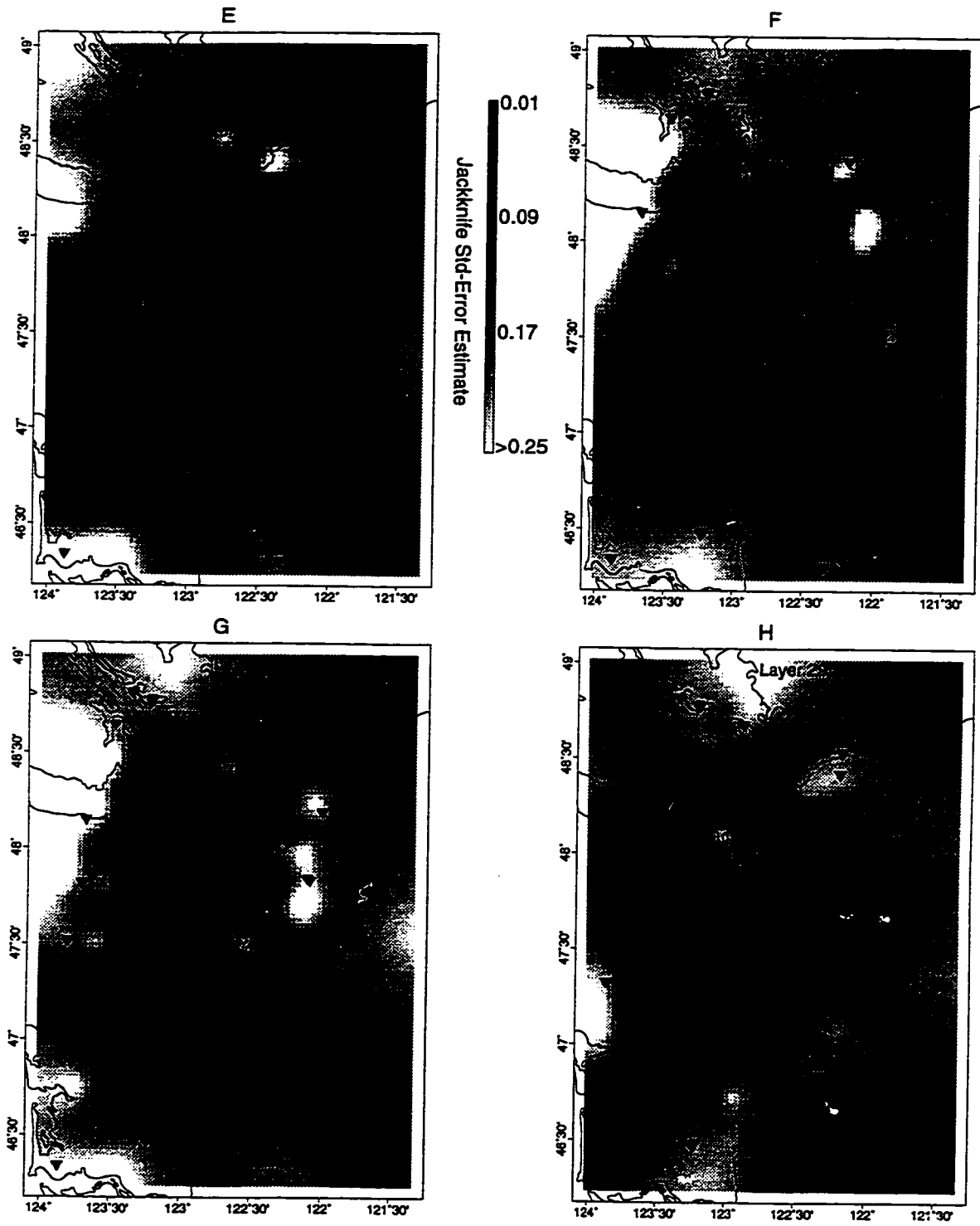


Figure 4.8: (continued)

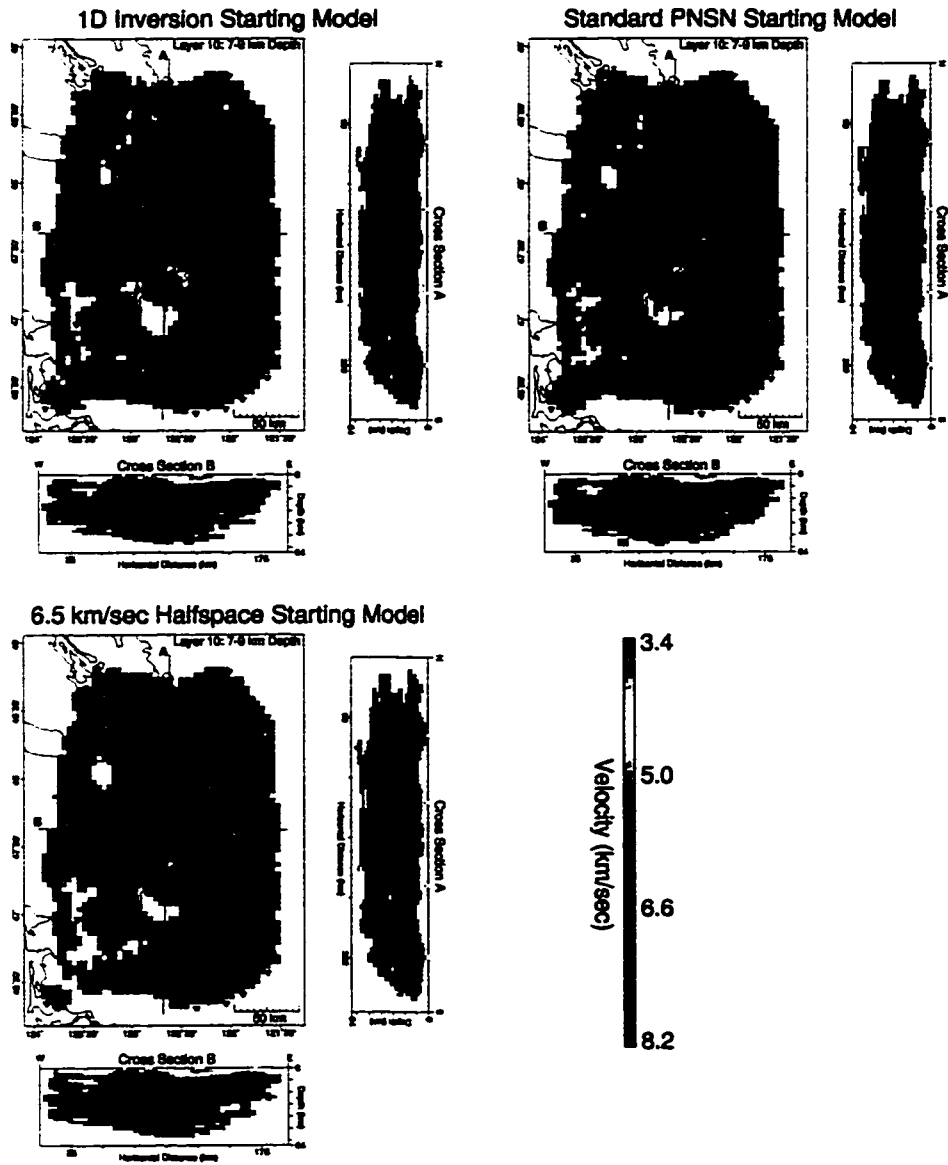


Figure 4.9: Comparison of one layer of and two cross sections for three different starting models.

See text for description of the models used.

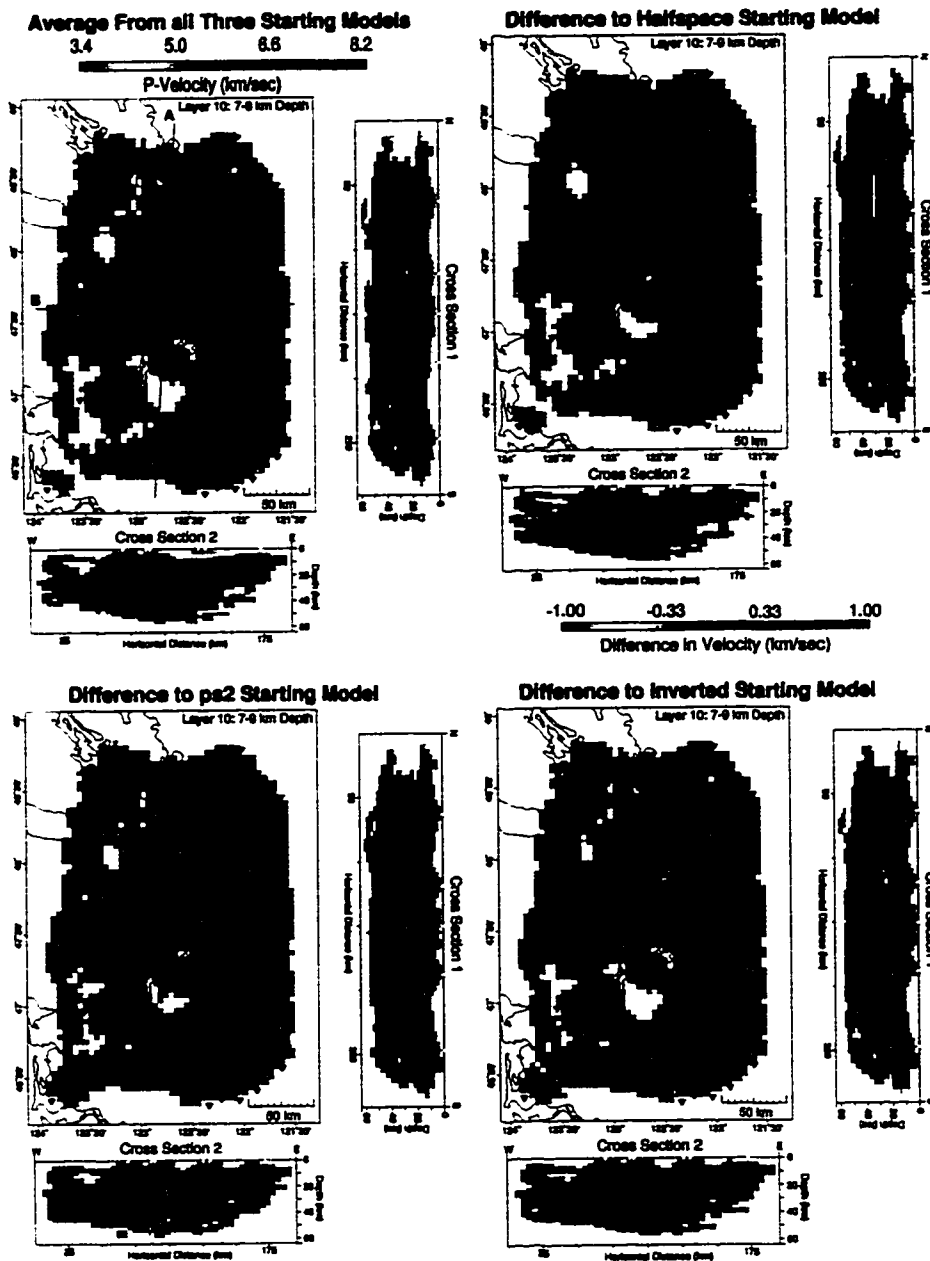


Figure 4.10: (Upper Left) One layer of and two cross sections of the average result from three different starting models.

Other maps and sections show the difference between the average model and the individual results.

See text for description of the models used.

Chapter 5

INTERPRETATION OF RESULTS

In this chapter I will interpret the results of the tomographic inversion in terms of the geologic features that may be represented by the velocity contrasts of the model. The results are shown in map view in figure 4.6. To aid in interpretation several cross sections are shown in figure 5.1. To understand the interpretation it is important to consider the resolution of the model (shown in figures 4.7 and 5.2) and the estimated errors in the velocity model (shown in figure 4.8).

We look at features in the three main geologic provinces within the GPSR; the Coast Range, the Puget Lowland, and the Cascade Range. In addition, I look at one feature deep in the model which I interpret as a mantle wedge above the top of the subducted slab at a depth of about 45 *km*. A far more detailed analysis of the features near the surface is contained in Chapter 7.

5.1 *Coast Range*

5.1.1 *Olympic Core Rocks*

In the far western portion of figure 4.6 A there is a low velocity region. This region is interpreted to correspond to the core rocks of the Olympic Mountains. The core rocks are primarily composed of melange and heavily faulted marine sedimentary rocks [Tabor, 1987] and are expected to have low seismic velocities. At a depth of 5 *km*, the P-wave seismic velocity of the model in this region ranges from $\sim 5.4 - 5.6 \frac{\text{km}}{\text{sec}}$. Table 5.1 is a compilation of some relevant rock velocities from *Christensen and Mooney* [1995]. At this depth we would expect accretionary wedge sediments from the

top of the slab to metamorphose into a metagraywacke facies. The model velocities are a good fit for the laboratory measured velocity of this facies. The region of reduced velocity persists in depth to approximately 25 km where the velocity increases to $\sim 6.3 \frac{km}{sec}$; consistent with rocks of the mica quartz schist facies.

Table 5.1: Summary of Rock Velocities from *Christensen and Mooney* [1995]

Rock Type	Depth (km)	P-Vel. ($\frac{km}{sec}$)	σ^2	%Anisot.	ρ ($\frac{kg}{m^3}$)	σ^2
Basalt	5	5.845	0.547	1.7	2878	144
	10	5.892	0.543	1.6	2883	144
	15	5.915	0.542	1.4	2889	144
	20	5.918	0.541	1.4	2894	144
	25	5.915	0.540	1.3	2899	144
	30	5.908	0.540	1.3	2904	144
	35	5.899	0.539	1.3	2910	144
	40	5.890	0.539	-	2915	144
	45	5.882	0.539	-	2920	144
	50	5.873	0.539	-	2926	144
Metagraywacke	5	5.336	0.615	4.8	2615	112
	10	5.461	0.564	4.5	2621	112
	15	5.536	0.519	4.1	2627	112
Phyllite	20	6.171	0.168	10.3	2745	58
	25	6.165	0.158	9.9	2751	58
Mica Quartz	20	6.340	0.370	13.7	2849	129
Schist	25	6.344	0.375	13.4	2856	129

5.1.2 Crescent Formation

To the east of the low-velocity Olympic Core rocks there is fairly rapid transition into material with a substantially higher velocity (figure 4.6 B and C). This portion of the model is well resolved (figure 4.7) although there is an area with high estimated error (figure 4.8 B). However, the high error is confined to a small portion of the high velocity region and does not affect the interpretation.

The high velocity region corresponds to surficial exposures of the Crescent Basalt, a portion of the Siletzia terrane discussed in Chapter 1. At the surface the Crescent

formation forms a horseshoe shaped contact (the name Crescent formation is due to Lake Crescent on the Olympic Peninsula) with the Quaternary glacial deposits to the east [Schuster, 1992] (figure 5.3). At least the outline of the Crescent Formation horseshoe shape is visible in the model (figure 4.6 A). Although there is some missing continuity, the resolution in this portion of the model is not sufficient to interpret this as breaks in the formation.

The Crescent Formation is a thick basalt unit, mapped in places with a total section thickness estimated to be more than 16 km [Babcock *et al.*, 1992]. The basalt is inter-layered with marine sediments [Tabor and Cady, 1978]. The high velocity region to the east of the Olympic Core falls within the laboratory determined basalt velocities of table 5.1 (5.84 to 5.87 $\frac{km}{sec}$), and the correspondence with basalt velocities persists to a depth of at least 25 km. The Crescent is a thick unit by any measure. Compared with the Babcock *et al.* [1992] estimate our results of 25 km vertical thickness could indicate even greater section thickness, or could represent very steep dip to the mid-crustal depths. On the East-West cross section (figures 5.1 A and B), the contact between the Crescent and the Olympic Core appears to dip to the east at an angle of approximately 45°.

Figure 5.1 also indicates that the western termination of extensive seismicity is coincident with the contact between the Crescent formation and the lower velocity rock of the Olympic Core complex (figure 5.1 B). I propose a simple mechanical model to explain this cutoff in seismicity. Figure 5.4 shows a schematic of the model. The Crescent formation and the Olympic core rocks are two units of different mechanical strength. When the two units are subjected to a north-south compressive stress they must undergo the same strain but they can have different internal stress. Since the Olympic core is the weak unit its deformation is accommodated aseismically. Earthquakes in the GPSR would be expected to occur only in stronger units such as the Crescent formation which deform seismically. However, when the system is subjected to an east-west compressive stress, the two units are under the same stress

but they can undergo different strains. In this case, since the Olympic core is relatively weak, only a small amount of stress is transmitted into the Crescent formation and we see few earthquakes with east-west maximum compression.

5.2 *Puget Lowland*

5.2.1 *Seattle and Tacoma Basins*

The most obvious features in the upper 10 *km* of our model are the two distinct regions of low velocity beneath the cities of Seattle and Tacoma (Figure 4.6). These correspond to basins filled with sediment and expected to have low seismic velocity. In the tomographic model the low velocity due to the Seattle Basin persists to a depth of 11 *km*. Unconsolidated sediments in this area are mapped to a depth of ~ 4000 feet Hall and Othberg [1974] and the reflection model of Pratt *et al.* [1997] shows low velocities and reflections consistent with sedimentary formations persisting to a depth of 6.5 *km*. While I do expect the low velocity to persist for some distance below the base of the sediments, 11 *km* seems extreme. This is probably due to near-surface features being smeared down into the model by almost vertical rays.

In addition to the large low velocity regions near Seattle and Tacoma there is also less clear evidence for low velocity basins near the cities of Everett and Chehalis. These basins are less well resolved than either the Seattle or Tacoma basins. This is a result of two factors: first, these basins are closer to the edges of the model and so there is decreased ray coverage. Second, neither of these areas is as well instrumented as the Seattle-Tacoma region.

According to the Puget Lowland hypothesis of Pratt *et al.* [1997], this entire region is a thrust sheet under a north-south compression. Their model includes basins delimited by east-west striking thrust faults or anticlines. Unfortunately, the resolution of our model is insufficient to define the bounding features of the basins. Since the resolution in the near surface is relatively poor with this dataset, I will

forego an in depth discussion of the Seattle and Tacoma basins until Chapter 7 where I will augment the earthquake data with a large number of surface sources.

5.3 Subducted Slab

At depth, the most prominent feature in the model is a velocity reversal (figure 5.1 A, B, E, and F). At a depth of approximately 35 km the velocity jumps to $\sim 8 \frac{km}{sec}$. However, below this depth there is a reduction in velocity to $\sim 7.6 \frac{km}{sec}$. Although the checkerboard test shows reduced resolution in this portion of the GPSR, the model can detect the sense of large features. Extensive tests with different starting models and data sets have shown this to be a robust feature. I interpret the first transition, to $8 \frac{km}{sec}$ material, as the Moho; then the second transition, to $7.6 \frac{km}{sec}$ material, corresponds to top of the subducted oceanic plate. The result is a wedge of mantle trapped between the bottom of the continental crust and the top of the subducted oceanic plate.

There are then two possible compositional explanations for the low velocity feature. First, work by Kirby *et al.* [1996] suggests that in “hot subduction zones” there is an early transition of basalt to eclogite. At these depths eclogite has a seismic velocity of $7.83 \frac{km}{sec}$; not very different from the mantle. However, this transition releases the water trapped in the oceanic crust, and this water could lead to serpentinization of the mantle above the descending slab. For comparison, the seismic velocity of pure serpentinite at 45 km depth is $5.2 \frac{km}{sec}$. A second, perhaps simpler, possibility is that the oceanic crust at this depth is still basalt. At a depth of 45 km basalt has a seismic velocity of $5.8 \frac{km}{sec}$. Since the resolution at this depth is poor, it is impossible to distinguish between these two possibilities using the results of the tomography experiment.

5.4 Comparison With Previous Studies

In general, the results of this tomographic inversion agree with the results of *Lees and Crosson* [1990] and *Moran et al.* [1996]. Specifically, the model of *Lees and Crosson* [1990] contained low velocity features in the region of the Olympics and the basins under Seattle and Tacoma. Poorly resolved features on the edge of my model such as the low velocity under Mount Rainier at a depth of 15-17 *km* (figure 4.6 C) were interpreted structurally by *Moran et al.* [1996]. The model of *Moran et al.* [1996] included low velocity regions under Seattle and Tacoma similar to this model.

Figure 5.1 C shows a cross section close to the 2-D refraction profile of *Parsons et al.* [1998]. Although the resolution of my model is not sufficient to recover the detailed near shore structure seen in *Parsons et al.* [1998], the two models both include a mantle wedge that terminates along a north-south line approximately along the center of the Puget Sound.

5.5 Hypocenter Relocations

Figure 5.5 shows a comparison of the hypocenters of the CDS using the ps2 velocity model (with station corrections) and the 3-D model resulting from this study. As described in section 4.3, the average RMS for the data set is substantially lower with the 3-D model. The earthquakes tend to be 2-5 *km* shallower with the 3-D model while the horizontal locations do not change much. There are a limited number of events with depths that change by ~ 10 *km* and one event with a hypocenter that changes by over 50 *km* horizontally. This is obviously a poorly located event that has a very poorly constrained location in spite of the efforts to remove such events from the dataset (this event did not make it into the HQDS). The changes do tend to be larger in the areas where a poor depth constraint might be expected (*e.g.* deep slab events), and lower in the vicinity of concentrations of seismographs (*e.g.* near Mount Rainier and Mount Saint Helens).

5.6 Summary

Interpretation of the inverted model of the P-wave seismic velocity delineates major features such as: the Core Rocks of the Olympic Mountains; the Siletzia terrane; basins filled with low velocity sediments under the cities of Seattle, Tacoma, Everett, and Olympia; and a mantle wedge at a depth between 40 and 50 *km* under Seattle. After this inversion was complete additional data became available which allowed the inversion of a model with much higher resolution in the Central Puget Lowland and this is the subject of the balance of this dissertation.

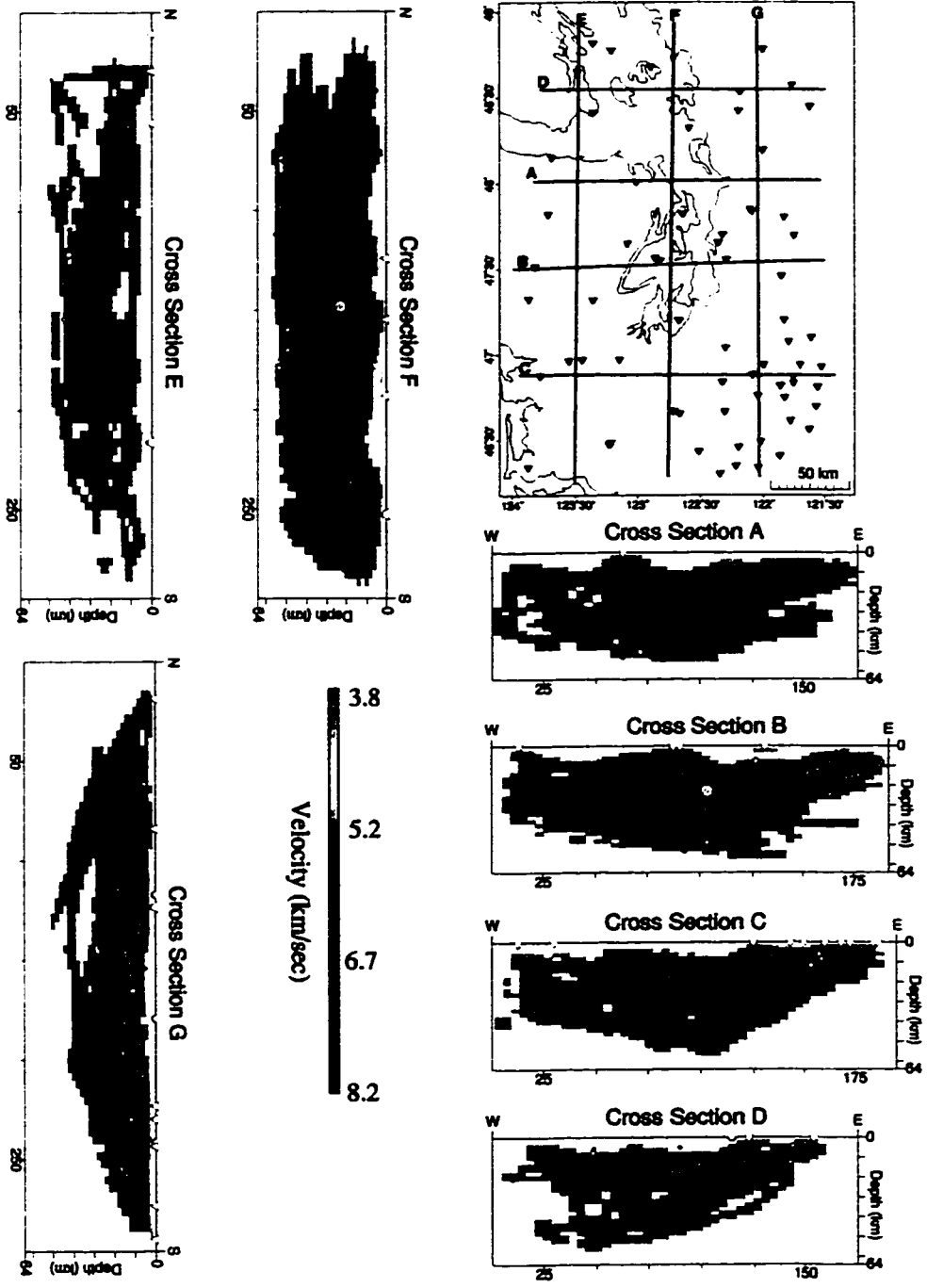


Figure 5.1: A Set of cross sections through the final model and a map of their locations.

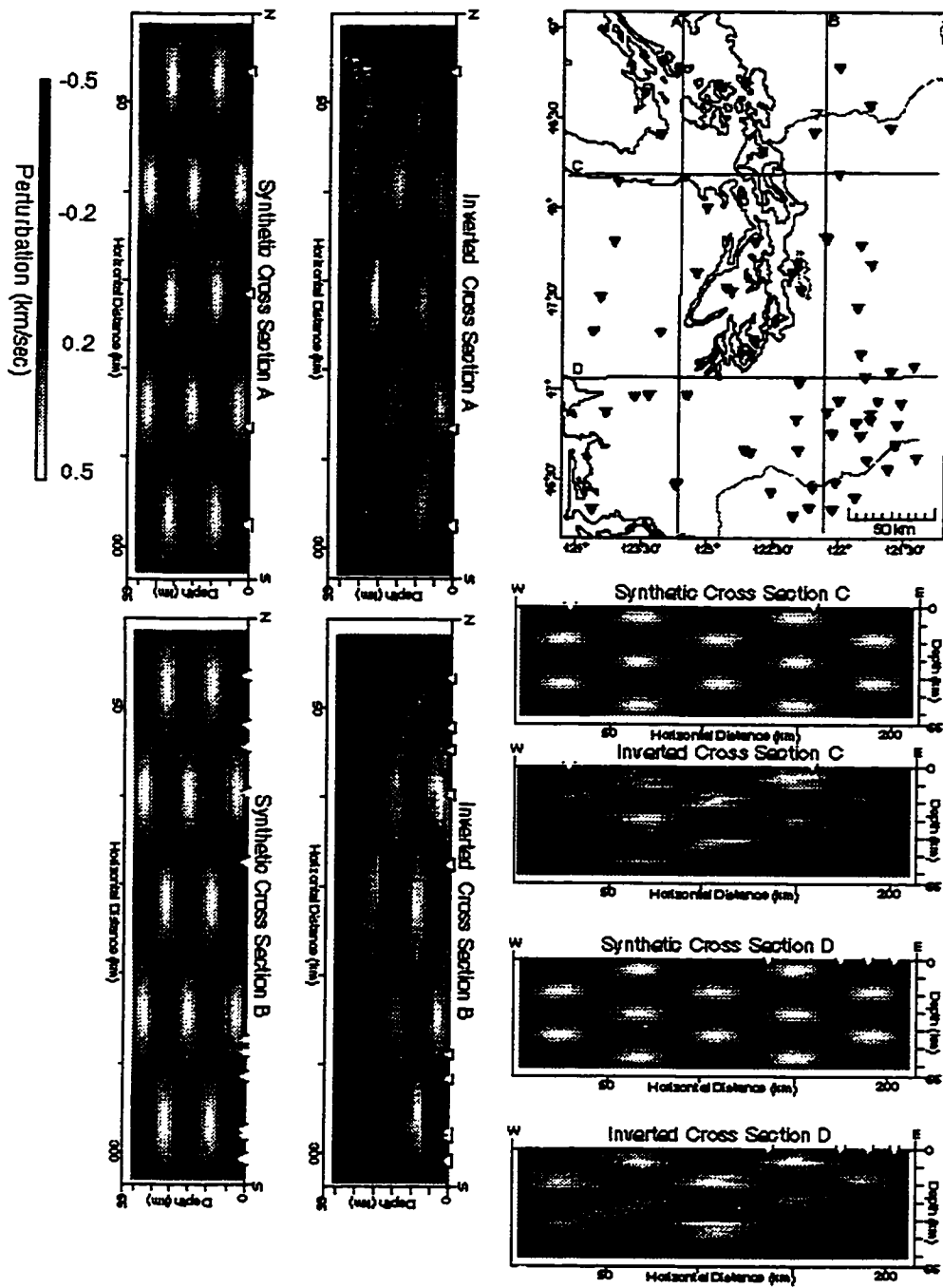


Figure 5.2: A Set of cross sections through a checkerboard test from the final model and a map of their locations.

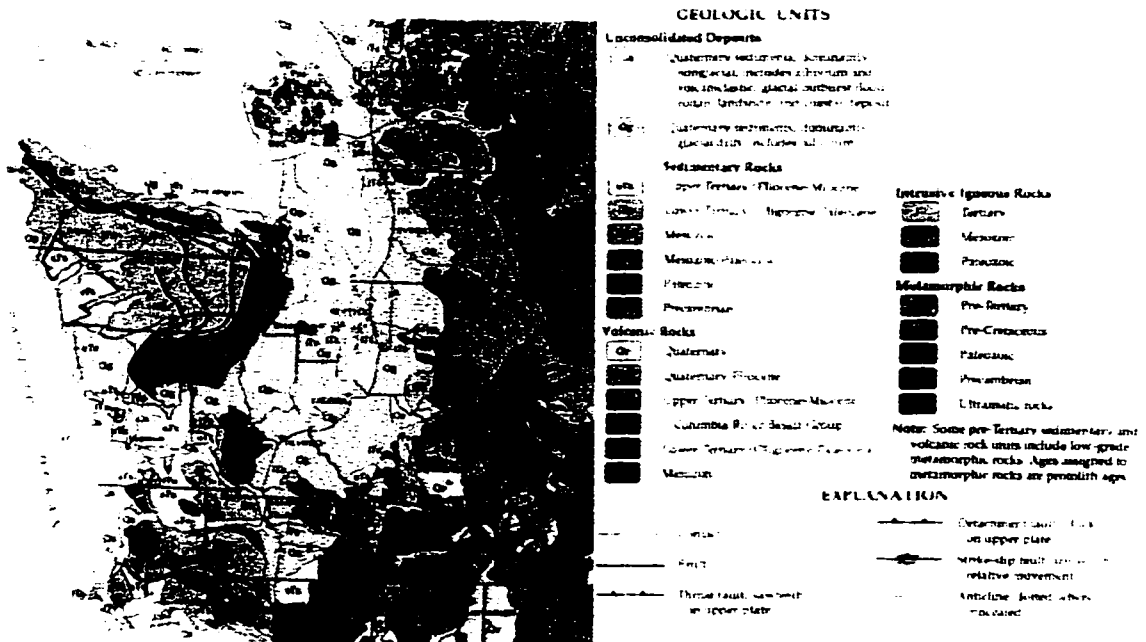


Figure 5.3: Map, modified from *Schuster* [1992], showing the geology of the GPSR.

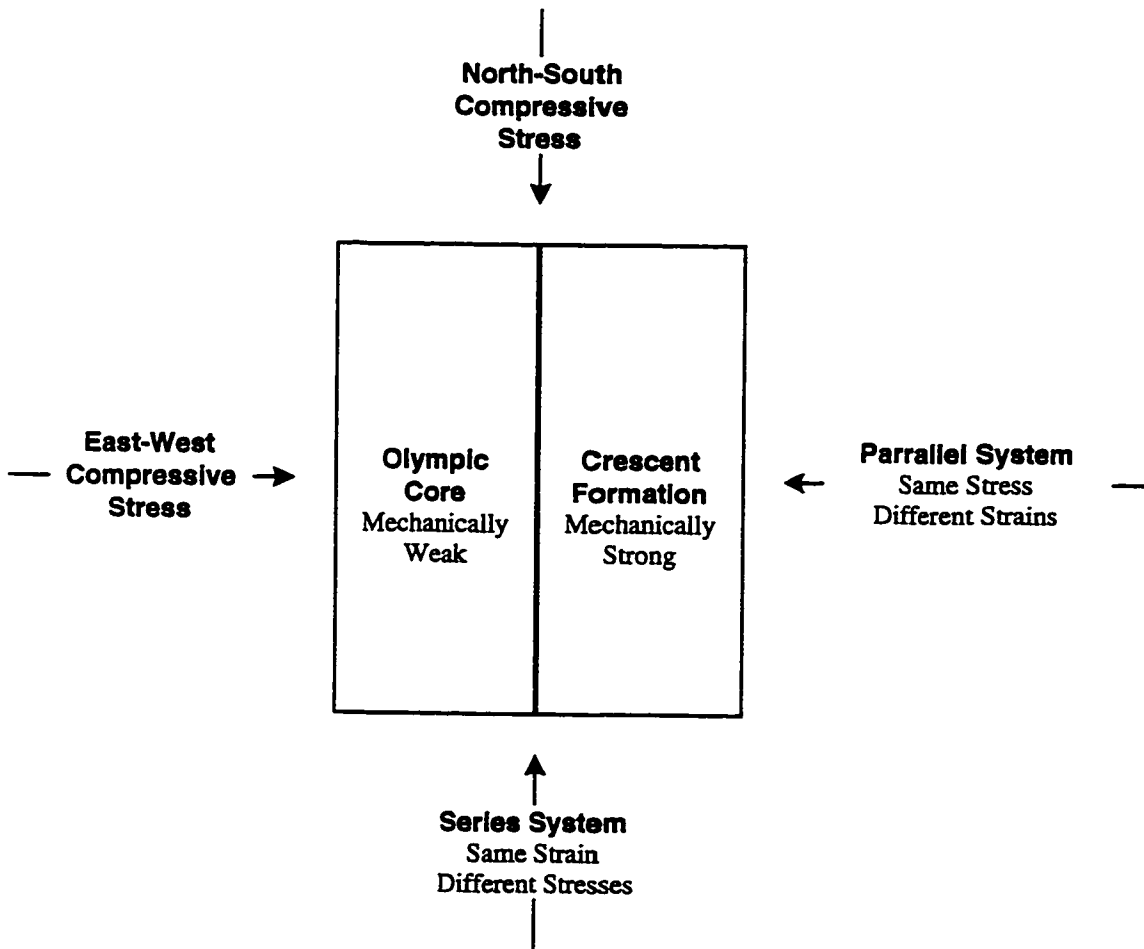


Figure 5.4: Vastly simplified model of the Olympic Mountains Crescent formation mechanical system.

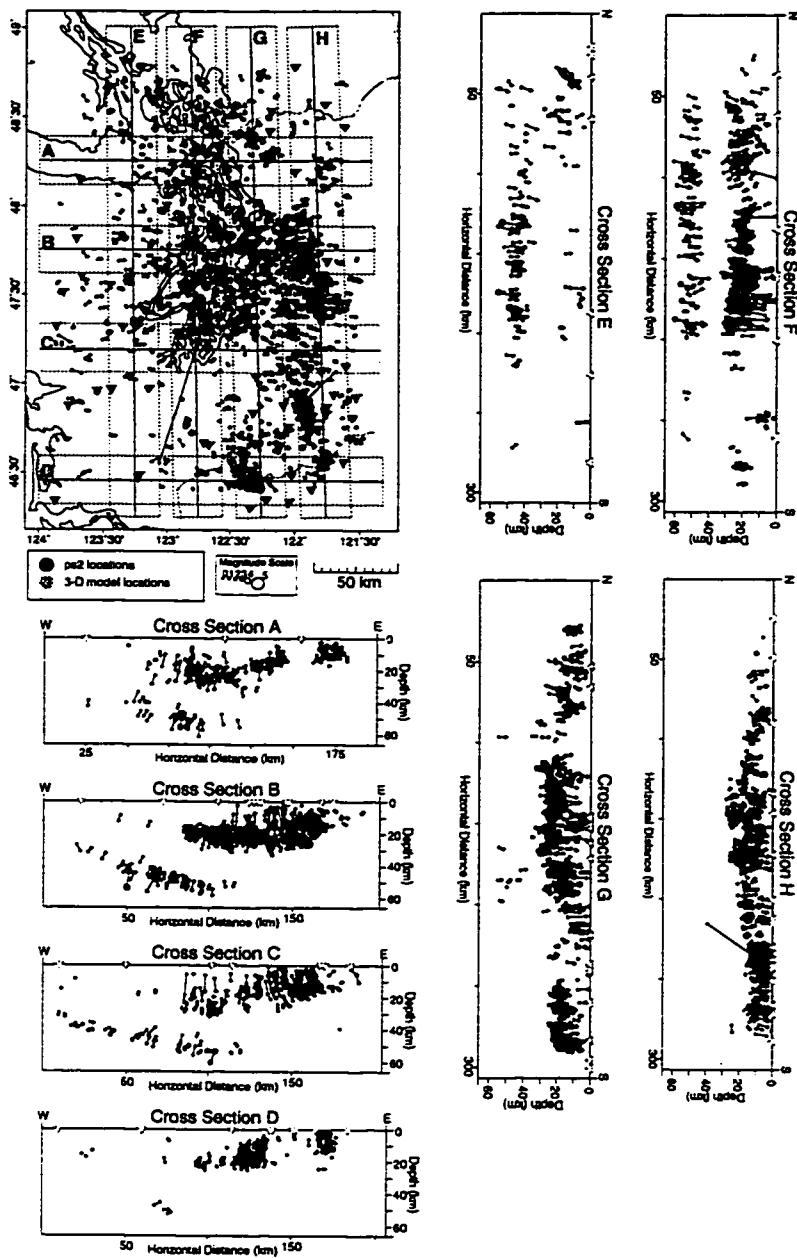


Figure 5.5: Comparison of the location of the earthquakes of the CDS located with the ps2 velocity model (with station delays) and with the 3-D model resulting from this study. Vectors are shown connecting the earthquake pairs from the locations with the different models.

Chapter 6

ADDITIONAL DATA FROM THE SHIPS EXPERIMENT

As a result of concern about a large, damaging earthquake in the Seattle Metropolitan area the US Geological Survey (USGS) instigated the “Seismic Hazards in the Puget Sound” (SHIPS) project. A portion of the work for SHIPS is being performed by a number of collaborating institutions including the University of Oregon (U of O), the Geological Survey of Canada (GSC), and the University of Washington (UW). SHIPS is an active experiment consisting of a marine phase performed from March 10 to March 24, 1998, and a land phase currently scheduled for the spring of 1999.

6.1 Marine Phase of SHIPS

During the marine phase the UW Research Vessel *Thomas Thompson*, was outfitted with an array of 17 airguns with a total volume of 6500 in^3 (figure 6.1). The *Thompson* towed a 4 km streamer for recording short offset reflections and the Canadian Research Vessel *Tully* was employed for long offset reflections. In addition, approximately 240 land-based seismometers were deployed for the period that the *Thompson* was active; 60 by the UW, 20 by the U of O, 30 by the GSC, and the remainder by the USGS (figure 6.2). These stations were concentrated along the waterways, but a substantial number were scattered in a 2-D array across the Puget Sound region. The *Thompson* spent several hours performing a “shakedown cruise” in Lake Washington and the rest of the experiment in the waterways of the Puget Sound (figure 6.2). When the streamer was not deployed, the *Thompson* fired all guns at 40 s intervals. Because of space considerations when the streamer was deployed, 3 of the largest

guns were inactive and the cycle time was reduced to 20 s.

6.2 Data

At this time, the data from the temporary seismographs deployed for the SHIPS experiment are not yet available. However, the shots were also recorded at the permanent seismograph stations of the PNSN, and this data was available immediately, even before the experiment was completed. For the duration of the SHIPS experiment 33 PNSN stations in the immediate Puget Sound region were set to record continuously (in addition to the normal triggered mode). The continuous data was stored in 15 *minute* chunks in the standard UW2 data format.

6.3 Stacking

6.3.1 Motivation

Certain source receiver pairs had excellent signal-to-noise ratios and provided unambiguous first arrivals (figure 6.3). Analysis of these shots using the coda magnitude relationship developed for the PNSN indicates that the individual shots had a magnitude equivalent to approximately a 0 M_c earthquake. Because this is a relatively small signal for an urban and seismically noisy environment, the signal at the majority of stations was less clear. In order to enhance the signal-to-noise ratio at these stations I developed a stacking technique. The stacking is motivated by the underlying idea that the signal (the arrival of energy from the *Thompson's* airguns) is coherent with a 40 s period, whereas the noise that is obscuring the signal can be modeled as a random process.

6.3.2 Synthetic Example

Figure 6.4 illustrates this process. An impulsive oscillatory waveform (figure 6.4 A) was assumed with a period of 40 s and random amplitude (Gaussian distributed with

a mean 1 and a variance of 0.2). We then add zero mean Gaussian noise with a variance of 1 to obscure the signal. In an individual 40 s window (figure 6.4 B) the signal is difficult or impossible to pick. However, when we sum 84 of the windows (equivalent to 1 *hour* of data), the signal adds coherently and the noise cancels out (figure 6.4 C). In fact, with random Gaussian distributed noise such as this with variance σ^2 and mean μ , the expected value of the average of n points is

$$p_e = \mu \pm \frac{\sigma^2}{\sqrt{n}} \quad (6.1)$$

As expected, the improvement of the signal in this example fits this relationship. If we compare figure 6.4 B and figure 6.4 C, the average value noise in the stack of 84 traces is slightly over 10% of the noise in the un-stacked traces.

6.3.3 Arrival-Time Move-out

The primary complication in the stacking process comes from the movement of the source (the airgun array towed by the *Thomas Thompson*) during a single stack. In order to contain approximately 100 *shots* (needed to reduce the noise level to 10% of the unstacked level) each stack needs to be 1 *hour* long. During 1 *hour* the ship may move up to 8 *km*. This causes an apparent change in the 40 s periodicity of the data due to variation in the propagation distance and structure. If we stack blindly without correcting for the source movement the signal loses coherency and is not well recovered. Figure 6.5 is a demonstration of this effect. In this example, the signal is obvious in the individual traces displayed in the record section. However, the signals do not align because of the movement of the source, and the stacked signal is unclear.

In order to correct this problem, we use a slant stacking process. We define the stack location as the position of the middle shot going into the stack (figure 6.6). Instead of adding the windows directly, we first calculate a time offset from the stack location to the shot location. To determine the offset, travel-times are calculated with the finite-difference travel-time (FDTT) calculator using a reasonable 3-D velocity

model. Then the offset is just the difference in travel-time between the stack location and the shot location. Figure 6.6 shows the calculated travel-times across a real stack; this stack-station combination was chosen because it has a large offset (the source movement is nearly perpendicular to the gradient of the travel-time).

Of course the 3-D model does not exactly represent the earth. However, the difference between the 3-D model and the true earth is reflected in the difference between the predicted travel-time and the true travel-time. This is exactly the information we need in order solve the tomography problem. It is the first derivative of this difference across the range of shots in an individual stack that causes mis-alignment of the stack. It is reasonable to expect that this first derivative is small across a distance on the order of 8 km. Figure 6.7 shows realignment based on the 3-D model from Chapter 4. There is a slight mis-alignment due to the inaccurate velocity model (visible near the top of the record section). However, the main energy arrival in the stack corresponds to the arrivals at the center of the record section, which is the projected location of this stack.

Filtering

There are two other important effects due to the motion of the source. First, there is a loss of coherency in the waveform at the station. Recent work by *Bear and Paulis* [1997] indicates that high frequency seismic signals can lose coherency across distance ranges on the order of 150 m. Although the work of *Bear and Paulis* [1997] looked at loss of coherency as the receiver location changed, it seems reasonable to expect a similar result as the source moves. For this reason, it is desirable for the signals to be low-pass filtered so that the long wavelength portion of the signal, less sensitive to small scale (~ 100 m) velocity variations, is all that remains. The signal spectrum shows a peak between 2 and 15 Hz (figure 6.8). Since we want the low-period portion of this signal we choose to use a zero-phase bandpass filter with corners at 2 and 10 Hz on the signals before stacking. Figure 6.9 shows a comparison of the same

signal stacked with a various number of shots both with and without filtering. This signal was chosen because it is strong enough to be successfully stacked even without filtering to explore the effect of filtering on the quality of the arrival. Although the loss of high frequency energy in the filtered trace makes arrival-time picks less precise, the mean absolute time of picks on the filtered and un-filtered traces is the same.

6.3.4 Water Depth Correction

The next problem that needs to be addressed, with respect to the movement of the ship, is the change in the water depth beneath the shots making up a stack. Since the acoustic velocity of water is low ($\sim 1.5 \frac{km}{sec}$) this could cause an error in the absolute arrival time as well as causing mis-alignment in the stack. We account for this by projecting the source down to the water-bedrock interface and adjusting the time using an assumed water velocity of $1.5 \frac{km}{sec}$. The true path of the energy from the shot actually follows a slanted path toward the station (figure 6.10); but since the velocity increases rapidly in the bedrock, a projection straight down is a reasonable approximation. The real angle taken by the signal through the water will be the furthest from vertical with shots that are close to stations. In general, this is where the water is shallow.

In fact, we can make a few assumptions and calculate the error in the shot location due to the vertical shot projection for both a near and a distant station. The ray-parameter, p , for a P-wave ray is defined by

$$p = \frac{\sin(\theta)}{v_P} \quad (6.2)$$

where θ is the angle the ray makes to vertical and v_P is the P-wave velocity where the ray angle is measured. At the bottom of the ray-path, the turning point, θ is 90° so p for any ray is $\frac{1}{v_P} \Big|_{Turning\ Point}$. As a general rule of thumb, the turning point for a ray with a surface source and receiver is 10% of the source-receiver distance. So, a 100 km ray turns at ~ 10 km. Using the inverted 1-D velocity model for the GPSR

(table 4.1) this corresponds to a ray parameter of $\frac{1}{6.59}$ or $0.1517 \frac{\text{sec}}{\text{km}}$. In the water, where the velocity is $1.5 \frac{\text{km}}{\text{sec}}$, this ray would make an angle of $\sin^{-1}(1.5p) = 13^\circ$ from vertical. The deepest stack was in 220 m (table 6.1 day 071, hour 12) of water, so a 13° angle produces a negligible location error of 51 m. A ray with a 10 km source-receiver distance has a ray-parameter of $0.17 \frac{\text{sec}}{\text{km}}$ corresponding to an angle, in the water, of 14° . Even in 220 m of water this causes a location error of only 58 m.

6.4 Sample Stack

A sample of the results is shown in figure 6.11, they vary from very clear at Oak Harbor (OHW) and on all three components at Mt. Erie (ERW), to difficult-to-see but detectable due to a change in frequency content at Jim Creek (JCW), to undetectable at Gold Mountain (GMW) where there are some high points around the predicted arrival but nothing unambiguous enough for a pick.

From all of the stacks performed, I have selected the best from the 20th hour (GMT) of Julian day 069; (figure 6.13) and the worst from the 5th hour of Julian day 071 (figure 6.14) to display here in a record section format. In the best example there are 21 clear arrivals, in the worst example there are only 7.

6.5 Selection of Data to Stack

Since there is a large amount of data from the SHIPS experiment, and it is impractical to analyze it all at this time, I selected a subset of the available data. I selected 56 hour-long periods chosen to give good coverage of the central Puget Sound region (figure 6.12). From these stacks I was able to pick a total of 862 P-wave arrivals. This is an average of $15.4 \frac{\text{picks}}{\text{stack}}$.

Table 6.1 shows a summary of the results of the stacking. "WD" is the water depth under at the stack. "Dt" is the distance from the stack location to the most distant shot, this is as high as 4.6 km since the stack is not always at the exact center

of the shots. “Num” is the number of picks for the stack, “Res” is the maximum absolute residual for picks made on the stack. And “Off” is the distance from the stack to the most distant station on which a pick was made.

Table 6.1: Summary of SHIPS stacks

<i>Stack Location</i>						<i>Picks</i>		
Day	Hour	Lat (°)	Lon (°)	WD (km)	Dt (km)	Num	Res (s)	Off (km)
069	20	47.740	-122.270	0.020	3.36	21	3.3	119.4
069	21	47.683	-122.231	0.040	3.93	19	3.1	125.0
070	10	47.686	-122.482	0.160	3.61	12	2.2	70.3
070	12	47.537	-122.470	0.070	4.54	15	2.2	130.0
070	13	47.466	-122.518	0.110	4.44	13	0.3	137.0
070	14	47.397	-122.539	0.130	4.03	16	1.6	161.5
070	15	47.331	-122.552	0.100	2.25	17	1.7	151.5
070	19	47.325	-122.711	0.070	3.56	12	1.5	173.2
070	20	47.260	-122.695	0.080	4.06	11	1.9	119.0
070	23	47.148	-122.762	0.070	4.21	15	1.4	193.1
071	02	47.258	-122.853	0.040	4.47	12	2.2	134.2
071	03	47.184	-122.803	0.050	4.62	14	1.5	141.9
071	04	47.120	-122.725	0.070	4.72	19	1.4	152.0
071	05	47.132	-122.673	0.120	1.19	7	1.7	149.6
071	06	47.203	-122.596	0.180	2.14	11	1.8	165.3
071	07	47.253	-122.565	0.080	3.71	18	1.5	160.0
071	09	47.305	-122.498	0.070	3.96	17	2.1	170.5
071	10	47.297	-122.451	0.140	3.32	14	1.2	170.5
071	11	47.350	-122.388	0.080	4.25	14	0.4	151.6
071	12	47.411	-122.360	0.190	4.16	19	2.2	145.5
071	13	47.484	-122.403	0.220	4.56	14	1.0	109.2
071	14	47.564	-122.431	0.210	4.85	13	1.2	111.5
071	15	47.606	-122.358	0.170	4.02	19	2.0	135.4
071	16	47.651	-122.444	0.100	4.04	18	2.0	132.5
071	17	47.729	-122.433	0.170	4.61	14	2.2	123.9
071	18	47.808	-122.411	0.190	4.37	13	2.2	128.4
071	20	47.942	-122.322	0.200	4.46	17	2.3	134.8
071	21	48.005	-122.277	0.150	3.74	21	3.1	144.0

continued from previous page

Day	Hour	Lat (°)	Lon (°)	WD (km)	Dt (km)	Num	Res (s)	Off (km)
071	22	48.067	-122.327	0.100	3.94	20	1.5	151.6
072	02	48.068	-122.419	0.180	3.89	19	2.0	133.2
072	04	48.163	-122.547	0.100	3.53	13	0.8	96.0
072	15	47.877	-122.459	0.190	4.34	16	1.2	122.3
072	16	47.948	-122.522	0.160	5.07	11	1.4	84.6
072	20	47.776	-122.729	0.050	3.47	13	0.7	122.9
073	02	47.493	-123.050	0.160	3.93	16	1.0	125.3
073	03	47.431	-123.108	0.160	4.18	14	2.2	124.3
073	04	47.373	-123.123	0.120	4.00	8	2.0	128.2
073	05	47.448	-123.096	0.120	4.43	19	2.1	130.9
073	07	47.583	-122.984	0.160	4.46	21	1.0	128.5
073	08	47.635	-122.915	0.110	3.65	21	2.6	129.3
073	09	47.667	-122.832	0.140	3.71	17	2.2	112.7
073	10	47.705	-122.760	0.140	3.80	16	1.4	136.0
073	12	47.827	-122.667	0.050	3.60	11	0.5	95.6
073	14	47.945	-122.637	0.090	4.14	14	1.6	146.9
073	15	48.026	-122.626	0.080	4.87	15	1.7	154.8
073	16	48.118	-122.653	0.160	6.01	17	0.9	164.9
073	17	48.196	-122.783	0.060	6.54	14	1.8	126.3
073	18	48.254	-122.888	0.070	5.03	15	1.3	142.8
073	19	48.309	-122.950	0.140	4.08	16	3.1	129.1
075	04	48.198	-123.113	0.150	3.94	16	1.7	177.0
075	05	48.164	-123.042	0.050	4.00	15	1.0	182.7
075	07	48.107	-122.956	0.070	6.29	19	1.8	174.0
075	07	48.113	-122.911	0.070	3.41	19	1.8	172.9
075	08	48.155	-122.841	0.090	3.71	16	0.9	174.7
075	10	48.284	-122.779	0.070	4.00	12	1.0	148.2
075	11	48.352	-122.748	0.060	4.03	13	1.3	191.7

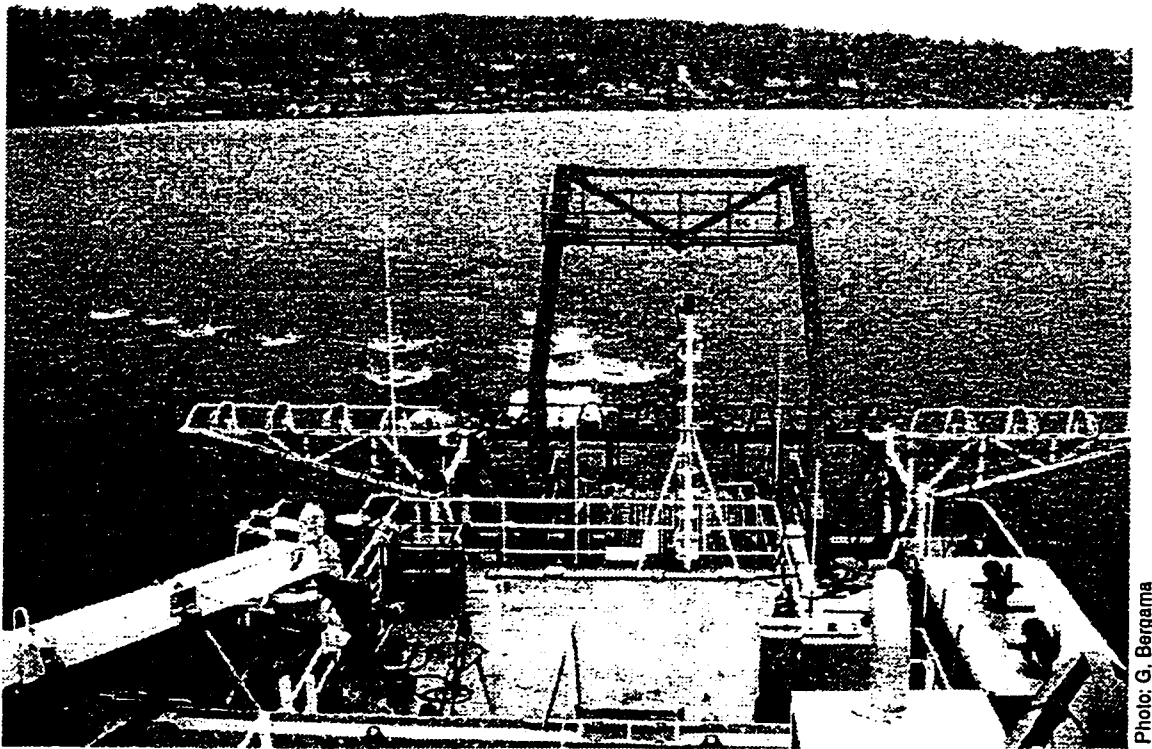


Photo: G. Bergama

Figure 6.1: View off the fan-tail of the University of Washington Oceanographic vessel Thomas Thompson. All guns (suspended beneath the floats) have just fired but the bubbles are only visible from the two in the center. The Laurelhurst neighborhood of Seattle is in the background.

Thompson Track Map

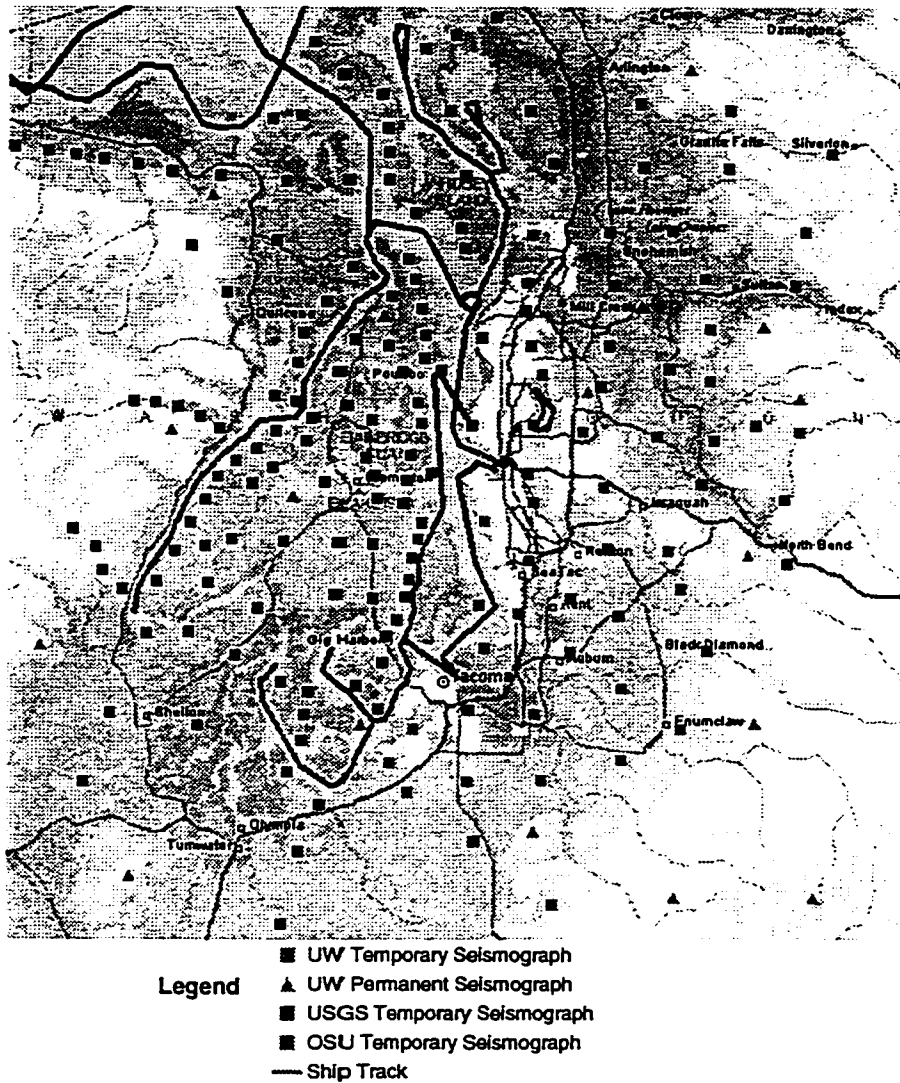


Figure 6.2: Map showing the path of the RV Thomas Thompson during the SHIPS experiment. This figure also shows the locations of temporary and permanent seismographs in operation during the experiment.

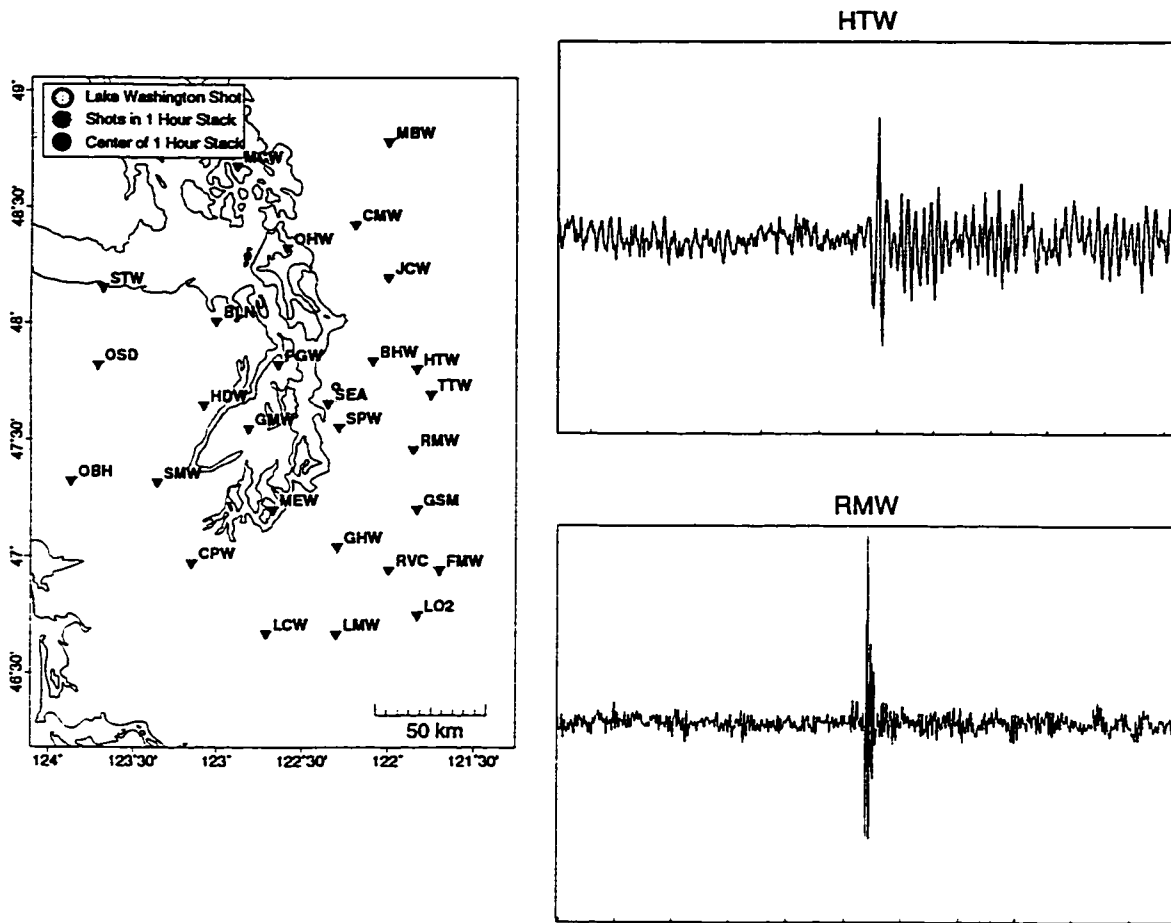
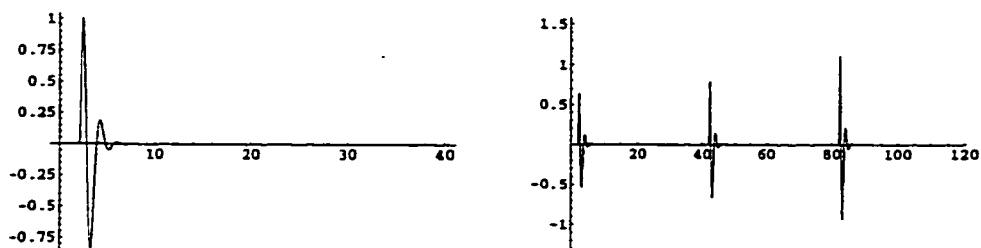


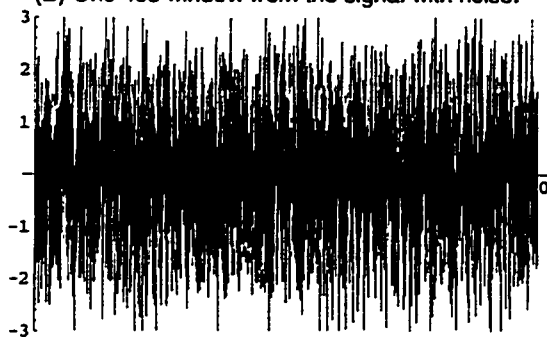
Figure 6.3: Figure showing two good examples of energy (unstacked) from the airguns of the RV Thomas Thompson arriving at permanent seismographs of the PNSN. These examples are from a shot in Lake Washington during the first active day of the experiment (black circle with grey fill in the map).

Synthetic Stack Example

(A) Synthetic signal with 40s period; left side, one cycle with unit amplitude; right side, 3 cycles with random amplitude (Gaussian with unit mean and 0.2 variance).



(B) One 40s window from the signal with noise.



(C) A stack of 84 (1 hours worth of data) 40s windows. The noise in the stacked signal is approximately 10% of the noise in the unstacked signal.



Figure 6.4: Examples of synthetic stacking.

Example Straight Stack

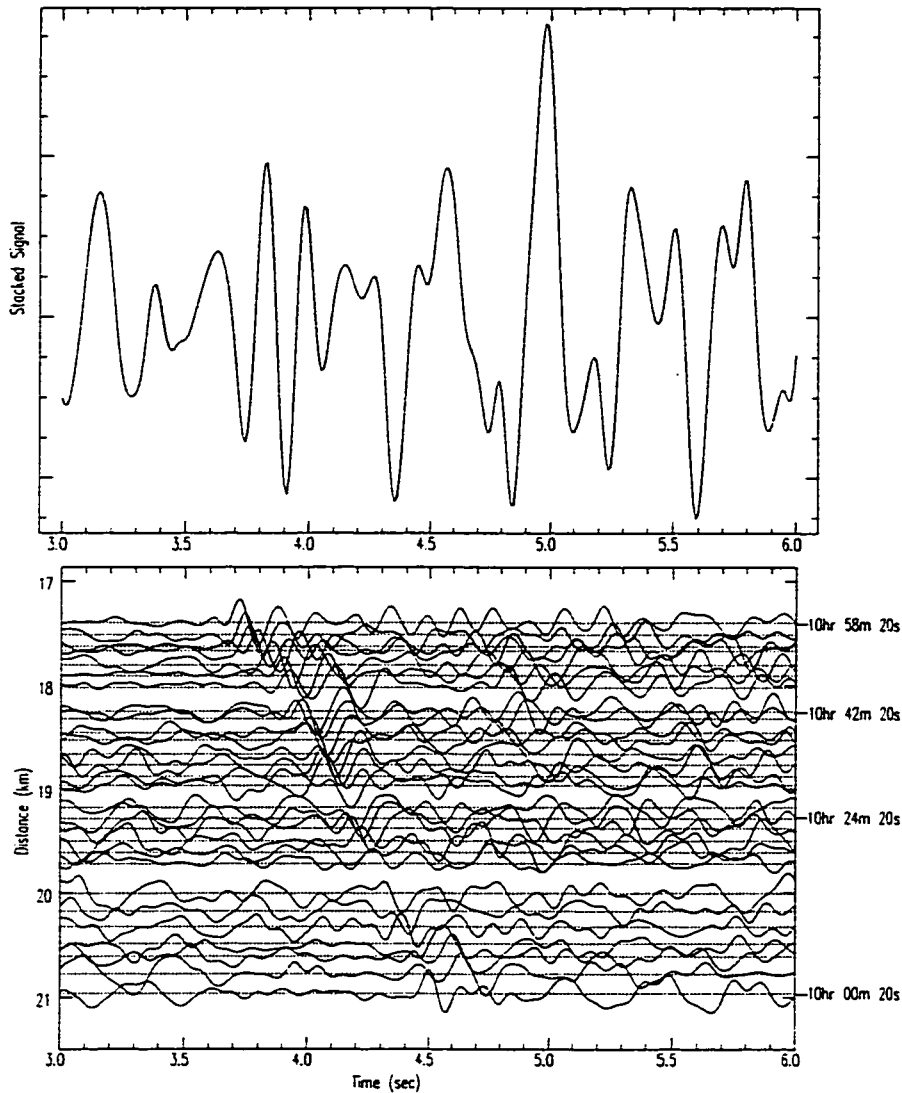
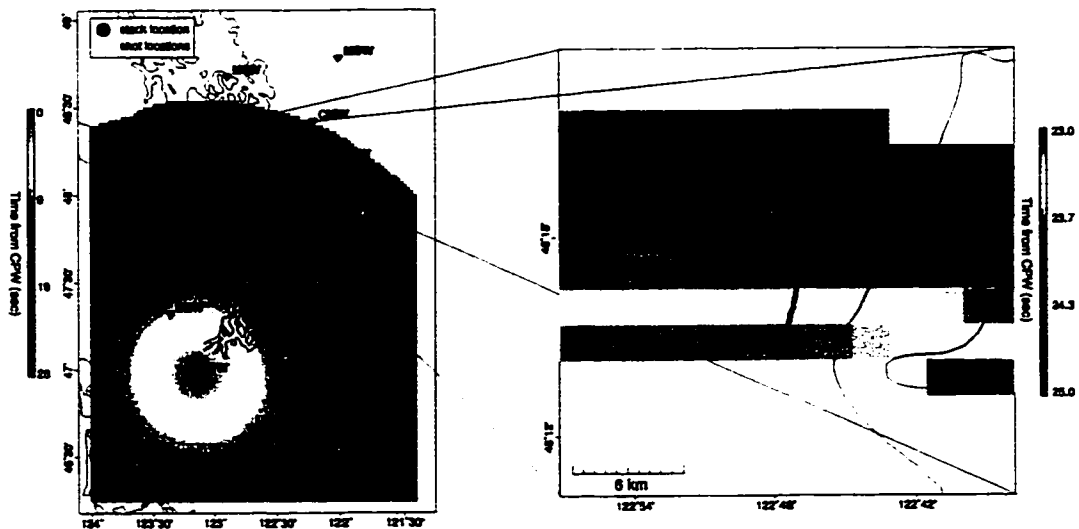


Figure 6.5: Example from Oak Harbor (OHW). On the bottom we show a record section of shots in 1 hours worth of data (to reduce clutter only $\frac{1}{3}$ of the shots are actually shown). At the top we show the stack resulting from these shots. Because the source is moving the shots do not add coherently and we get a low quality result. The location of the shots making up this stack is shown in Figure 6.3.



Map of shots and stack location for the 10th hour of March 16 (Universal Time). Color shows the time calculated from station CPW. Right is the whole region, left is blow up in the region of the stack showing the time offset during this stack. This stack is 8 km long and the total time offset across is approximately 1.2s.

Figure 6.6: This figure shows the time offset across a single stack. The travel-times were calculated using the 3-D velocity model of *Symons and Crosson* [1997] and the finite-difference travel-time calculator. Times are calculated outward from Capitol Peak (CPW), total offset across the stack is approximately 1.2 s.

Example Slant Stack

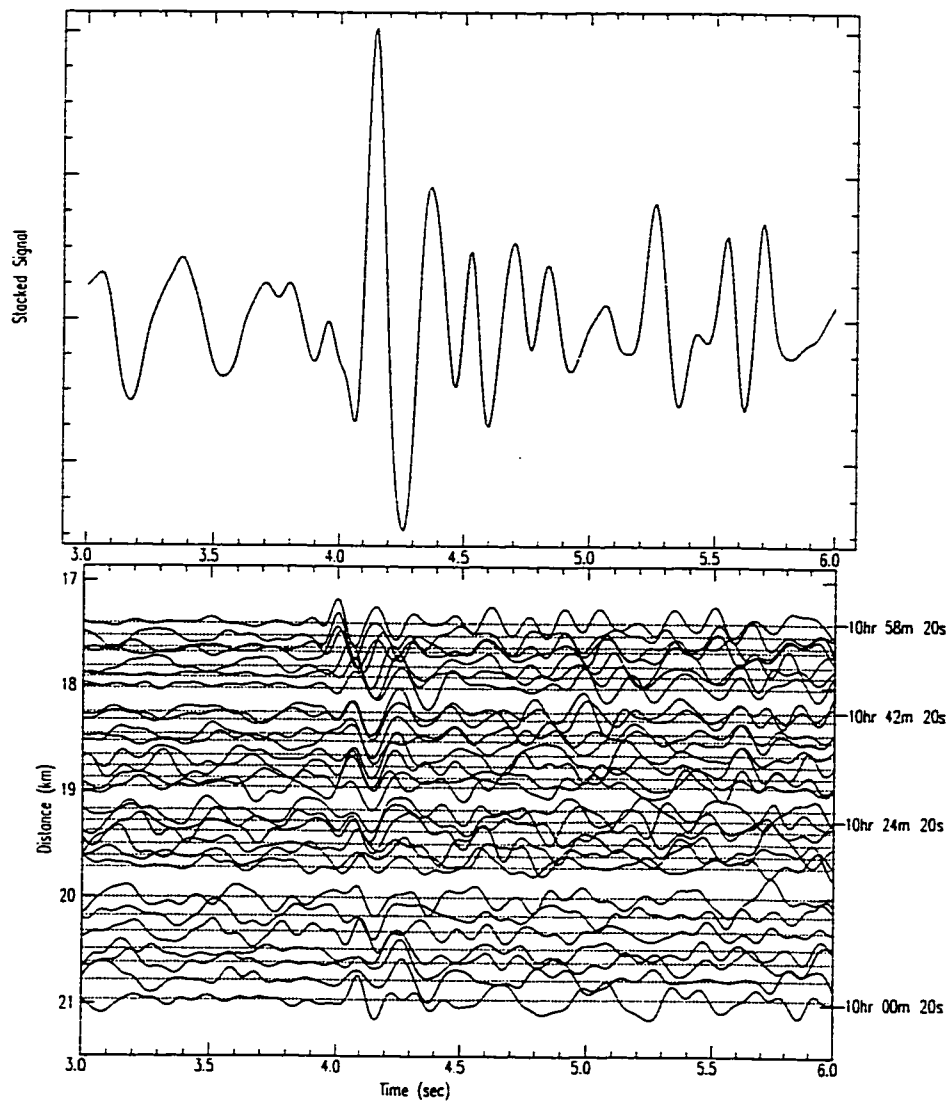


Figure 6.7: Example from Oak Harbor (OHW). This is the same as Figure 6.5 except we have corrected for source movement. The shots do not exactly align as a result of the imperfect model, but the stack is of high quality. The stack location would be at the center of the record section. The main arrival on the stack is coincident with the arrivals at the center of the section.

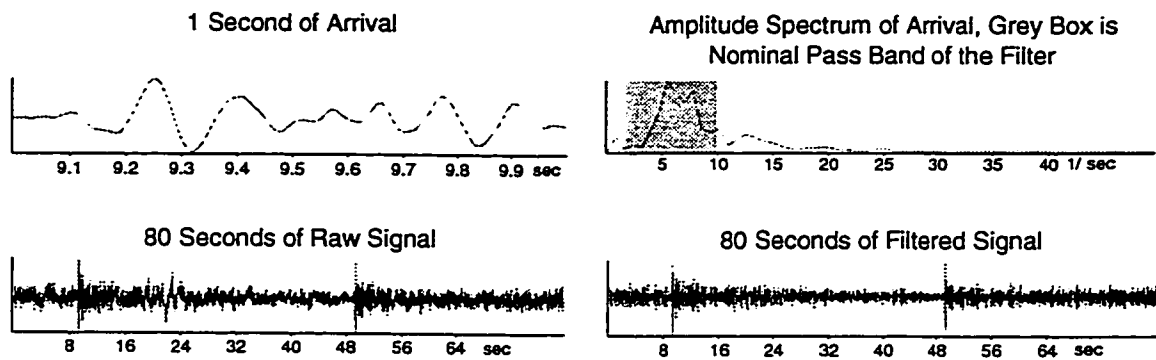


Figure 6.8: (Top) Time series and Fourier Power Spectrum of 1 s of arrival at Haystack Mountain (HTW), this is one of the good arrivals from Figure 6.3. (Bottom) 80 s of signal before and after filtering.

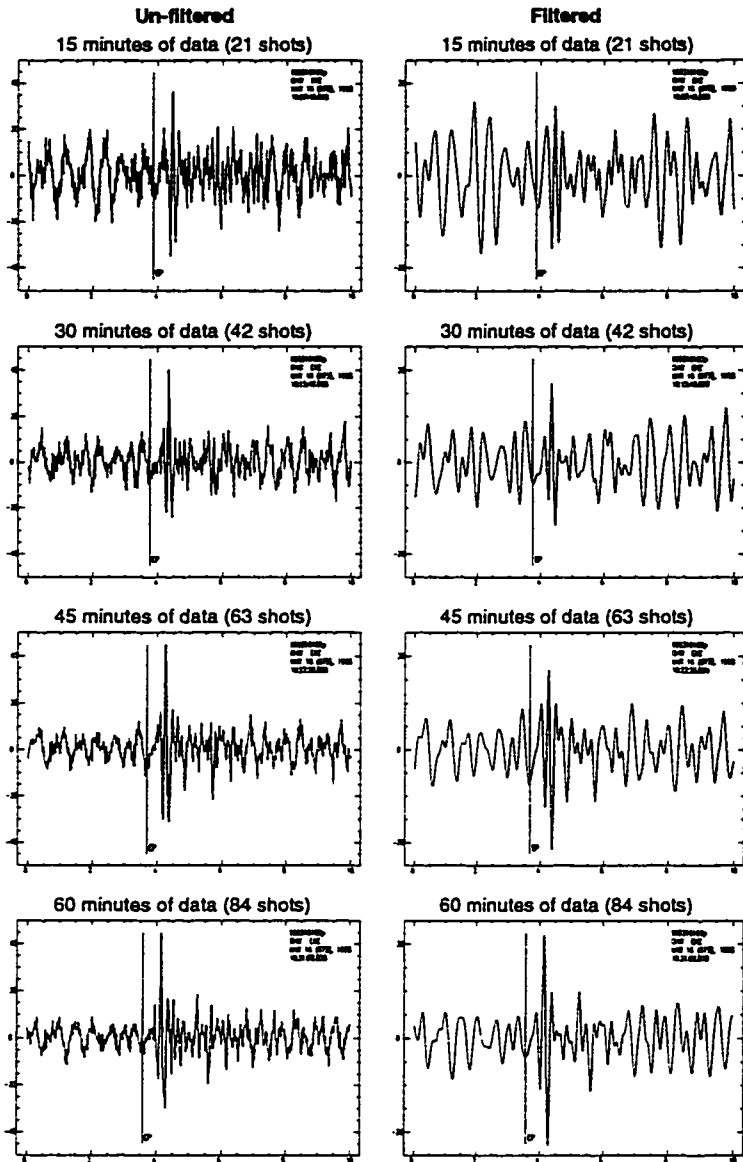


Figure 6.9: Figure showing a comparison of stacking with and without filtering at a station with a strong arrival. In both the filtered and un-filtered data the shape of the waveform is maintained without regard to the number of shots included in the stack.

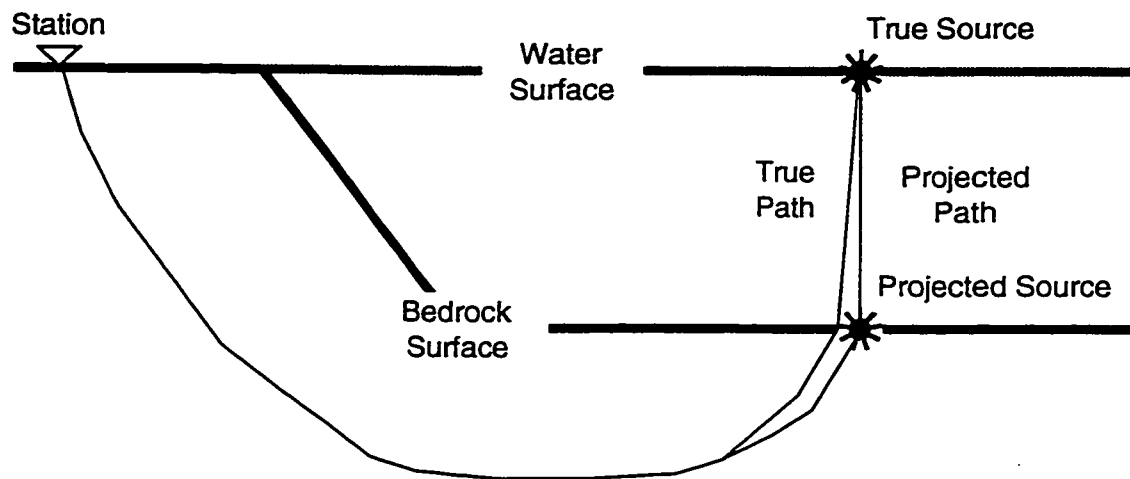


Figure 6.10: Schematic of the water projection process. The shot near the water surface is projected straight down to the bedrock surface. Since the water velocity is low, the path in the water is near vertical as consequence of Snell's Law.

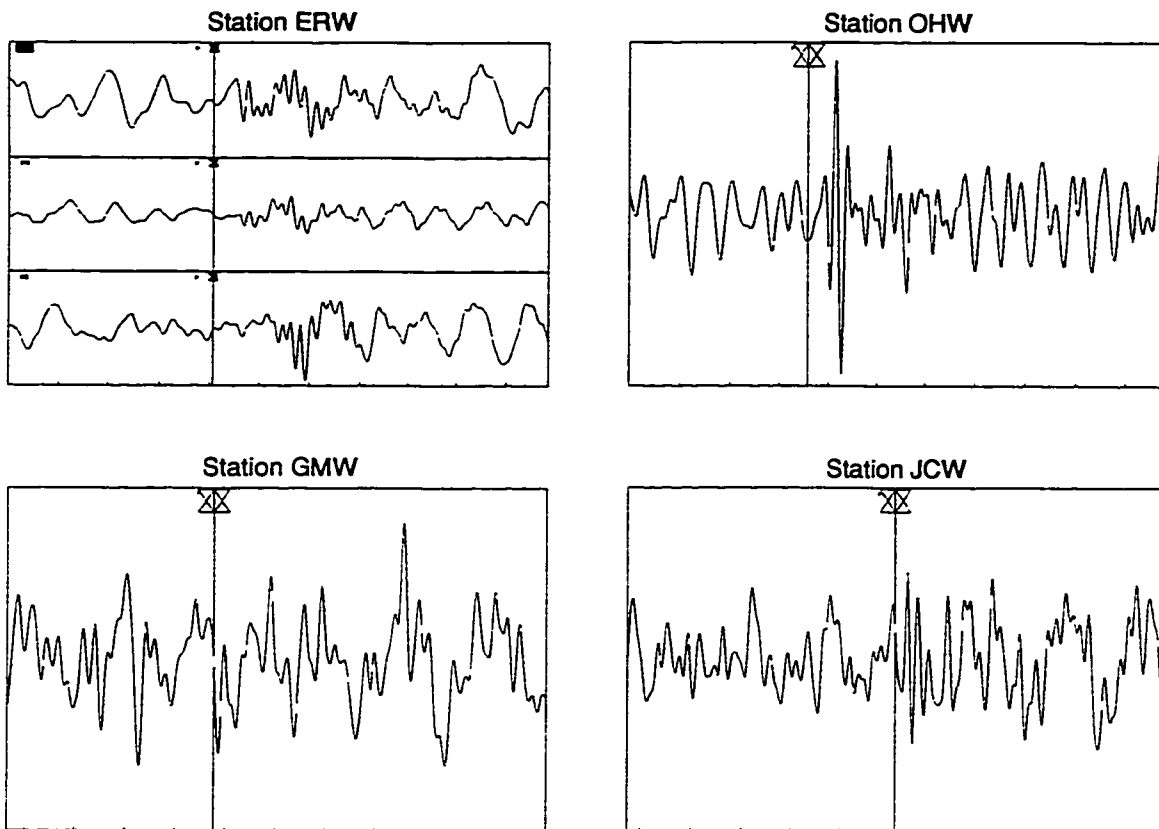


Figure 6.11: Figure showing stacks with various grades of success. At ERW and OHW the arrival is clear (on all three components at ERW). At JCW the arrival is visible as a change in frequency content, and at GMW there is no clear arrival, there are increases in energy but nothing that is an unambiguous P-wave arrival. The marks in the seismogram windows show the predicted time of the arrival using 3-D velocity model derived in *Symons and Crosson [1997]*. The large difference between the predicted and true arrival-times is an indicator of substantial information about the velocity model in this signal.

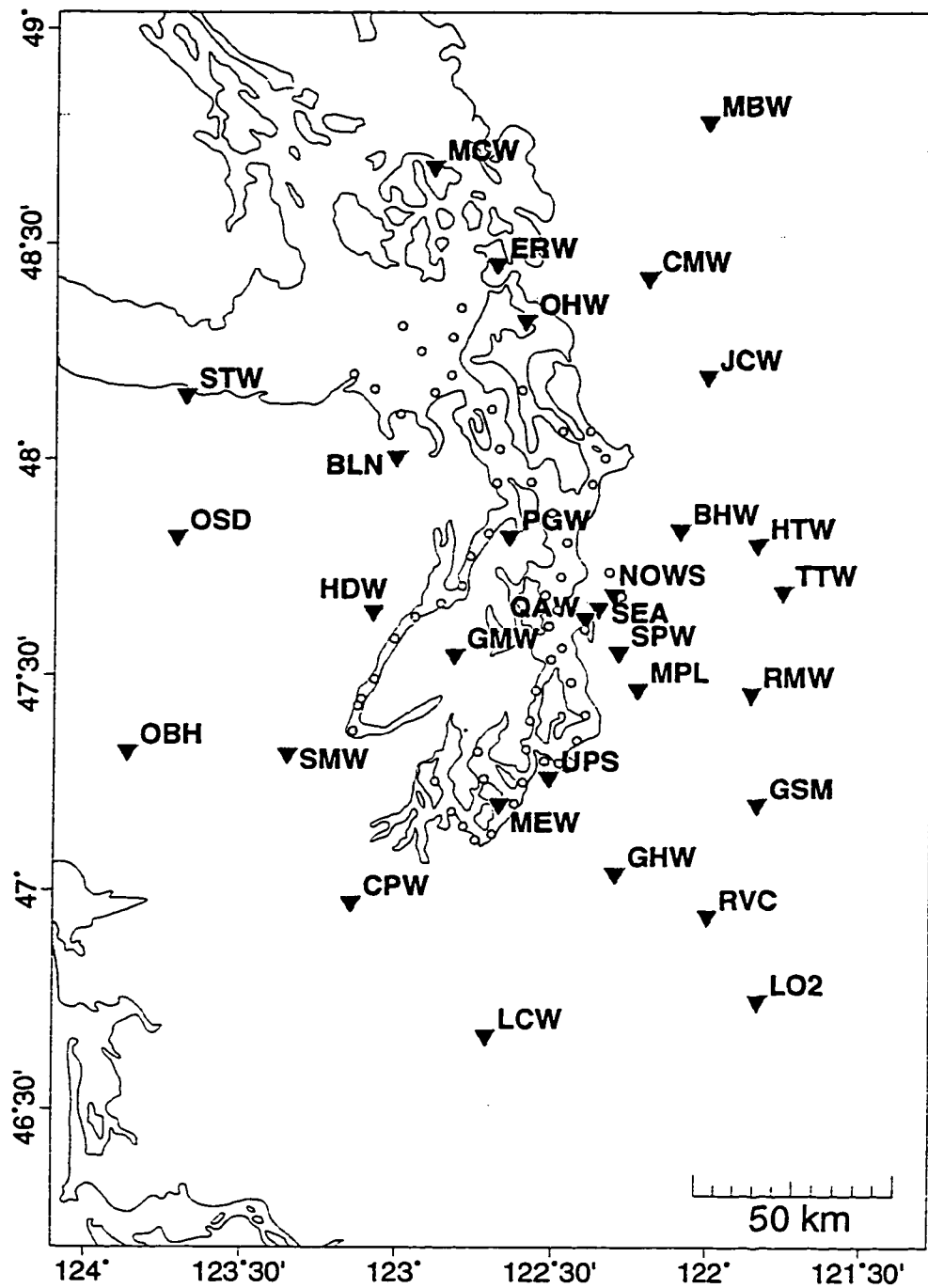


Figure 6.12: Map of stack locations used in this study and locations of permanent stations of the PNSN.

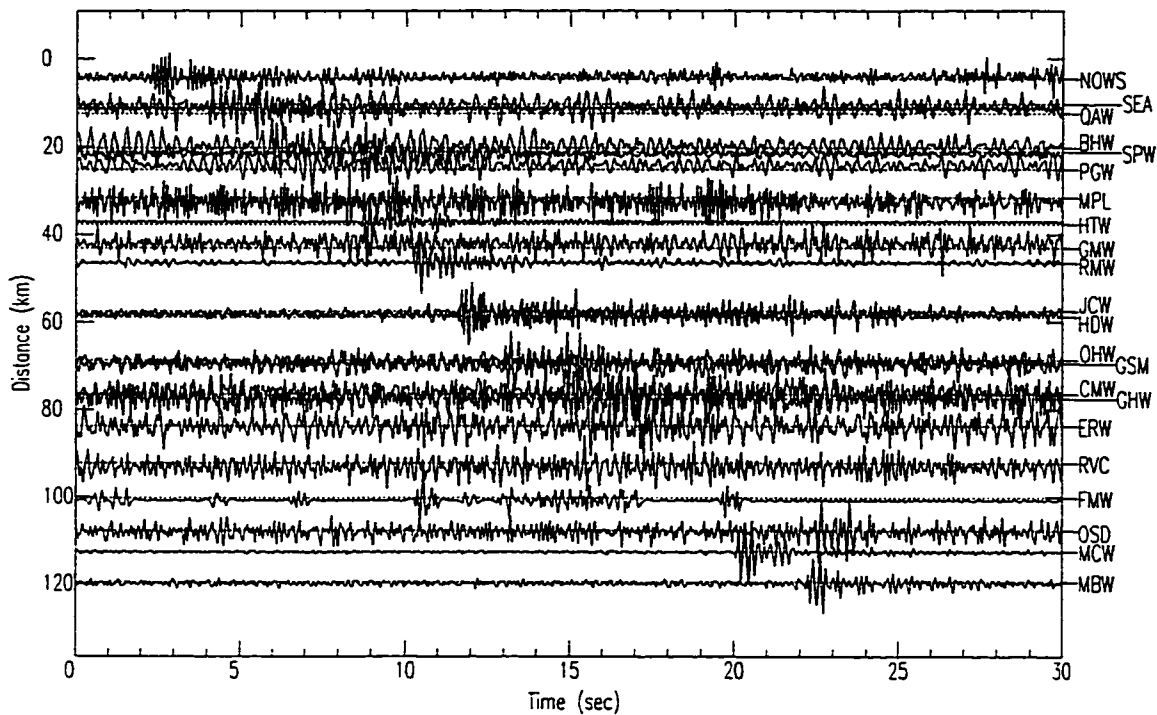


Figure 6.13: Record section showing the best stacking result. There are 21 picks on stations: NOAA/PMEL (NOWS); Seattle (SEA); Queen Anne (QAW); Seward Park West (SPW); Bald Hill (BHW); Port Gamble (PGW); Maple Valley (MPL); Haystack Lookout (HTW); Gold Mt. (GMW); Rattlesnake Mt. (RMW); Jim Creek (JCW); Hoodsport (HDW); Oak Harbor (OHW); Grass Mt. (GSM); Cultus Mt. (CMW); Garrison Hill (GHW); Mt. Erie (ERW); Voight Creek (RVC); Snow Dome (OSD); Mt. Constitution (MCW); and Mt. Baker (MBW). Not all arrivals are visible in this section because of overlap in the record section.

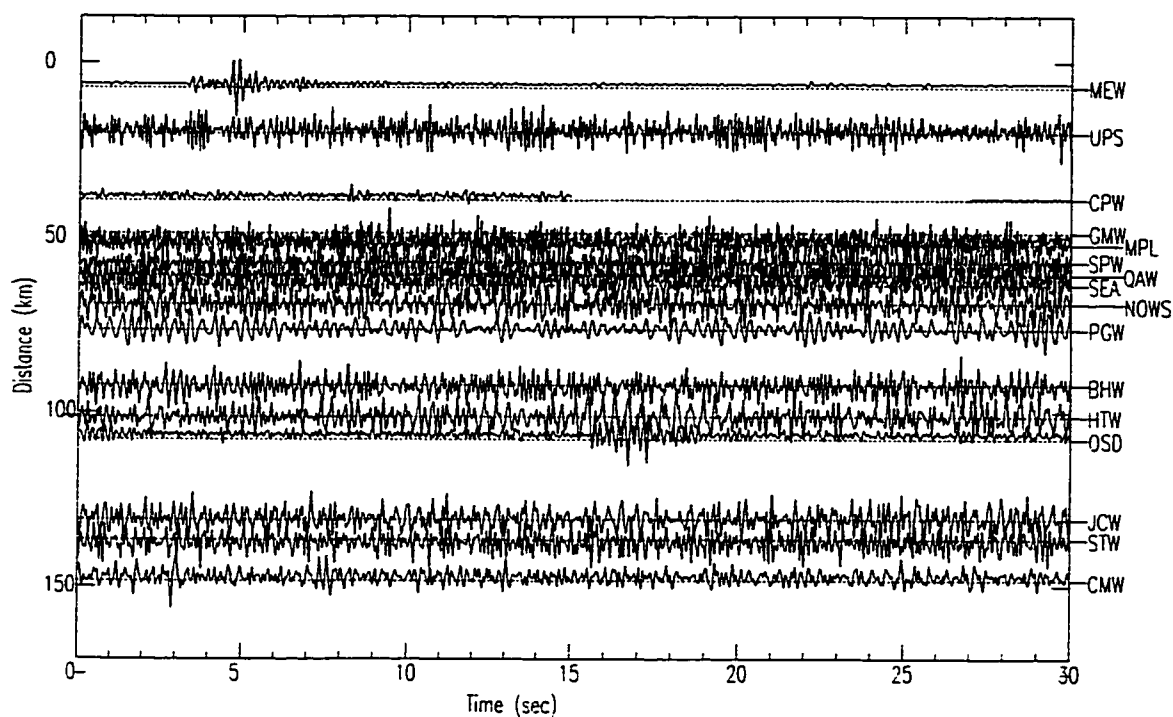


Figure 6.14: Record section showing the worst stacking result. There are 7 picks from this stack: McNeil Island (MEW); Capitol Peak (CPW); Gold Mt. (GMW); Maple Valley (MPL); Queen Anne (QAW); Seattle (SEA); Cultus Mt. (CMW).

Chapter 7

VELOCITY INVERSION USING SHIPS DATA

In this chapter, I discuss the results of an inversion incorporating a portion of the SHIPS data introduced in Chapter 6. In addition to the SHIPS data, this inversion uses the HQDS and the 1991 and 1995 explosions. After a brief discussion of the resolution of this new model I will interpret features in the Coast Range, the Puget Lowland, and the Cascade Range as in Chapter 5.

7.1 Resolution

7.1.1 Hit Comparison

Figure 7.1 shows a comparison of the sampling for a near-surface layer (3-5 km) of the model. The colors in the map show the number of rays that sample each node of the inversion grid. The comparison is based on the HQDS with and without the addition of 56 stacks of SHIPS data chosen to be well distributed in space (locations shown as yellow circles in figure 7.1 left). In the immediate Puget Sound region the results are excellent. With only earthquake data and a few explosions the near surface is sampled only in areas extremely close to stations (figure 7.1 right). After the addition of surface sources from SHIPS, this near surface region is well sampled throughout the Puget lowland. This result leads me to expect sufficient resolution in the near surface to resolve the features that are critical to understanding the seismic hazard in the GPSR. For the balance of this chapter, I will focus exclusively on the well-sampled central portion of the model from latitude $47^{\circ}45'N$ to $48^{\circ}15'N$ and from longitude $123^{\circ}45'W$ to $122^{\circ}15'W$ (a square 160 km on a side, figure 7.1).

7.1.2 *Checkerboard*

Prior to interpretation, I performed a resolution test for the region of interest. Here, the checkerboard input model used for the test is much more dense than that used for the previous resolution test in chapter 4. The characteristic size of the elements in this checkerboard (figure 7.2) is approximately 10 *km* horizontal by 6 *km* vertical (compared to 20 *km* horizontal by 10 *km* vertical in figures 4.7 and 5.2).

The shallow maps and cross section A of figure 7.2 indicate good resolution at this scale from the eastern edge of the Olympic Peninsula east through the central Puget lowland at depths of 5 – 7 *km*. At a slightly greater depth of 11 – 13 *km* the well resolved region is much larger; the sense of the perturbation is recovered through almost the entire detail region. In the immediate Seattle area the perturbation is resolved to almost its full magnitude.

7.2 *Geologic Interpretation*

The results of the inversion are shown in map and cross sections in plate 1. Figure 7.3 shows a few selected maps and cross sections with my interpretations labeled.

7.2.1 *Coast Range*

Core Rocks of the Olympic Mountains and Contacts

Plate 1 maps D, E, and F; and cross sections A, B, H, and J all show a low-velocity feature in the northwestern portion of the model between 47°30'N and 48°N and 123°W and 124°W. This feature corresponds to the core rocks of the Olympic Mountains which are expected to have low seismic velocities. Using this anomaly, I have drawn my interpretation of the contact between the high velocity rocks of the Siletzia terrane (discussed below) and the lower velocity rocks of the Olympic core complex on figure 7.3. In the east-west cross sections the contact varies from steeply dipping

($\sim 60^\circ$ in plate 1 cross section H) to overturned near the surface in plate 1 cross section J (figures 7.3 H and J show the contact). In plate 1 cross sections H and J the low velocities persist to a depth of nearly 30 km. Because of the east-dipping contact the core rocks at depth are actually 15 – 20 km east of the surface exposures of the Siletzia terrane.

From the geometry of the contact, I conclude that the accretionary prism has formed under the Siletzia terrane and warped the Siletzia upward. This is consistent with dips of the Siletzia terrane measured where the formation outcrops at the surface [Babcock *et al.*, 1992]. This is also similar to the geometry of the accretionary wedge and the Siletzia terrane imaged by Davis and Hyndman [1979] just off the coast of Vancouver Island. The difference is that on Vancouver Island the contact lies offshore; on the Olympic Peninsula the contact lies just to the west of the Puget Sound and the accretionary wedge is aurally exposed, forming the Olympic Mountains.

I suggest that the originally flat-lying formation has been warped upward along the contact with the Olympic Core. The upward warping is consistent with the only 2 crustal earthquake focal mechanisms from the study of Ma *et al.* [1996] in this portion of our study area. Events 63 and 67, from the study of Ma *et al.* [1996], indicate a maximum compressive principle stress with an east-west orientation. This is in contrast to their study as whole which found predominantly north-south oriented stress. The upward warping of the Crescent formation may result from vertical accumulation of relatively weak Olympic core sediments scraped off of the descending slab. If this model is correct, then the Crescent formation does act as the backstop to scrape sediments off the down-going Juan de Fuca slab, but the geometry is not that of the “normal” backstop (figure 7.4).

The Crescent backstop geometry shown in figure 7.4 implies that the accumulation of the accretionary wedge acts to lift the Crescent formation. Figure 7.5 shows the free-air gravitational anomaly for the GPSR measured by Finn *et al.* [1991]. The long period free-air anomaly is a measure of how well the continental crust is isostatically

compensated [*Heiskanen and Meinesz, 1958; Cordell, 1979*]. Indeed, comparison of figure 7.5 and figure 5.3 does show a relative gravity high corresponding to the surface exposures of the Crescent formation. This indicates that the elevation of the Crescent in this region is being supported elsewhere.

The western-most cross section (plate 1 cross section A and figure 7.3 A) also shows the bottom of the Olympic core complex at approximately 20 km depth. The bottom corresponds to a change in P-wave velocity from 5.9 $\frac{km}{sec}$ to 6.4 $\frac{km}{sec}$ within a 4 km change in depth. This transition is also clear in the east-west cross sections (plate 1 cross sections H and J and figure 7.3 H and J). I interpret this feature to be the intersection of the Olympic core complex with the basalts of the oceanic crust at the top of the down-going Juan de Fuca plate.

Siletzia Terrane and the Contact With the Puget Lowland

Between the low velocity rocks of the Olympic Core and the low velocities in the Puget Lowland, there are high velocity rocks of the Siletzia terrane (known locally as the Crescent formation). The geometry of the western contact with the Olympic core rocks was discussed in the previous section. The geometry of the contact between the Siletzia terrane and the Puget Lowland is most clear in plate 1 map C although the high velocity anomaly is first visible in plate 1 map B and persists to plate 1 map E which is the deepest layer to which the low velocities of the Puget Lowland persist. Plate 1 map C shows the horseshoe shape of the Siletzia terrane that is similar to the geology shown in figure 5.3.

In plate 1 maps C and D and figure 7.3 the horseshoe shaped contact between the Siletzia terrane and the Puget Lowland is broken by an eastward excursion of the high velocity corresponding, on the surface, with the Blue Hills (figures 5.3 and 7.3) a local out-crop mapped as a portion of the Siletzia terrane [*Johnson et al., 1996*].

In plate 1 map D there is another break in the horseshoe shape of the Siletzia-Puget Lowland contact north of the Blue Hills. This feature does not correspond

to any surface features but it is just south the line of the southern Whidbey Island fault (SWIF) (figure 7.3 map). The SWIF was postulated by *Gower et al.* [1985] and identified, primarily from seismic reflection data, by *Johnson et al.* [1996]. *Johnson et al.* [1996] identify the southern Whidbey Island fault zone as a broad region (6–11 km wide) with splays exhibiting strike-slip, reverse, and thrust displacement. There is a less well defined high velocity perturbation along a line just south of the SWIF that connects this feature with the well defined high velocity in the northwest corner of plate 1 map D. The well defined high velocity region in the northwest corner of the map corresponds to an out-crop of Siletzia terrane on the southern tip of Vancouver Island. This out-crop is separated from the rest of Vancouver Island by the Leech River and San Juan–Survey Mountain Faults which *Johnson et al.* [1996] interpreted as the western end of the SWIF. A linear northwest-southeast trending feature persists in this portion of the model from a depth of 7 km (plate 1 map D) to a depth of 15 km (plate 1 map F). The line moves northeast as the depth increases so I infer a slight northeast dip for the SWIF zone, consistent with the results of *Johnson et al.* [1996] based on seismic reflection surveys at much lower depth. The structure continues off the eastern edge of this map in plate 1 map F.

In the center of the southern edge of plate 1 maps C and D and figure 7.3 C and D there is another high high velocity feature identified as what eventually crops out at the surface as the Black Hills (figure 7.3 map). Although this feature does not persist all the way to the surface I believe this is a function of poor resolution at the near surface with good resolution at greater depths (figure 7.2). Plate 1 cross section C shows a cross sectional view which passes through this structure. *Pratt et al.* [1997] identify the fault separating the Black Hills and the Tacoma basin as a south dipping thrust fault. Since their seismic reflection results end at the south end of the Puget Sound, their interpretation is based on the mapped dip of the Doty fault (south of this boundary) which dips to the south. Based on the tomography, I interpret the boundary between the Black Hills and the Tacoma basin as a north dipping thrust

fault (figure 7.3 D). This is also more consistent with historical subsidence in the region [Sherrod, 1998].

7.2.2 Puget Lowland

Sedimentary Basins

The most obvious features in the upper 10 *km* of the detail map (plate 1 maps A-D and figure 7.3) are the low velocity regions below the cities of Seattle and Tacoma. The minimum velocity under the city of Seattle is $\sim 2.5 \frac{km}{sec}$ directly under station SEA (a Wood-Anderson seismometer in the basement at the University of Washington; appendix D). For comparative purposes, sonic logs from the Socal-Schroeder #1 well slightly north of Lake Washington average $\sim 3.0 \frac{km}{sec}$ through the upper 2.5 *km* of sedimentary rocks [Brocker and Ruebel, 1998]. The package of sedimentary rocks is much thinner at Socal-Schroeder #1 since the well is located north of the main portion of the Seattle basin. Plate 1 cross section J shows the region of low velocity persisting to a depth of ~ 10 *km* below Seattle. This is in contrast to the results of Pratt *et al.* [1997] which showed low velocities persisting to a depth of only 6.5 *km* in the Puget Sound just west of Elliott Bay; approximately 15 *km* west of the slowest inverted velocities in our model.

The size and magnitude of the low velocity region below Seattle could have a large effect on the intensity of shaking experienced in the city during a large earthquake. For this reason I performed a resolution kernel test specific to this region in order to assess the reliability of these results. Since the Seattle and Tacoma basins are relatively widely separated in space we can save time by performing the resolution test in both simultaneously. Since we are interested in the resolution with regard to low velocity basins, the perturbation is a negative one. This is significant because we are using only the first arrival; with a low velocity perturbation energy will tend to move around the perturbation and this will affect the resolution. The resolution

test (figure 7.6) indicates that a shallow low velocity region in the Seattle area is recoverable to almost its full magnitude and does not significantly smear in depth. A perturbation in the Tacoma region is not quite as well recovered and there is some smearing, a 6 km synthetic perturbation shows as a 10 km deep perturbation in the inverted result.

The recovery of the correct anomaly depth under Seattle leads me to believe that low velocities do persist to a depth of 10 km directly under the city of Seattle. This requires a slope on the bottom of the basin that is down to the east from Elliott bay (where the refraction study of *Pratt et al.* [1997] constrains the depth to the bottom of the basin to 6.5 km) to under the U of W (where this study constrains the depth of the basin to 10 km). The smearing of the resolution kernel test in Tacoma suggests that this study does not have the necessary resolution to give a good constraint on the depth of the Tacoma basin, although our data suggests a range of 5–10 km.

Without the data from the temporary SHIPS stations it is difficult to define the eastern edge of the Seattle basin with any degree of accuracy. However, the western edge is well constrained. Directly west of West Seattle, the edge of the basin is coincident with the contact between high velocity rocks of the Blue Hills and lower velocity rocks to the east. This contact lies almost exactly under the city of Bremerton (plate 1 map C), and can be seen as an anomaly in the contact between the rocks of the Siletzia terrane and the lower velocity rocks of the central Puget lowland. This contact generally follows Hood Canal except for an eastward jump at the Blue Hills (under PNSN stations GNW and GMW; appendix D).

There is less clear evidence of a low velocity region under Everett in plate 1 map C. Compared to the distinct regions of low velocity under Seattle and Tacoma, the Everett Basin is a more spread-out low-velocity patch to the north of Seattle. Examination of the checkerboard test in this area (figure 7.2) does show relatively poor resolution toward in the upper portion of this feature, so the northern boundary is not well constrained and the full magnitude of the anomaly is not expected to be

recovered. However, the existence of the Everett basin is significant and clear from the tomography results.

7.2.3 Cascade Range

Although the contact between the Puget Lowland and the Cascade Range is not terribly well constrained, plate 1 maps C and D show the eastern edge of the Puget lowland as a transition into high velocity material (figure 7.3 H and J *Cascade front*). This transition strikes almost due north in plate 1 map C. The geometry of the transition is more complex in plate 1 map D (the contact is not linear). This is probably the result of uplift of the basement of the Puget Lowland. Topographically, this transition corresponds to the start of the foothills of the Cascade mountains. I interpret this transition as the contact between the basement of the Puget Lowland (the Siletzia terrane) and the pre-tertiary basement of the Cascade Range. Unfortunately, this model has insufficient resolution to determine whether this is an active structure or a suture zone.

Duvall Earthquake

The transition from the Puget Lowland into the higher velocity material of the Cascade range is not imaged across the entire map, but there is a well resolved portion in the neighborhood of the May 2, 1996 Duvall earthquake (M_c 5.3). This earthquake is discussed in detail in *Thomas et al.* [1996]. The centroid moment tensor and the first motion focal mechanism agree that this event resulted from either a west or an east dipping thrust fault. The tomography (plate 1 cross section H) indicates a contact in this exact region. It seems likely that the Duvall earthquake occurred on a small fault that is part of this observed contact. Unfortunately, the resolution of the model is not sufficient in this region to show the actual fault.

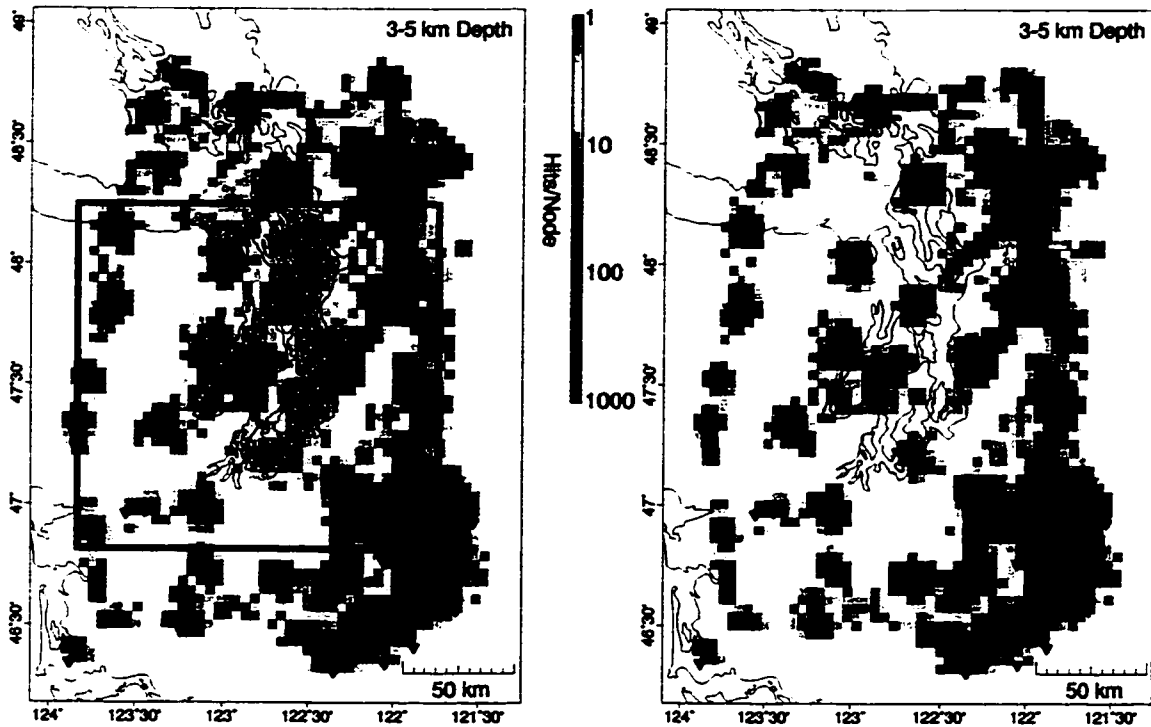


Figure 7.1: Comparison of the number of hits/node with (left) and without the SHIPS data (right). In both maps completely un-sampled regions are shown as uncolored. The yellow dots are the locations of the SHIPS shots used in this comparison. The color map is based on the number of rays sampling a given node. Box in left map shows the region selected for detailed analysis in this chapter.

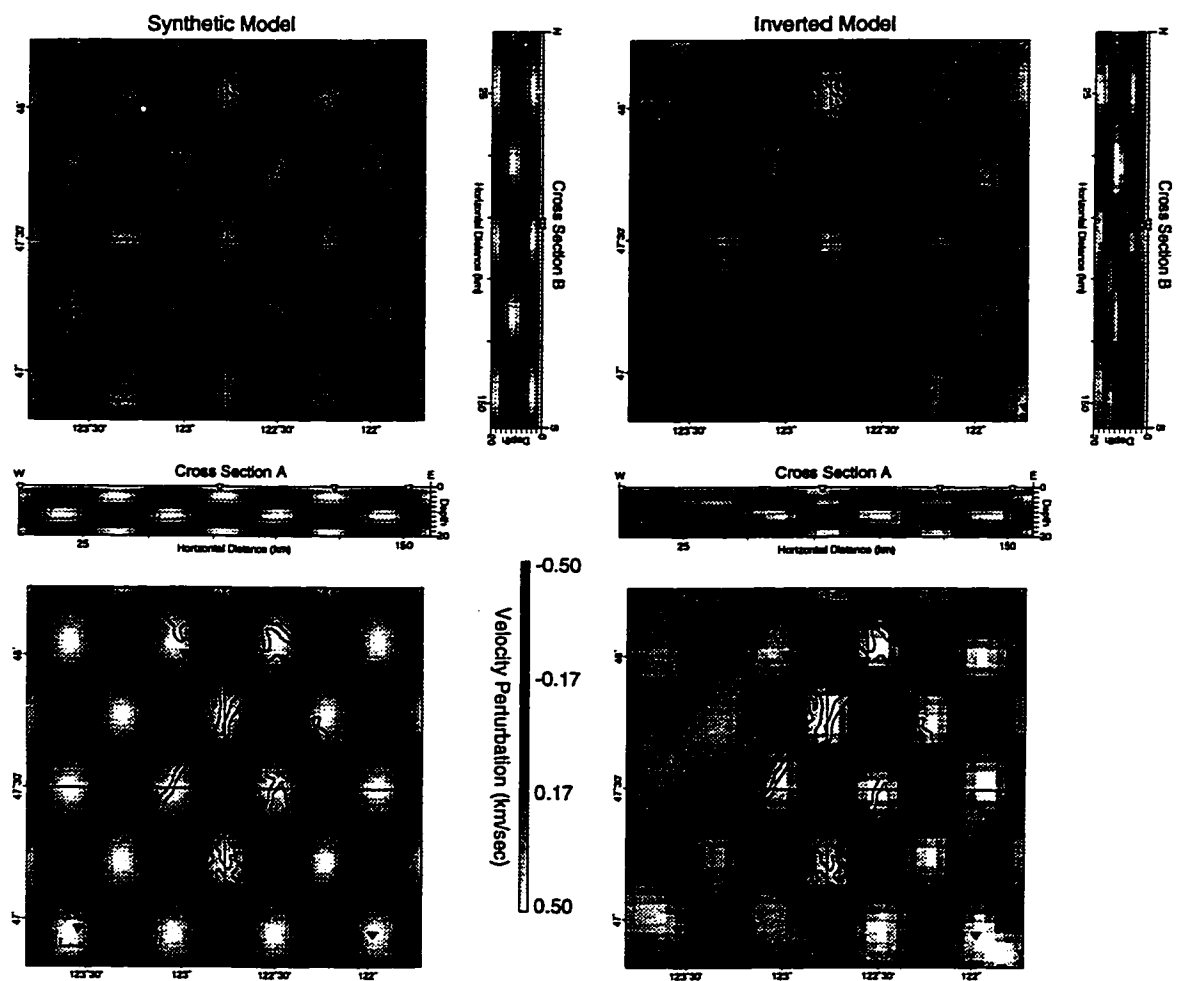


Figure 7.2: Comparison of synthetic (left) and inverted (right) checkerboard using the SHIPS data. Compared to the checkerboard in Chapter 4 these perturbations are much smaller.

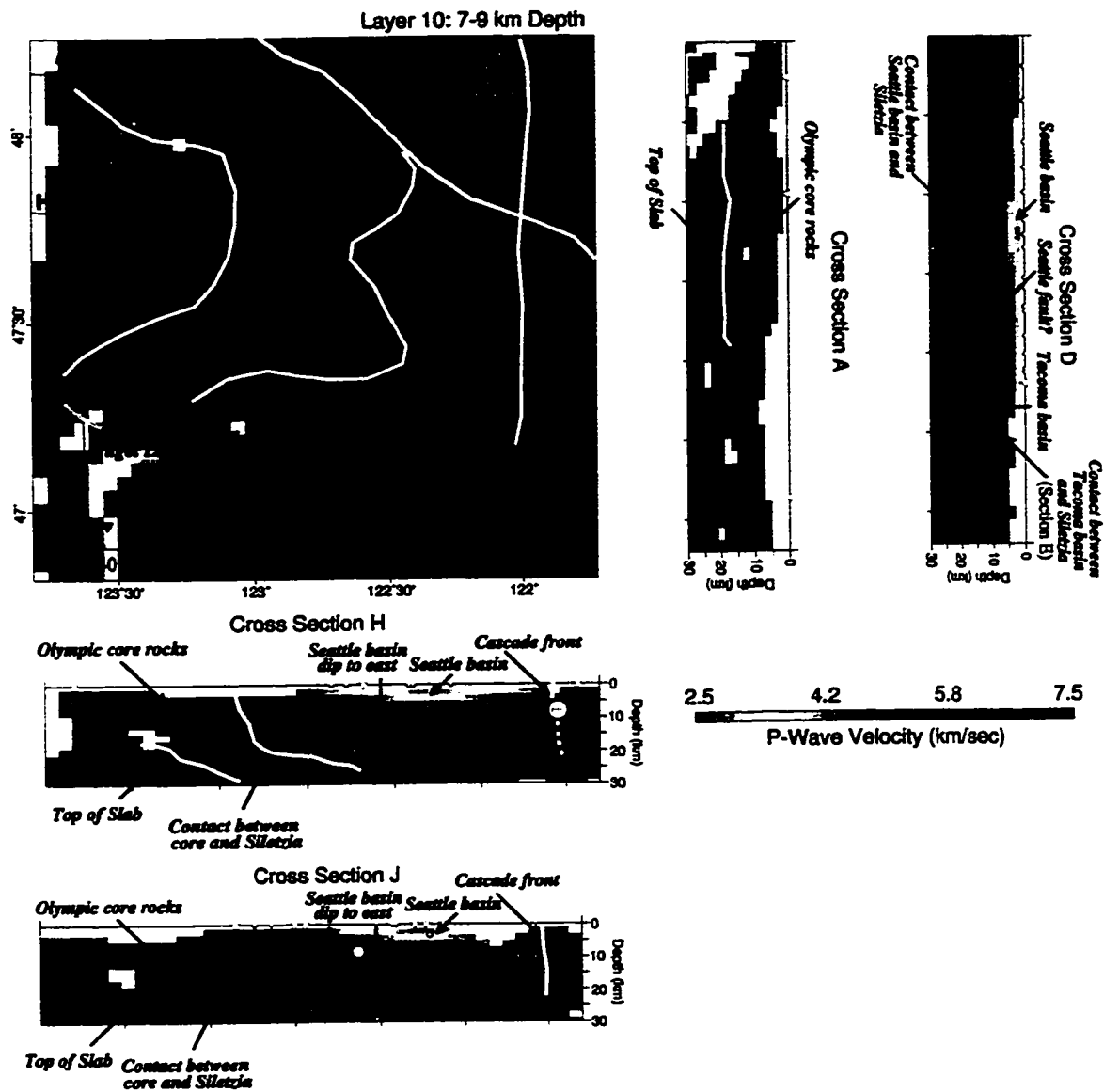


Figure 7.3: Map and several cross sections (from plate 1) with my interpretations labeled. There is no vertical exaggeration on the cross sections.

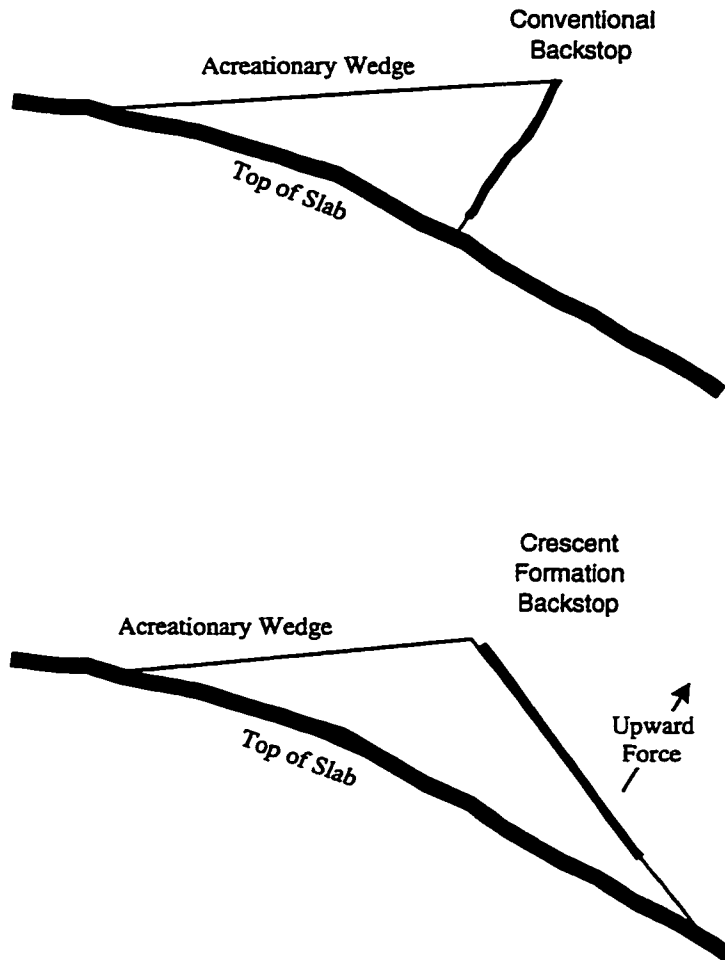


Figure 7.4: Comparison of the standard geometry for an accretionary wedge backstop (Top). And the geometry for the Crescent formation backstop interpreted in this study (Bottom). Since the Crescent dips the same direction as the subducting slab there is an upper force imparted by the accumulating sediments.

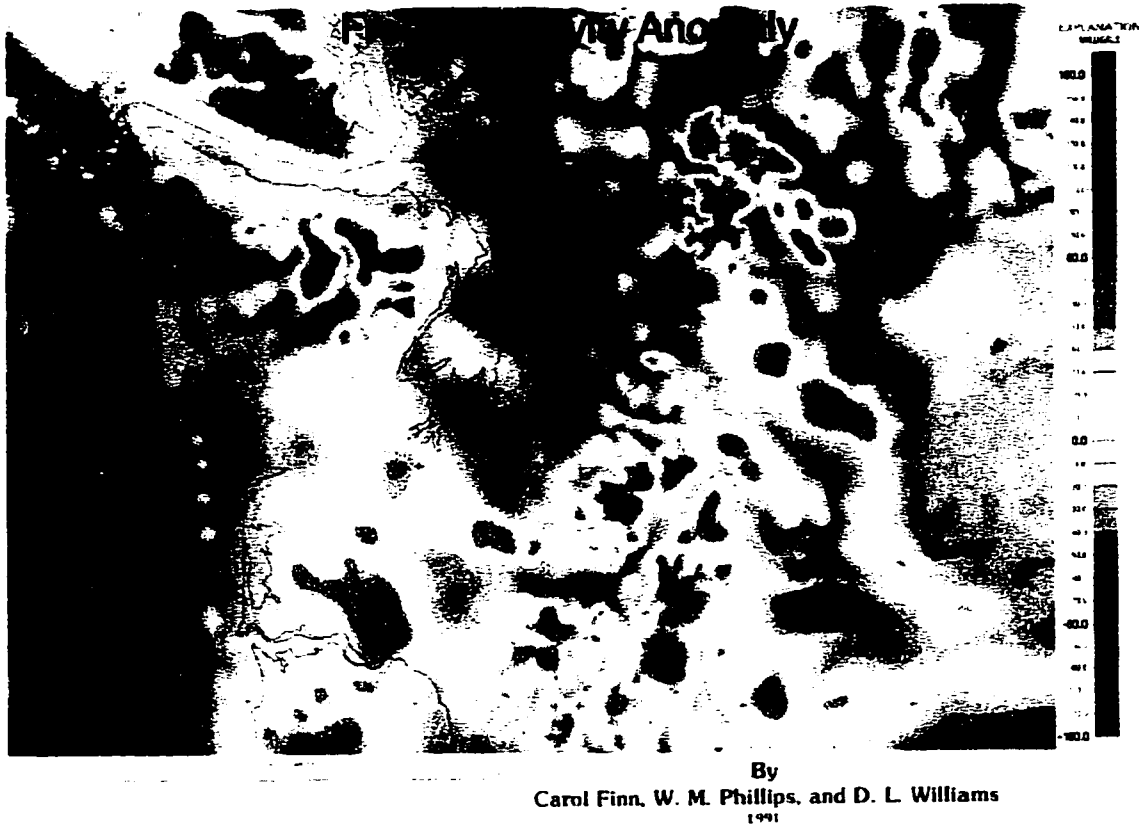


Figure 7.5: Map of the free-air gravity anomaly of the GPSR from *Finn et al.* [1991]. The long wavelength portion of this anomaly is a measure of crustal isostatic compensation.

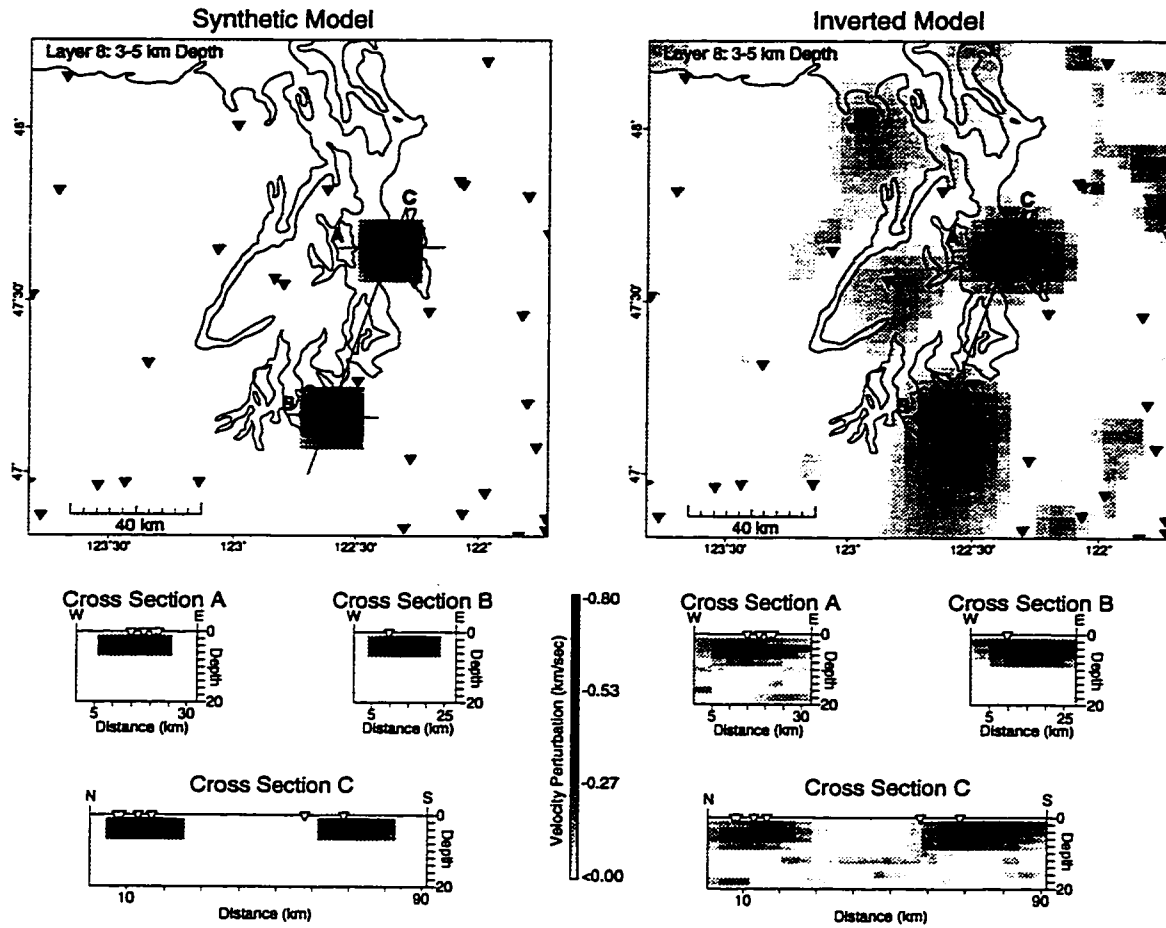


Figure 7.6: A map and cross sections through a resolution kernel test for low velocity regions below the cities of Seattle and Tacoma.

Chapter 8

CONCLUSIONS

In this dissertation I have described a non-linear seismic tomography experiment in the Greater Puget Sound Region (GPSR). The GPSR contains portions of three distinct geologic provinces: (1) the Coast Range Province—composed of the Olympic Mountains and the Siletzia terrane lying along the Washington Coast (the western edge of the GPSR). (2) The Puget Lowland—an approximately linear depression that stretches from Oregon’s Willamette Valley to the Strait of Georgia in Canada. The Puget Lowland lies in the middle of the GPSR. (3) The Cascade Range—lying along the eastern edge of the GPSR and characterized by extensive episodic volcanism since the later Mesozoic.

The result of this study is a three-dimensional model of the P-wave velocity within the GPSR. Interpretation of this model provides information about the subsurface geology in the region. The method used to perform the tomography has been developed as part of this research. The method uses a finite-difference algorithm to calculate seismic travel-times to every point in the region using the full 3-d velocity model.

8.1 Data

The method is capable of using three different types of data: (1) Earthquakes with unknown hypocenters. The earthquake hypocenters are found as part of the model during solution of the tomography problem. (2) Explosions or other seismic events with known locations. (3) External data constraining the seismic velocity at known

locations within the model.

Within the GPSR earthquakes are the most numerous type of data. During this experiment I have examined the resolution possible using two different sets of earthquakes. First, the complete data set (CDS) consists of all earthquakes within the GPSR that meet a specific set of selection criteria. The arrival-time picks in the CDS are un-reviewed. Next, a high-quality subset (HQDS) of the CDS. These are the best events from within the GPSR selected to keep as many of the unique ray-paths as possible. The HQDS has been re-picked so that we have more confidence in the accuracy and consistency of the observations. Comparison shows that the HQDS provides almost the same resolution as the CDS, and the inversion takes only half as much time to complete.

Our study also includes 20 explosions within the GPSR which were used in wide-angle reflection–refraction line experiments performed in 1991 and 1995. The explosions are used directly in the inversion since their locations are known. The 2-D interpretation of the velocity structure resulting from the 1991 experiment is also incorporated into the inversion as external constraints.

The last source of data included in the inversion are shots of the 1998 Seismic Hazards in the Puget Sound (SHIPS) experiment. During SHIPS, about 30,000 air gun shots were fired at approximately 100 *m* intervals in the waterways of western Washington and British Columbia. We stacked waveforms recorded at about 50 PNSN stations to obtain approximately 1000 travel-times of first arriving compressional waves from as uniform as possible a distribution of shots. The addition of the SHIPS data to the existing earthquake dataset improves the resolution in the upper 20 *km* of our model.

8.2 Features of the Model

I have interpreted two separate models. The first model was complete before the SHIPS experiment and shows a number of large surface and deep features. The second model includes data from the SHIPS experiment and interpretation is confined to the near surface in the central portion of the GPSR where the resolution is improved by the inclusion of the additional data. Significant findings include:

- Coast Range Features
 - A spectacular image of the accretionary prism which forms the Olympic Mountains. The model velocities are constant with laboratory measured velocities of metagraywacke–quartz-mica-schist facies rocks to a depth of 25 *km*.
 - An excellent correlation between the low velocity material in this model and the low gravity feature along the Washington coast.
 - The contact between the core rocks of the Olympic Mountains and the Siletzia terrane (known as the Crescent formation in this area). The core rocks underlie the Siletzia terrane. The Siletzia terrane dips down to the east over the contact with the Olympic core rocks. The conclusion is that the accumulation of the sediments that are being pushed up to form the Olympic Mountains underneath the Siletzia terrane has warped these rocks upward.
 - At the contact with the Olympic core, our model shows a thickness for the Siletzia terrane of ~ 20 *km*, consistent with measurements of the surface geology by *Babcock et al.* [1992].
 - Shallow high velocity features in the model correspond to isolated outcrops of the Siletzia terrane at the Blue Hills near Bremerton and the Black Hills south of Tacoma.

- The basal contact between the low velocity rocks of the Olympic core complex and higher velocity material ($\sim 6.5 \frac{km}{sec}$) which we interpret as the top of the down-going Juan de Fuca slab. Approximately 10 km below the top of the Juan de Fuca slab there is another increase in velocity to $\sim 8 \frac{km}{sec}$. I interpret this as the bottom of the oceanic crust.
 - The model also includes a northern contact between the Siletzia terrane and lower velocity material. The contact corresponds to the Southern Whidbey Island Fault described by *Johnson et al.* [1996].
- Puget Lowland Features
 - Well defined low velocity features in the model correspond to sedimentary basins under the cities of Seattle, Tacoma, Everett, and Chehalis. The best imaged is the Seattle basin, which is 10 km deep under the University of Washington. This is deeper than the 6.5 km described by *Pratt et al.* [1997] in the Puget Sound just west of Elliott Bay.
 - There is a good correspondence between the velocity of the center of the Seattle basin in this model ($\sim 2.5 \frac{km}{sec}$) and well logs for unconsolidated sediments in the upper 2.5 km of the Socal-Schroeder #1 well slightly north of Lake Washington ($\sim 3.0 \frac{km}{sec}$) [*Brocker and Ruebel*, 1998].
 - The western edge of the Seattle basin is well constrained at the contact with the Siletzia terrane. Unfortunately, the eastern edge is not well constrained with this data set.
 - In general the Tacoma basin is not as well constrained. However, the southern edge lies against a shallow velocity anomaly corresponding to the Black Hills. The geometry of the contact between these two features suggests a south-dipping thrust fault; consistent with regional subsidence, but in disagreement with the model of *Pratt et al.* [1997].

- Cascade Range Features

- The model shows the eastern edge of the Puget lowland as a transition into high velocity material along a contact striking nearly due north. Topographically this corresponds to the start of the foothills of the Cascade mountains. While I cannot definitively constrain the eastern edge of the Siletzia terrane, it appears to extend at least 30 *km* east from the eastern edge of the waterways of the Puget Sound.
- Although the contact between the Siletzia terrane and the Cascade basement is not imaged across the entire section, there is a well resolved portion in the neighborhood of the May 2, 1996 Duvall earthquake (M_c 5.3). It seems likely that the Duvall earthquake occurred on a small fault that is part of this structure.

- Deep Features

- At ~ 35 *km* the velocity jumps to $\sim 8 \frac{km}{sec}$, I interpret this as the Moho.
- Approximately 15 *km* below the Moho there is a low velocity region. The velocity reversal is probably the basalt that forms the oceanic crust on the Juan de Fuca slab. However, the low velocities could be serpentinized mantle if the basalt has transformed to eclogite.

8.3 Future Work

The SHIPS experiment provided a large amount of high quality data which has only just begun to be analyzed. The models shown in this dissertation were inverted with no data from the large temporary deployment of seismometers which were a major component of SHIPS. The inclusion of the SHIPS data from the permanent stations of the PNSN resulted in a large improvement in the quality of the model in the upper 20 *km*, but there are still many questions that are unanswered.

The models discussed in this dissertation do not have sufficient resolution to explore the terminating features of the basins in the Puget Lowland. Further analysis will almost certainly lead to the identification of heretofore unknown faults. The geometry of the contact between the Cascade Range and the Siletzia terrane is poorly resolved in this study, understanding this feature is critical to interpretation of the current tectonic regime in the GPSR.

In addition to providing higher resolution P-wave velocity models by using data from the temporary SHIPS seismic deployment, it is possible that the 3-component SHIPS stations might provide enough data for the inversion of an S-wave velocity model. The S-wave structure is critical for modeling the strong-motion response of the region; and, at present, there is very little data to address this question.

Bibliography

- Ammon, C. J., and J. E. Vidale, Tomography without rays, *Bull. Seis. Soc. Am.*, *83*, 509–528, 1993.
- Atwater, B. F., A Seattle tsunami 1100 years ago (abstract), *Abstracts with Programs - Geological Society of America*, *24*(5), 4, 1992.
- Atwater, B. F., Coastal evidence for great earthquakes in western Washington, *U.S. Geological Survey Professional Paper*, *1560*, 77–90, 1996.
- Atwater, T., Implications of plate tectonics for the Cenozoic tectonic evolution of western North America, *Geol. soc. Am. Bull.*, *81*, 3523–3536, 1970.
- Babcock, R. S., R. R. Burmester, K. P. Clark, D. C. Engebretson, and A. Warnock, A rifted margin origin for the Crescent basalts and related rocks in the Northern Coast Range Volcanic Province, Washington and British Columbia, *J. Geophys. Res.*, *97*(B5), 6799–6821, 1992.
- Backus, G., and F. Gilbert, The resolving power of gross earth data, *The Geophysical Journal of the Royal Astronomical Society*, *16*(2), 169–205, 1968.
- Bear, L. K., and G. L. Pavlis, Estimation of slowness vectors and their uncertainties using multi-wavelet seismic array processing, *Bull. Seis. Soc. Am.*, *87*(3), 755–69, 1997.
- Bonini, W. E., D. W. Hughes, and Z. F. Danes, Complete Bouguer Gravity Anomaly Map of Washington, Geologic Map GM-11, Washington State Department of Natural Resources, 1974.
- Brandon, M. T., and A. R. Calderwood, High-pressure metamorphism and uplift of the Olympic subduction complex, *Geology*, *18*, 1252–1255, 1990.

- Brocker, T. M., and A. L. Ruebel, Compilation of 29 sonic and density logs from 23 oil test wells in western Washington state, Tech. rep., USGS Open File Report 98-249, 1998.
- Bucknam, R. C., H. E. Hemphill, and E. B. Leopold, Abrupt uplift within the past 1700 years at southern Puget Sound, Washington, *Science*, 258(5088), 1611-14, 1992.
- Cady, W. M., Tectonic setting of the Tertiary volcanic rocks of the Olympic Peninsula, Washington, *J. Res. U.S. Geol. Surv.*, 3, 573-582, 1975.
- Chapman, C. H., and J. A. Orcutt, Least-squares fitting of marine seismic refraction data, *Geophys. J. R. Astr. Soc.*, 82, 339-374, 1985.
- Christensen, N. I., and W. D. Mooney, Seismic velocity structure and composition of the continental crust: A global view, *J. Geophys. Res.*, 100(B7), 1995.
- Constable, S. C., R. L. Parker, and C. G. Constable, Occam's inversion: A practical algorithm for generating a smooth model from electromagnetic sounding data, *Geophysics*, 52(3), 289-300, 1987.
- Cordell, L., Gravimetric expression of graben faulting in Santa Fe County and the Espanola basin, New Mexico, in *Guidebook of Sante Fe Country*, edited by R. V. Ingersol, vol. 30th Field Conference, pp. 59-64, New Mexico Geological Society, 1979.
- Cowan, D. S., and C. J. Potter, Continent-Ocean Transect B3: Juan de Fuca Spreading Ridge to Montana Thrust Belt, *Bull. Geol. Soc. Am.*, 9999, 000-999, 1986.
- Crosson, R., Crustal structure modeling of earthquake data 1. Simultaneous least squares estimation of hypocenter and velocity parameters, *J. Geophys. Res.*, 81(17), 3036-3046, 1976a.

- Crosson, R., Crustal structure modeling of earthquake data 2. Velocity structure of the Puget Sound region, Washington, *J. Geophys. Res.*, *81*(17), 3047–3054, 1976b.
- Crosson, R., and T. Owens, Slab geometry of the Cascadia subduction zone beneath Washington from earthquake hypocenters and teleseismic converted waves, *Geophys. Res. Lett.*, *14*, 824–827, 1987.
- Crosson, R. S., and J. M. Lees, Regularization or smoothing in inversion and seismic tomography as a linear filtering operation, *Eos Trans. AGU*, *70*(2), 601, 1989, (Abstract).
- Davis, E. E., and R. D. Hyndman, Accretion and recent deformation of sediments along the northern Cascadia subduction zone, *Bull. Geol. Soc. Am.*, *101*, 1465–1480, 1979.
- Dewberry, S. R., and R. S. Crosson, The M_D 5.0 earthquake of 29 January 1995 in the Puget lowland of western Washington: an event on the Seattle fault?, *Bull. Seis. Soc. Am.*, *86*(4), 1167–72, 1996.
- Duncan, R. A., A captured island chain in the Coast Range of Oregon and Washington, *J. Geophys. Res.*, *87*(B13), 10,827–10,837, 1982.
- Duncan, R. A., and L. D. Kulm, Plate tectonic evolution of the Cascades arc-subduction complex, in *The Geology of North America*, edited by E. L. Winterer, D. M. Hussong, and R. W. Decker, vol. The Eastern Pacific Ocean and Hawaii, pp. 413–438, Geological Society of America, 1989.
- Efron, B., and R. J. Tibshirani, *An introduction to the Bootstrap*, vol. 57 of *Monographs on Statistics and Applied Probability*, chap. The jackknife, pp. 141–152, Chapman and Hall, 1993.

- Engebretson, D., A. Cox, and R. Gordon, *Relative motions between oceanic and continental plates in the Pacific Basin*, Special Paper, Geological Society of America, 206th edn., 1985.
- Evarts, R., R. Ashley, and J. Smith, Geology of the Mount St. Helens area: Record of discontinuous volcanic and plutonic activity in the Cascade arc of southern Washington, *J. Geophys. Res.*, *92*, 10155–10169, 1987.
- Finn, C., Geophysical constraints on Washington convergent margin structure, *J. Geophys. Res.*, *95*, 19533–19546, 1990.
- Finn, C., W. M. Phillips, and D. L. Williams, Gravity anomaly and terrain maps of Washington, Geophysical investigations series, Department of the Interior; U.S. Geological Survey, 1991.
- Gower, H. D., J. C. Yount, and R. S. Crosson, Seismotectonic map of the Puget Sound region, Washington, Dept. of Interior, U.S. Geological Survey, Miscell. Invest. Series Map I-1613, 1985.
- Gridley, J. M., Crustal structure of western Washington State, Ph.D. thesis, University of Texas at El Paso, El Paso, Texas, 1993.
- Hall, J. B., and K. L. Othberg, Thickness of unconsolidated sediments, Puget lowland, Washington, Geologic Map GM-12, Washington Div. Geol. Earth Res., 1974.
- Heiskanen, W. A., and F. A. V. Meinesz, *The earth and its gravity field*, McGraw-Hill, 1958.
- Hole, J. A., Nonlinear high-resolution three-dimensional seismic travel time tomography, *Geoph. J. Int.*, *97*, 6553–6562, 1992.
- Hole, J. A., and B. C. Zelt, 3-D finite-difference reflection traveltimes, *Geoph. J. Int.*, *121*, 427–434, 1995.

- Johnson, C. E., A. Bittenbinder, B. Bogaert, L. Dietz, and W. Kohler, Earthworm: A flexible approach to seismic network processing, *IRIS Newsletter*, 14(2), 1–4, 1995.
- Johnson, S., Evidence for a margin-truncating transcurrent fault (pre-late Eocene) in Western Washington, *Geology*, 12, 538–541, 1984.
- Johnson, S., C. Potter, and J. Armentrout, Origin and evolution of the Seattle fault and Seattle basin, Washington, *Geology*, 22, 71–74, 1994.
- Johnson, S. Y., Eocene strike-slip faulting and nonmarine basin formation in Washington, in *Strike-Slip Deformation, Basin Formation, and Sedimentation*, vol. 37, pp. 283–302, Spec. Pub. Soc. Econ. Paleontol. Mineral., 1985.
- Johnson, S. Y., C. J. Potter, J. M. Armentrout, J. J. Miller, C. Finn, and C. S. Weaver, The southern Whidbey Island fault: An active structure in the Puget Lowland, Washington, *Bull. Geol. Soc. Am.*, 108, 334–354, 1996.
- Kirby, S. H., E. R. Engdahl, and R. Denlinger, Intermediate-depth intraslab earthquakes and arc volcanism as physical expressions of crustal and uppermost mantle metamorphism in subducting slabs (overview), in *Subduction Top to Bottom*, edited by G. E. Bebout, D. W. Scholl, S. H. Kirby, and J. P. Platt, no. 96 in Geophysical Monograph Series, pp. 195–214, American Geophysical Union, 1996.
- Lees, J. M., Xmap8: A free program for three-dimensional GIS, *Seis. Res. Lett.*, 66(4), 33–37, 1995.
- Lees, J. M., and R. S. Crosson, Tomographic imaging of local earthquake delay times for 3-D velocity variation in western Washington, *EOS*, 70(9), 139, 1989, (Abstract).

- Lees, J. M., and R. S. Crosson, Tomographic imaging of local earthquake delay times for three-dimensional velocity variation in western Washington, *J. Geophys. Res.*, *95*, 4763–4776, 1990.
- Ludwin, R. S., C. S. Weaver, and R. S. Crosson, Seismicity of Washington and Oregon, in *Neotectonics of North America*, edited by D. B. Slemmons, E. R. Engdahl, M. D. Zoback, and D. D. Blackwell, Decade Map Volume 1, pp. 77–97, Geological Society of America, Boulder, Colorado, 1991.
- Luetgert, J., T. Parsons, K. Miller, G. R. Keller, A. Trehu, S. Fleming, R. Clowes, and I. Asudeh, Crustal architecture of the Pacific Northwest: The 1995 seismic transect across southern Washington (abstract), *EOS*, *76*, F399, 1995.
- Ma, L., R. Crosson, and R. Ludwin, Western Washington earthquake focal mechanisms and their relationship to regional tectonic stress, in *Assessing earthquake hazards and reducing risk in the Pacific Northwest*, U. S. Geological Survey Professional Paper, pp. 257–83, U. S. Geological Survey, 1996.
- MacQueen, J. D., Linear inversion of gravity data with geological and geophysical constraints, Ph.D. thesis, University of Washington, Seattle, 1982.
- Malone, S. D., and S. S. Bor, Attenuation patterns in the Pacific Northwest based on intensity data and the location of the 1872 North Cascades earthquake, *Bull. Seis. Soc. Am.*, *69*(2), 531–546, 1979.
- McBirney, A., Volcanic evolution of the Cascade Range, *Annu. Rev. Earth Planet. Sci.*, *6*, 437–456, 1978.
- Miller, K. M., G. R. Keller, J. M. Gridley, J. Luetgert, W. Mooney, and H. Thybo, Crustal structure along the west flank of the Cascades, western Washington, *J. Geophys. Res.*, 1998, In Press.

- Moore, J. C., T. Byrne, P. W. Plumley, M. Reid, H. Gibbons, and R. S. Coe, Paleogene evolution for the Kodiak Islands, Alaska; Consequences of ridge-trench interaction in a more southerly latitude, *Tectonics*, *2*, 265–293, 1983.
- Moran, S. C., P-wave tomography at Mount Rainier, Washington: preliminary results, *EOS*, *76*, F644, 1995, (abstract).
- Moran, S. C., J. M. Lees, and S. D. Malone, Three-dimensional P-wave velocity structure in Southwestern Washington from local earthquake tomography, *EOS*, *77*(46), F466, 1996.
- Nelson, G. D., and J. E. Vidale, Earthquake locations by 3-D finite difference travel times, *Bull. Seis. Soc. Am.*, *80*, 395–410, 1990.
- Neumann, F., Crustal structure in the Puget Sound area, *Bur. Cent. Seis. Inter.*, *20*, 153–67, 1957.
- Officer, C. B., *Introduction to Theoretical Geophysics*, Springer-Verlag, 1974.
- Paige, C. C., and M. A. Saunders, LSQR: An algorithm for sparse linear equations and sparse least squares, *ACM Trans. on Math. Soft.*, *8*(1), 43–71, 1982.
- Parker, R. L., *Geophysical Inverse Theory*, Princeton series in geophysics, Princeton University Press, 41 William Street, Princeton, New Jersey 08540, 1994.
- Parsons, T., et al., A new view in the Cascadia subduction zone and volcanic arc: Implications for earthquake hazards along the Washington margin, *Geology*, *26*(3), 199–202, 1998.
- Parsons, T., J. Luetgert, A. Trehu, K. Miller, and U. ten Brink, A crustal velocity model of the Cascadia Subduction Margin southwest Washington, USA, from onshore-offshore seismic data, *EOS*, *77*(46), F453, 1996.

- Pratt, T. L., S. Johnson, C. Potter, W. Stephenson, and C. Finn, Seismic reflection images beneath Puget Sound, western Washington State: The Puget Lowland thrust sheet hypothesis, *J. Geophys. Res.*, 102(B12), 27,469–89, 1997.
- Press, W. H., B. P. Flannery, S. A. Teukolsky, and W. T. Vetterling, *Numerical Recipes: The art of scientific computing*, Cambridge University Press, 1986.
- Riddihough, R., Recent movements of the Juan de Fuca plate system, *J. Geophys. Res.*, 89(B8), 6980–6994, 1984.
- Satake, K., Fault parameters, coseismic deformation and tsunami heights from the January 1700 Cascadia earthquake (abstract), *EOS*, 77(46), 520, 1996.
- Schultz, A. P., and R. S. Crosson, Seismic velocity structure across the central Washington cascade range from refraction interpretation with earthquake sources, *J. Geophys. Res.*, 101(B12), 27899–915, 1996.
- Schuster, J. E., Geologic Map of Washington, Tech. rep., Washington Div. Geol. Earth Res., 1992.
- Sherrod, B., Personal Communication, 1998.
- Simpson, R. W., and A. V. Cox, Paleomagnetic evidence for tectonic rotation of the Oregon Coast Range, *Geology*, 5, 585–589, 1977.
- Snavely, P. D., and E. M. Baldwin, Siletz River volcanic series, Northwestern Oregon, *AAPG Bull.*, 32, 806–812, 1948.
- Snavely, P. D., N. S. MacLeod, and H. C. Wagner, Tholeiitic and alkalic basalts of the Eocene Siletz River volcanics, Oregon Coast Range, *American Journal of Science*, 266, 387–424, 1968.
- Spakman, W., and G. Nolet, Imaging algorithms, accuracy and resolution in delay time tomography, in *Mathematical Geophysics*, edited by N. J. Vlaar, G. Nolet,

M. J. R. Wortel, and S. A. P. L. Cloetingh, pp. 155–187, D. Reidel Publishing Company, 1988.

Spence, C. D., R. M. Clowes, and R. M. Ellis, Seismic structure across the active subduction zone of Western Canada, *J. Geophys. Res.*, *90*(B8), 6754–6772, 1985.

Stanley, D., Personal Communication, 1996.

Stanley, W., Tectonic study of the Cascade Range and Columbia Plateau in Washington State based upon magnetotelluric soundings, *J. Geophys. Res.*, *89*, 4447–4460, 1984.

Stanley, W., W. Gwilliam, G. Latham, and K. Westhusing, The southern Washington Cascades conductor - a previously unrecognized thick sedimentary sequence, *Am. Assoc. Petrol. Geol. Bull.*, *76*, 1569–1585, 1992.

Symons, N. P., and R. S. Crosson, Construction of a 3-D velocity model from heterogeneous data (abstract), *EOS*, *76*, F402, 1995a.

Symons, N. P., and R. S. Crosson, Relocation of earthquakes in the Puget lowland thrust sheet (abstract), *Seis. Res. Lett.*, *66*, 47, 1995b.

Symons, N. P., and R. S. Crosson, Seismic velocity structure of the Puget Sound region from 3-D non-linear tomography, *Geophys. Res. Lett.*, *24*(21), 2593–6, 1997.

Tabor, J. J., A tertiary accreted terrane: oceanic basalt and sedimentary rocks in the Olympic Mountains, Washington, in *Centennial Field Guide–Cordilleran Sec.*, pp. 377–382, Geological Society of America, 1987.

Tabor, J. J., and B. T. R. Lewis, Crustal structure of the Washington continental margin from refraction data, *Bull. Seis. Soc. Am.*, *76*(4), 1011–1024, 1986.

- Tabor, R. W., Late Mesozoic and possible early Tertiary accretion in western Washington state—The Helena-Haystack melange and the Darrington-Devils Mountain fault zone, *Geol. Soc. Am. Bull.*, 106, 217–232, 1994.
- Tabor, R. W., and W. M. Cady, The structure of the Olympic Mountains, Washington - analysis of a subduction zone, Prof. Paper 1033, U.S. Geological Survey, 1978.
- Thomas, G. C., R. S. Crosson, B. Cohee, T. Qamar, and P. Lombard, The May 2, 1996, Duvall, Washington earthquake and aftershock sequence, *EOS*, 77(46), 523, 1996.
- Thorsen, G. W., The Puget Lowland earthquakes of 1949 and 1965, *Washington State Department of Natural Resources, Information Circular*, 81, 1986.
- Trehu, A. M., I. Asudeh, T. M. Brocher, J. H. Luetgert, W. D. Mooney, J. L. Nabelek, and Y. Nakamura, Crustal architecture of the Cascadia forearc, *Science*, 266, 237–242, 1994.
- Um, J., and C. H. Thurber, A fast algorithm for two-point seismic ray tracing, *Bull. Seis. Soc. Am.*, 77, 972–986, 1987.
- Vidale, J., Finite-difference calculation of traveltimes, *Bull. Seis. Soc. Am.*, 78, 2062–2076, 1988.
- Vidale, J., Finite-difference calculation of traveltimes in three dimensions, *Geophysics*, 55, 521–526, 1990.
- Villasenor, A., Personal Communication, 1996.
- Walsh, T. J., Geologic Map of Washington - Southwest Quadrant, Washington Division of Geology and Earth Resources, 1987, Geologic Map GM-34.
- Wang, K., Simplified analysis of horizontal stresses in a buttressed forearc sliver at an oblique subduction zone, *Geophys. Res. Lett.*, 23(16), 2021–2024, 1996.

Wells, R. E., C. S. Weaver, and R. J. Blakely, Fore-arc migration in Cascadia and its neotectonic significance, *Geology*, 26(8), 759–762, 1998.

Appendix A

FINITE-DIFFERENCE TRAVEL-TIME CALCULATIONS

All travel-times used in this document have been calculated with a class of finite-difference travel-time calculators (FDTT) described in *Vidale* [1988, 1990]. The method works by solving the eikonal equation on an expanding box of nodes surrounding the source, when the box has expanded to fill the entire region the problems is complete. The actual code used for this work was corrected and extended by *Hole* [1992]; *Hole and Zelt* [1995]. This solver has the advantages of being fast and accurate, there are also no problems with shadow zones or accidental calculation of second (instead of first) arrivals in complex media.

The following explanation of the eikonal equation closely follows *Officer* [1974]. We start with the 3-D wave equation in Cartesian coordinates

$$c^2 \left(\frac{\partial^2 \Psi}{\partial x^2} + \frac{\partial^2 \Psi}{\partial y^2} + \frac{\partial^2 \Psi}{\partial z^2} \right) = \frac{\partial^2 \Psi}{\partial t^2} \quad (\text{A.1})$$

By inspection the solution of equation A.1 is

$$\Psi = f(\mathbf{k} \cdot \mathbf{x} - ct) \quad (\text{A.2})$$

Then the equation of characteristics of equation A.1 is

$$\left(\frac{\partial \Psi}{\partial x} \right)^2 + \left(\frac{\partial \Psi}{\partial y} \right)^2 + \left(\frac{\partial \Psi}{\partial z} \right)^2 = \frac{1}{c^2} \left(\frac{\partial \Psi}{\partial t} \right)^2 \quad (\text{A.3})$$

and equation A.2 also solves this equation. Now if c is not constant then \mathbf{k} will change and so we replace the argument of equation A.2 with the more general equation

$$\Psi = f[W(x, y, z) - c_0 t] \quad (\text{A.4})$$

where c_0 is a constant reference velocity. Substituting equation A.4 into equation A.3 we obtain the eikonal equation

$$\left(\frac{\partial W}{\partial x}\right)^2 + \left(\frac{\partial W}{\partial y}\right)^2 + \left(\frac{\partial W}{\partial z}\right)^2 = \left(\frac{c_0}{c}\right)^2 \quad (\text{A.5})$$

We first define the function $T(\eta, \xi)$ as the travel-time from a seismic source at position η to a receiver at position ξ . For a given source this defines the 2D scalar function $T(\xi)$. Now, by definition the gradient is the value of the change in dependent variable for change in independent variable so

$$\nabla T(\xi) = \frac{\partial t}{\partial \mathbf{l}} \quad (\text{A.6})$$

where \mathbf{l} is the length vector, and $\frac{\partial t}{\partial \mathbf{l}}$ is just time per distance or the slowness. This can be changed from a vector relation into an easier to use scalar form by squaring

$$\nabla T(\xi) \cdot \nabla T(\xi) = \frac{\partial t}{\partial \mathbf{l}} \cdot \frac{\partial t}{\partial \mathbf{l}} \quad (\text{A.7})$$

or simplifying

$$\left(\frac{\partial T(\xi)}{\partial x}\right)^2 + \left(\frac{\partial T(\xi)}{\partial y}\right)^2 = \left(\frac{1}{c^2}\right) \quad (\text{A.8})$$

An Illustration using Huygen's principle: a wave propagates as if every point on the wave surface is a secondary source, at a later time the wave will be the envelope of wavelets from the initial wave (figure A.1). Consider the function $W(\eta)$ defining the family of wavefronts from a given source. Then a wavefront at time t_0 is made up of the locus of points $W(\eta) = A + c_0 t_0$ (A and c_0 constants) and $W(\eta) - c_0 t_0 = A$ defines a wavefront with a given phase. Consider the wavelet from the point η where the velocity is c at a time $t = t_0 + dt$

$$W(\eta) - c_0 t_0 = W(\eta + c dt \hat{\mathbf{n}}) - c_0(t_0 + dt) \quad (\text{A.9})$$

where $\hat{\mathbf{n}}$ is the unit normal to the wavefront. If dt is small then

$$W(\eta) - c_0 t_0 = W(\eta) + c dt \hat{\mathbf{n}} \cdot \nabla W(\eta) - c_0(t_0 + dt) \quad (\text{A.10})$$

to first order and

$$\hat{\mathbf{n}} \cdot \nabla W(\eta) = \frac{c_0}{c} \quad (\text{A.11})$$

Now the gradient of W must be parallel to the normal to the wavefront, so, for some constant B

$$B\hat{\mathbf{n}} = \nabla W(\eta) \quad (\text{A.12})$$

If we pre-multiply by $\hat{\mathbf{n}}$ then

$$\hat{\mathbf{n}} \cdot B\hat{\mathbf{n}} = \hat{\mathbf{n}} \cdot \nabla W(\eta) \quad (\text{A.13})$$

And using equation A.11

$$B = \frac{c_0}{c} \quad (\text{A.14})$$

Substituting back into equation A.12 and solving we get

$$\hat{\mathbf{n}} = \frac{c}{c_0} \nabla W(\eta) \quad (\text{A.15})$$

Now substituting for $\hat{\mathbf{n}}$ in equation A.11

$$\frac{c}{c_0} \nabla W(\eta) \cdot \nabla W(\eta) = \frac{c_0}{c} \quad (\text{A.16})$$

Multiplying by $\frac{c_0}{c}$ yields the eikonal equation.

The first step is the discretization of the volume into a set of cubes, the slowness is specified at nodes which make up the corners of the cubes. The algorithm is initialized by finding the travel-time from the source to the corners of the box containing the source. This box is then iteratively expanded until it fills the entire volume. In 2-D, expansion of the box starts from the relative minimum time on each of the four sides (figure A.2). The time is then calculated from node t_0 to node t_3 using a non-centered finite-difference equation

$$\begin{aligned} \frac{\partial t}{\partial x} &\cong \frac{1}{h}(t_0 - t_3) \\ \frac{\partial t}{\partial z} &\cong \frac{1}{2h}(t_1 - t_2) \end{aligned} \quad (\text{A.17})$$

where h is the node spacing and t_0 , t_1 , and, t_2 are already known. Substituting into the 2-D eikonal equation (equation A.8) and solving for t_3

$$t_3 = t_0 + \frac{\sqrt{4h^2s^2 - t_1^2 + 2t_1t_2 - t_2^2}}{2} \quad (\text{A.18})$$

where s is the slowness in this cell (average of the nodal slownesses). Now the time to node t_4 is calculated using a centered finite-difference equation

$$\begin{aligned} \frac{\partial t}{\partial x} &\cong \frac{1}{2h}(t_0 + t_1 - t_3 - t_4) \\ \frac{\partial t}{\partial z} &\cong \frac{1}{2h}(t_0 + t_3 - t_1 - t_4) \end{aligned} \quad (\text{A.19})$$

and again solving equation A.8, in this case

$$t_4 = t_0 + \sqrt{2h^2s^2 - t_1^2 + 2t_1t_3 - t_3^2} \quad (\text{A.20})$$

Extension to 3-D is simple, there are of course more cases to consider but the methodology is the same. Instead of the four sides of a square, the box expands on the six sides of a cube.

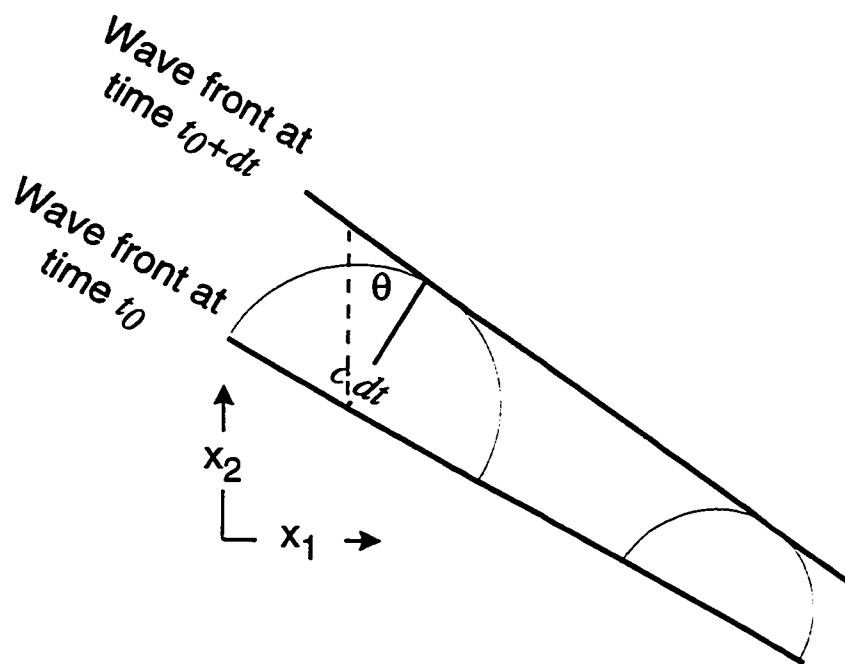


Figure A.1: According to Huygen's principle the wavefront at time $t_0 + dt$ is made of the locus of circles with radius $c dt$ from all points on the wavefront at time t_0 .

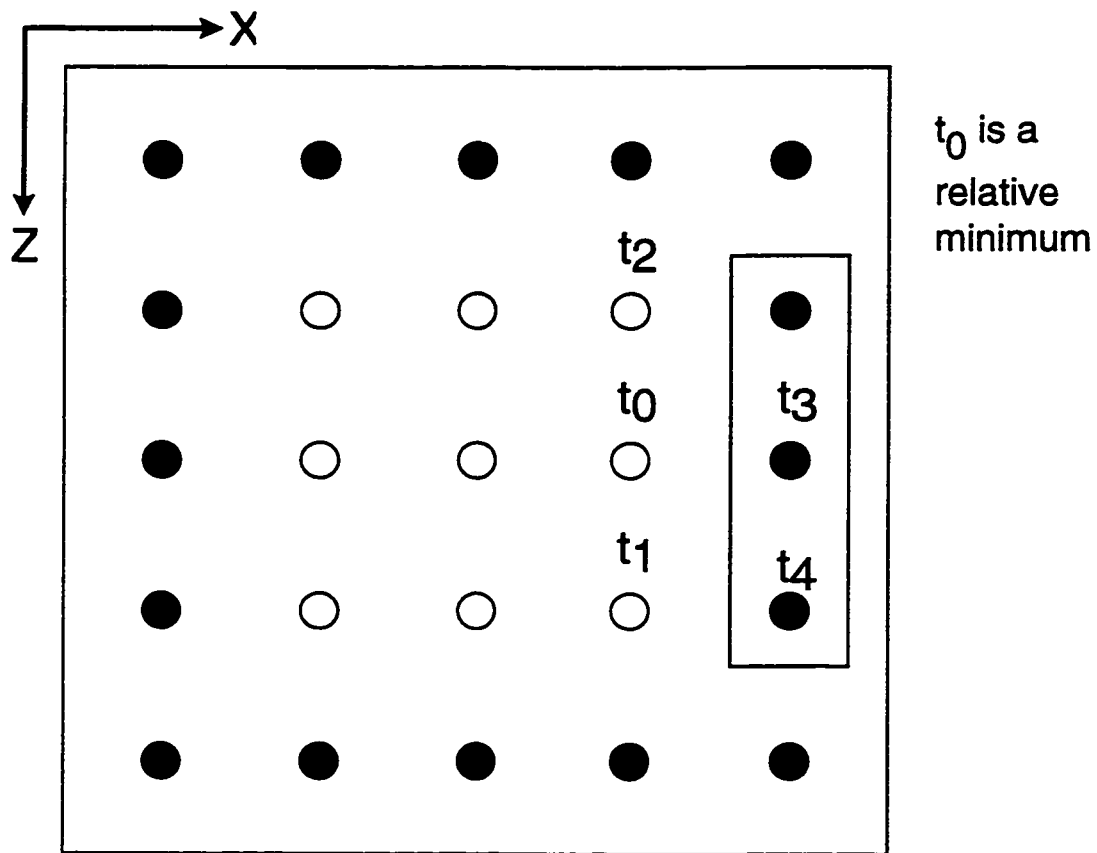


Figure A.2: The expansion of the box begins from the relative time minimum at node t_0 to node t_3 .

Appendix B

PSEUDO-CODE FOR NON-LINEAR SEISMIC TOMOGRAPHY USING FINITE-DIFFERENCE TRAVEL-TIMES

Table B.1: Seismic Tomography Pseudo-code

```
Read in the starting model  $\mathbf{m}^{(0)}$ 
Generate the regularization matrix,  $\mathbf{L}$ ;  $\mathbf{b} = \mathbf{L}\mathbf{m}^{(0)}$ 
 $N_{model}^{(0)} = \|\mathbf{b}\|^2$ 
Calculate travel-times
Locate earthquakes using Grid Search
Refine earthquake locations using Geiger's method and interpolated travel-times
Generate the residual vector,  $\mathbf{r}$ ;  $N_{ray}^{(0)} = \|\mathbf{r}\|^2$ 
Start main loop
  Generate the  $\mathbf{J}$  matrix by back tracing the travel-times
  Create the full matrix  $\mathbf{A} = \begin{bmatrix} \mathbf{W}\mathbf{J} \\ \lambda\mathbf{L} \end{bmatrix}$ 
  Use CGLS to find a solution to  $\mathbf{A}\delta\mathbf{m} = \begin{bmatrix} \mathbf{W}\mathbf{r} \\ -\mathbf{b} \end{bmatrix}$ 
  If  $\|\delta\mathbf{m}\|^2 < \text{tolerance}$  then exit main loop
  Start inner loop;  $\mu = 1$ 
     $\mathbf{m}_i = \mathbf{m}_{i-1} + \mu\delta\mathbf{m}$ 
     $\mathbf{b} = \mathbf{L}\mathbf{m}_i$ ;  $N_{model}^{(i)} = \|\mathbf{b}\|^2$ 
    Calculate travel-times and residual vector,  $\mathbf{r}$ 
     $N_{ray}^{(i)} = \|\mathbf{r}_i\|^2$ 
    If  $\lambda N_{model}^{(i)} + N_{ray}^{(i)} < \lambda N_{model}^{(i-1)} + N_{ray}^{(i-1)}$ 
      then exit inner loop
    else  $\mu = \frac{\mu}{2}$ 
  End inner loop
End main loop
```

Appendix C

PUGET LOWLAND SEISMOGRAPH STATIONS

Table C.1: Puget Lowland Seismograph Stations

Name	Inst. Date	Abbreviation	Lat.	Lon.	Elev. (km)
Ape Cave	–	APW	46N39.4667	122W39.4050	0.457
Ashford	3/95	ASF	46N45.6030	122W 1.5930	0.528
Boisfort Mt 1	10/72	BFW	46N29.2000	123W12.8900	0.902
Bald Hill	7/84	BHW	47N50.2100	122W 1.9300	0.198
Blyn Mt.	7/70	BLN	48N 0.4417	122W58.3107	0.585
Lake Shannon	12/84	BLS	48N34.3500	121W40.0000	1.341
Boistfort Mt. 2	11/80	BOW	46N28.5000	123W13.6833	0.870
Crazy Man Mt.	4/80	CMM	46N26.1167	122W30.3500	0.620
Cultus Mt.	6/86	CMW	48N25.4217	122W 7.1400	1.190
Cowlitz River	3/80	COW	46N29.4600	122W 0.7267	0.305
Capitol Peak	7/70	CPW	46N58.4300	123W 8.1800	0.792
Dalles Ridge	4/95	DLR	47N 6.1688	121W34.0450	1.190
Elk Rock	5/80	ELK	46N18.3333	122W20.4500	1.270
Frog Mountain	5/95	FGM	47N 4.5480	121W45.7595	1.158
Mt. Fremont	9/72	FMW	46N56.4933	121W40.1883	1.859
Garrison Hill	9/75	GHW	47N 2.5000	122W16.3500	0.268
Glacier Lake	–	GLK	46N33.8367	121W36.5117	1.320
Gold Mt.	2/70	GMW	47N32.8750	122W47.1800	0.506
Green Mountain	3/95	GNW	47N33.8640	122W49.5173	0.165
Grass Mt.	6/70	GSM	47N12.1900	121W47.6700	1.305
Hoodsport	–	HDW	47N38.9100	123W 3.2533	1.006
Haystack Lookout	6/75	HTW	47N48.2083	121W46.1442	0.829
Jim Creek	12/82	JCW	48N11.7117	121W55.5178	0.792
Kosmos	05/81	KOS	46N27.6800	122W11.4300	0.828
Lucas Creek	3/92	LCW	46N40.2400	122W42.0467	0.396

<i>continued from previous page</i>					
Name	Inst. Date	Abreviation	Lat.	Lon.	Elev. (km)
Ladd Mt.	6/75	LMW	46N40.0900	122W17.4400	1.224
Longmire	3/88	LON	46N45.0000	121W48.6000	0.853
Lyman	4/75	LYW	48N32.1200	122W 6.1000	0.107
Mt. Baker	11/72	MBW	48N47.0400	121W53.9800	1.676
Mt. Constitution	11/72	MCW	48N40.7800	122W49.9400	0.693
McNeil Island	3/85	MEW	47N12.1103	122W38.7600	0.097
Mashel Creek	8/95	MHL	46N52.9428	122W 3.8405	1.215
Monroe	09/79	MOW	47N50.7817	122W 2.8817	0.180
Burnt Hill	7/80	OBH	47N19.5750	123W51.9500	0.383
Oak Harbor	5/75	OHW	48N19.4000	122W31.9100	0.054
Lake Quinault	7/80	OLQ	47N30.9683	123W48.5250	0.121
North River	7/80	ONR	46N52.6250	123W46.2750	0.257
Snow Dome	10/84	OSD	47N49.2500	123W42.1000	2.010
UW Pack Forest	2/95	PAK	46N50.4893	122W18.1830	0.436
GS Canada	-	PGC	48N38.9998	123W27.0295	0.005
Port Gamble	4/85	PGW	47N49.3133	122W35.9615	0.122
-	-	PIB	48N49.1000	123W19.1500	0.060
Randle	3/80	RAN	46N24.5000	121W51.8167	1.620
Camp Muir	9/93	RCM	46N50.1483	121W43.9067	3.085
Camp Schurman	6/27/89	RCS	46N52.2600	121W43.8660	2.877
Rattlesnake Mt.	8/85	RDT	47N27.5825	121W48.3200	1.024
Emerald Ridge	7/89	RER	46N49.1533	121W50.4550	1.756
Rattlesnake Mt.	7/71	RMW	47N27.5825	121W48.3200	1.024
Rockport	-	RPW	48N26.9000	121W30.8167	0.850
Shriner's Peak	6/95	RSH	46N48.7598	121W31.7162	1.770
Voight Creek	1/83	RVC	46N56.5750	121W58.2883	1.000
Ranney Well	5/95	RWW	46N57.8343	123W32.5980	0.015
Strawberry Look.	6/80	SBL	46N20.4200	122W 2.3300	1.665
Seattle	-	SEA	47N39.3000	122W18.5000	0.030
-	-	SEAE	47N42.0000	122W16.3000	0.000
South Mt.	3/75	SMW	47N19.1700	123W20.5000	0.840
GS Canada	-	SNB	48N46.5598	123W10.2718	0.408
Seward Park	9/69	SPW	47N33.2217	122W14.7517	0.008
Satsop	5/93	SSW	46N58.3400	123W26.0300	0.120
Striped Peak	6/73	STW	48N 9.0483	123W40.2183	0.308
Tradedollar Lake	11/83	TDL	46N21.0500	122W12.9500	1.400

<i>continued from previous page</i>					
Name	Inst. Date	Abbreviation	Lat.	Lon.	Elev. (km)
Tolt Res.	10/93	TTW	47N41.6777	121W41.3332	0.542
GS Canada	-	VGZ	48N24.8338	123W19.4637	0.067
Willame Creek	6/95	WCR	46N36.8477	121W45.9932	1.200
Bear River Ridge	12/93	WIB	46N20.5800	123W52.5100	0.503
White Pass	3/80	WPW	46N41.8900	121W32.8000	1.250
Crystal Mt.	10/95	XTL	46N55.7967	121W29.5967	1.665

VITA

Neill P. Symons

Address:

University of Washington

Geophysics, Box 351650

Seattle WA 98195-1650

Phone Number: (206) 685-1707

E-Mail Address: nsymons@geophys.washington.edu

Education:

Ph.D., Geophysics, University of Washington, Seattle WA; 1998

B.S., Geology, University of Washington, Seattle WA; 1993

B.S., Computer Science, University of Washington, Seattle WA; 1993

NOTE TO USERS

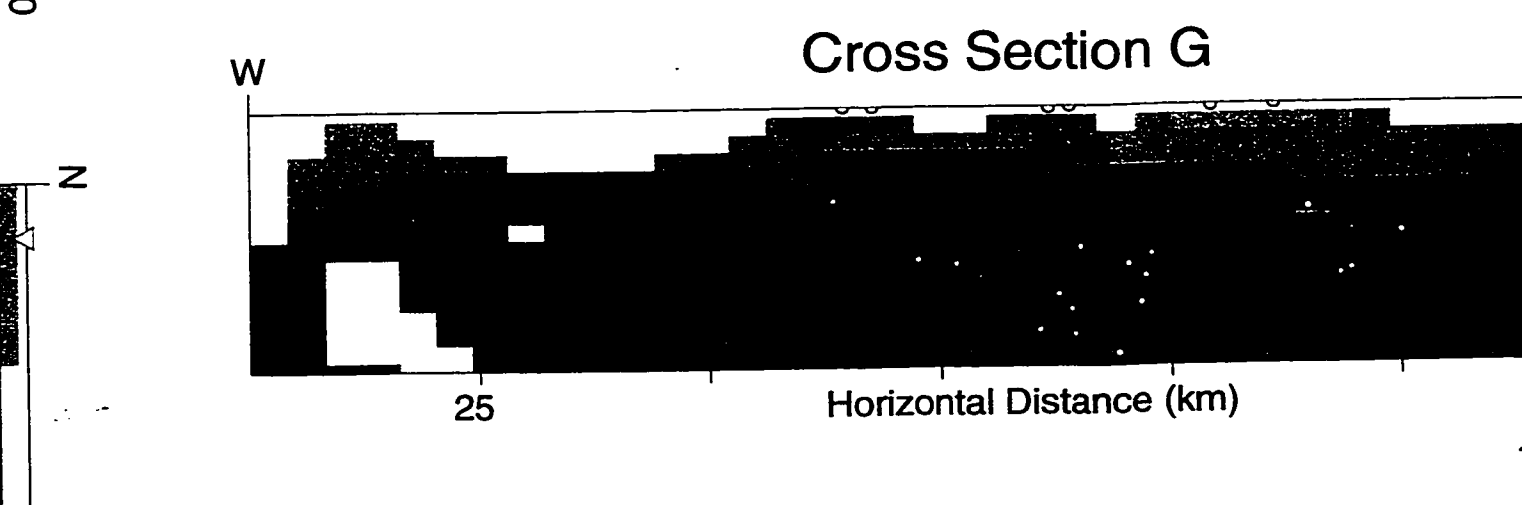
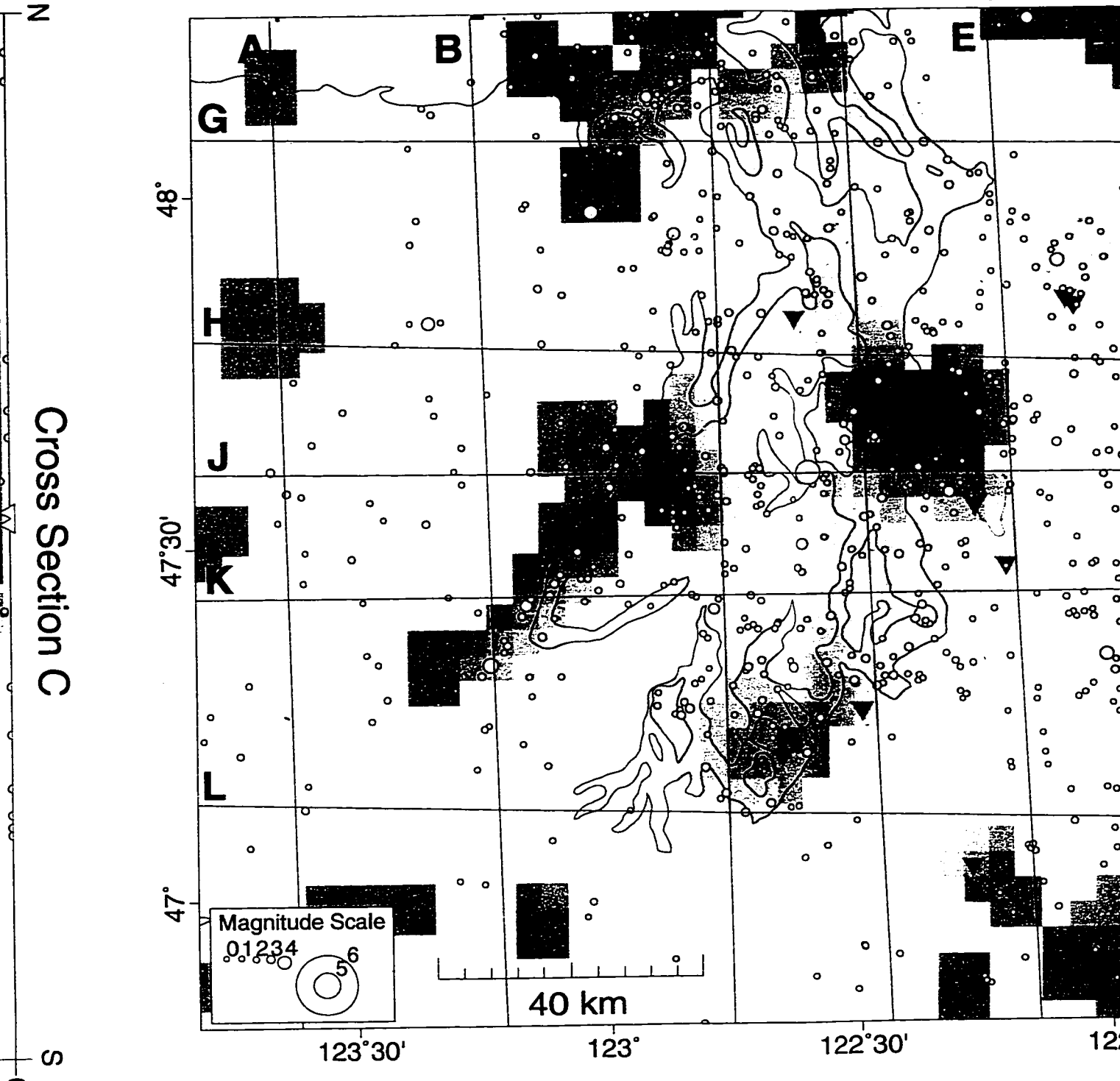
Oversize maps and charts are microfilmed in sections in the following manner:

LEFT TO RIGHT, TOP TO BOTTOM, WITH SMALL OVERLAPS

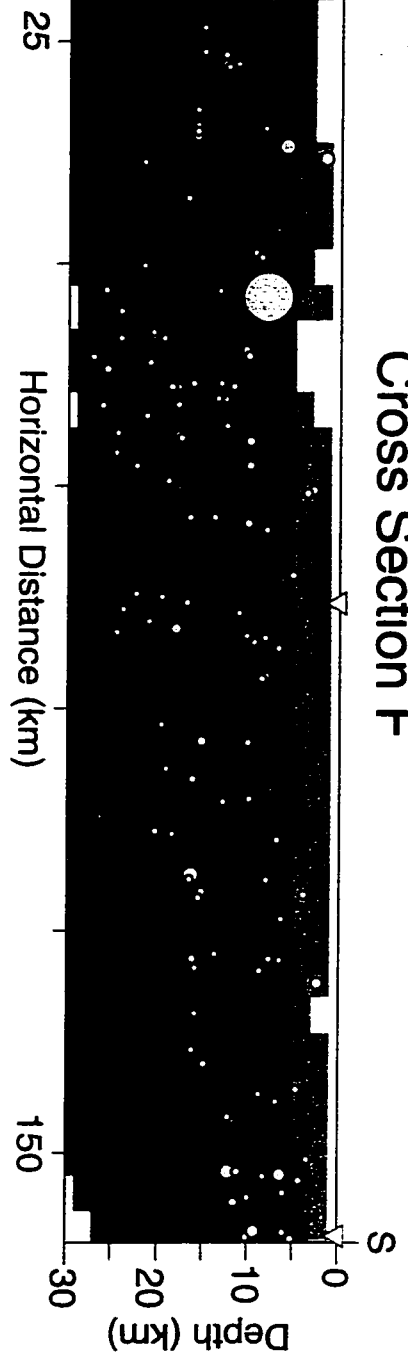
The following map or chart has been microfilmed in its entirety at the end of this manuscript (not available on microfiche). A xerographic reproduction has been provided for paper copies and is inserted into the inside of the back cover.

Black and white photographic prints (17"x 23") are available for an additional charge.

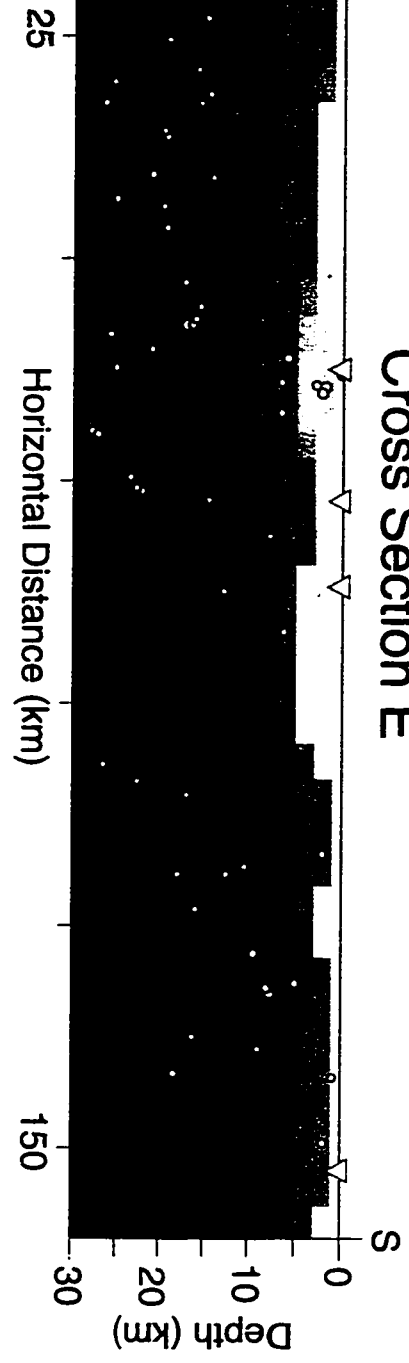
UMI



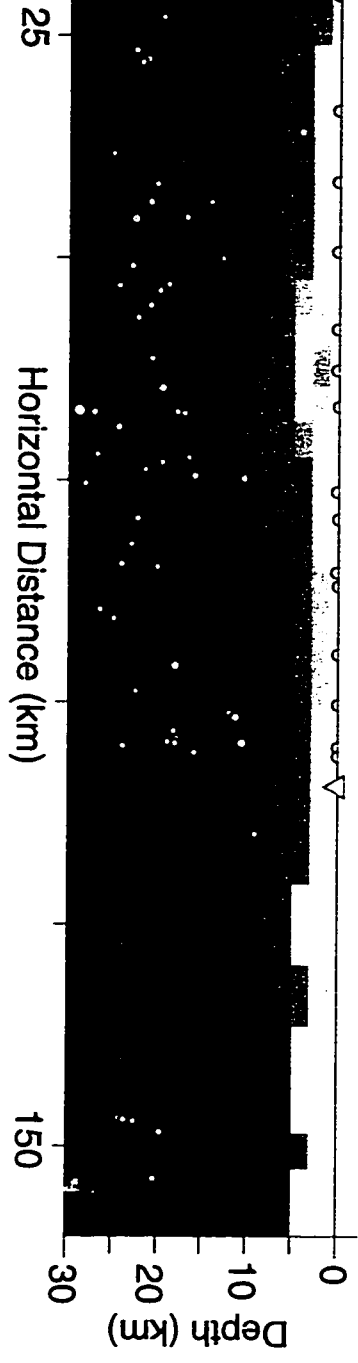
Cross Section F



Cross Section E



Cross Section D



2.5 4.2 5.8 7.5

P-Wave Velocity (km/sec)

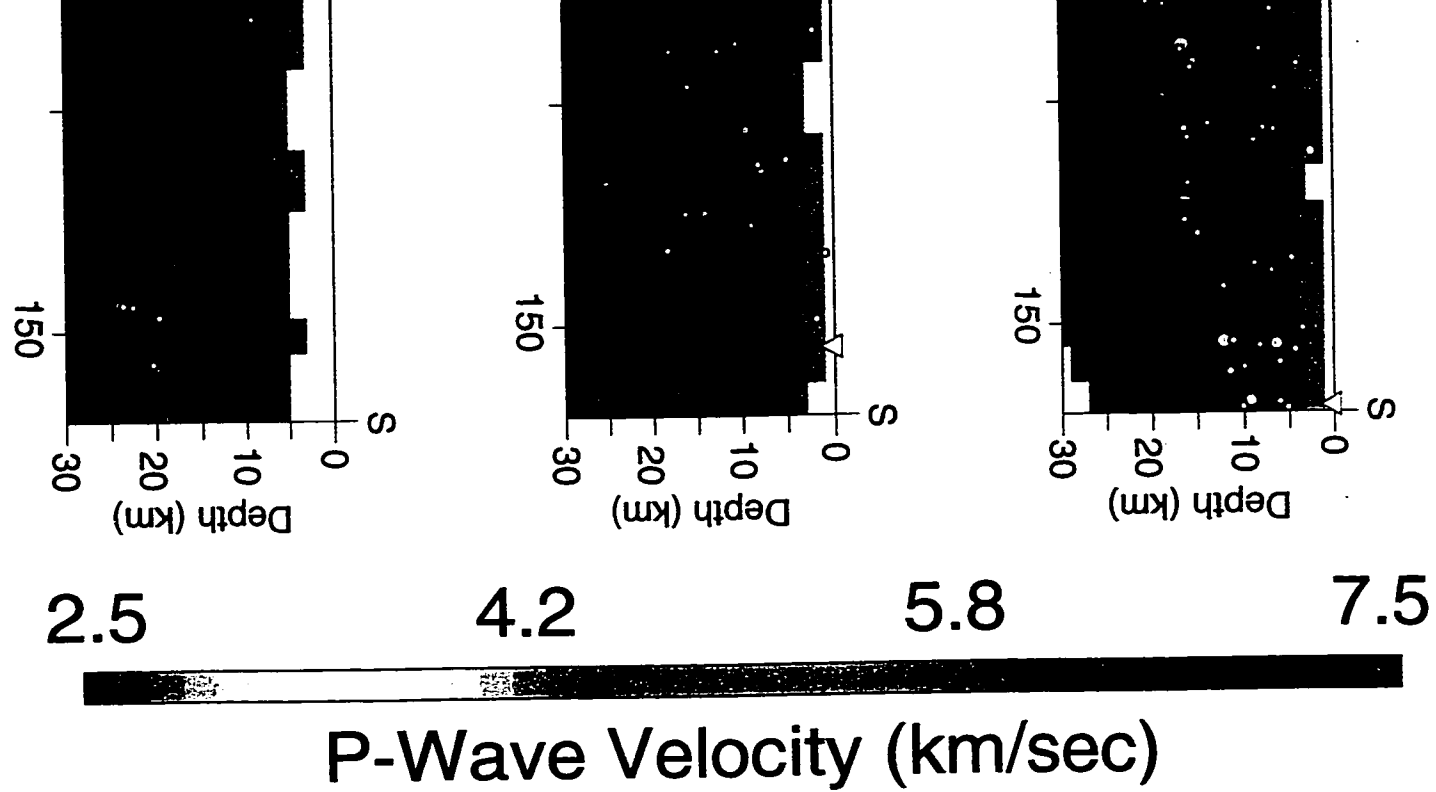
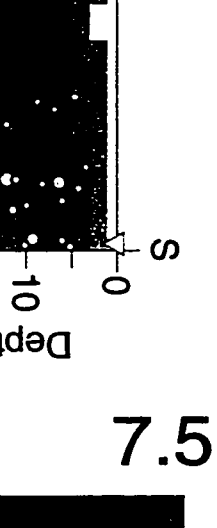
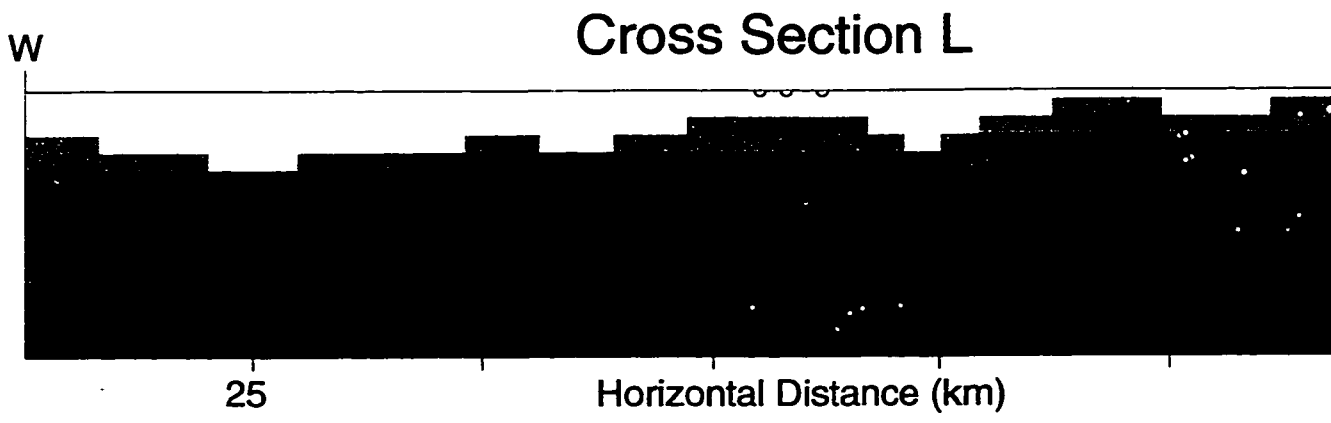
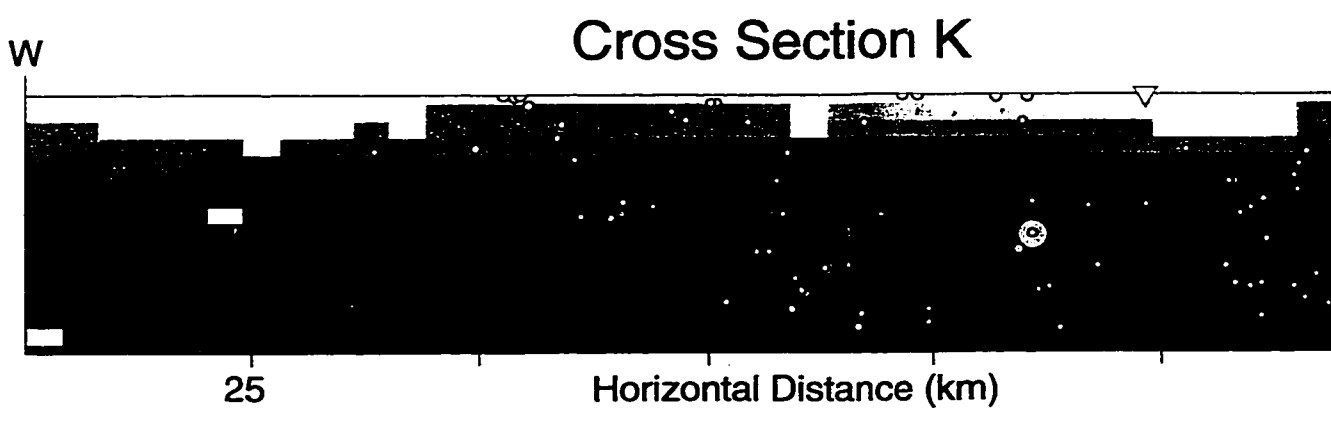


Plate 1: Seven maps and 11 cross sections through chapter 7. The data for this model consists of: 20 explosions from 1991 and 1995; and 56 stations. Data has been recorded at about 70 seismic stations in the Seismograph Network since 1980. Maps and cross sections

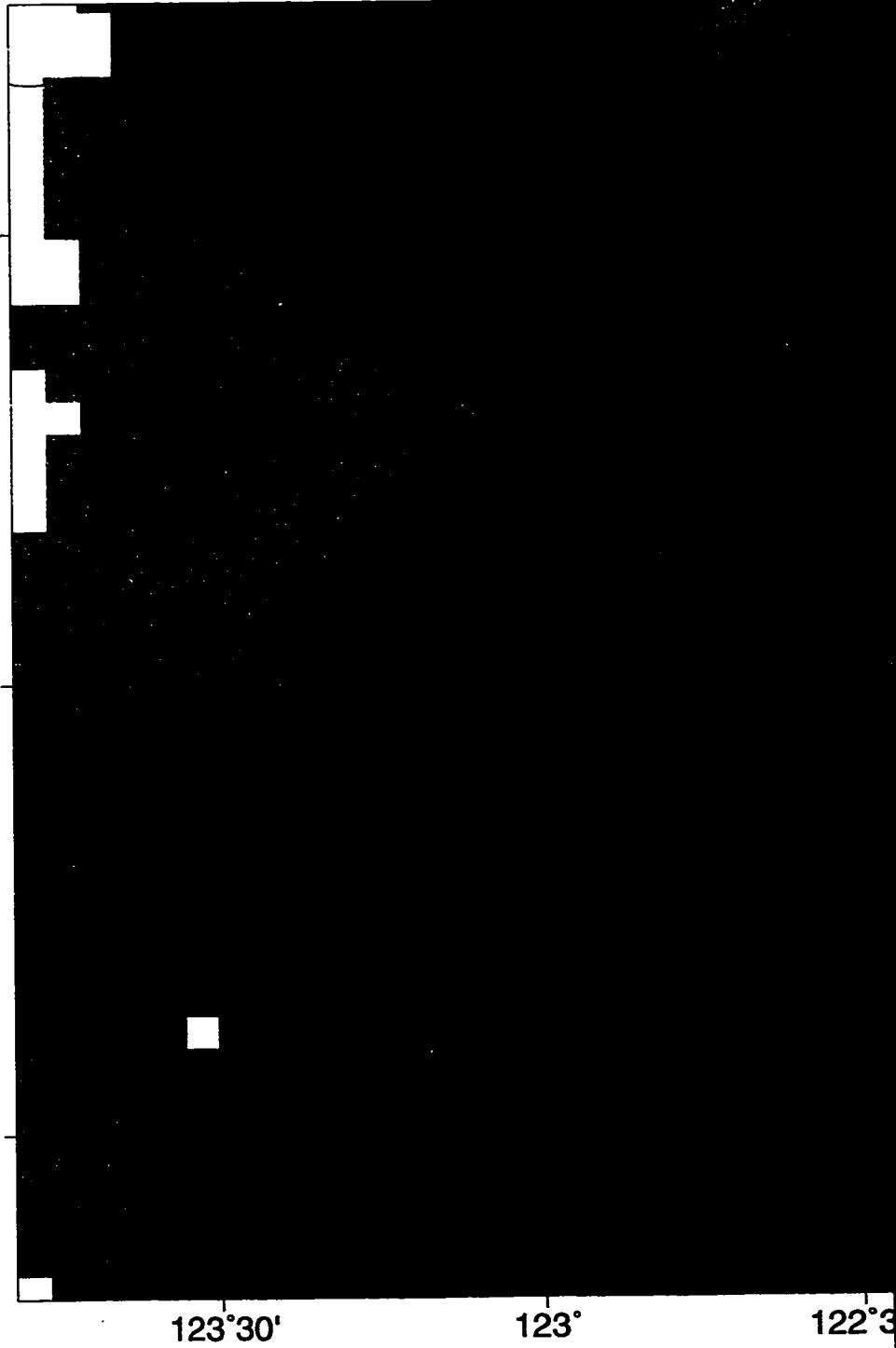
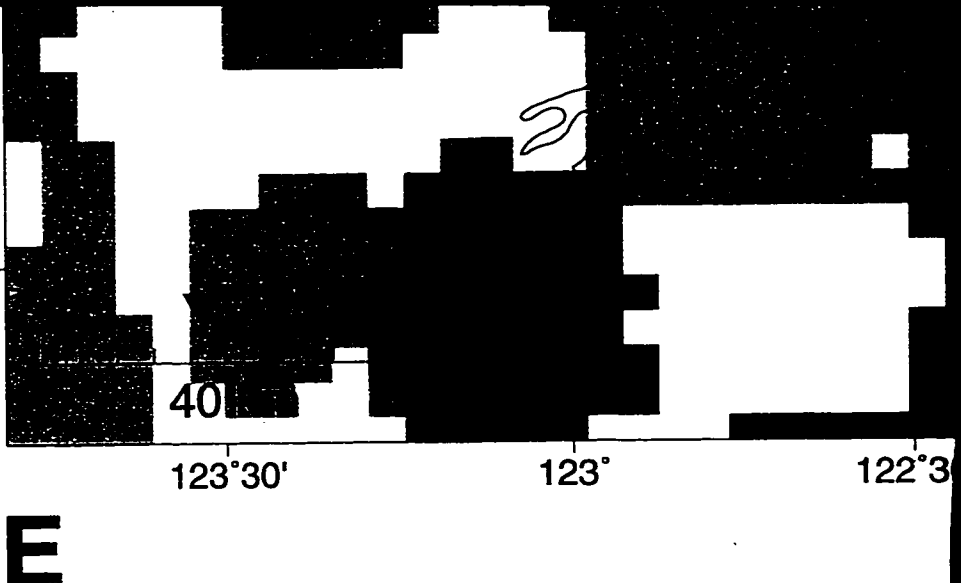
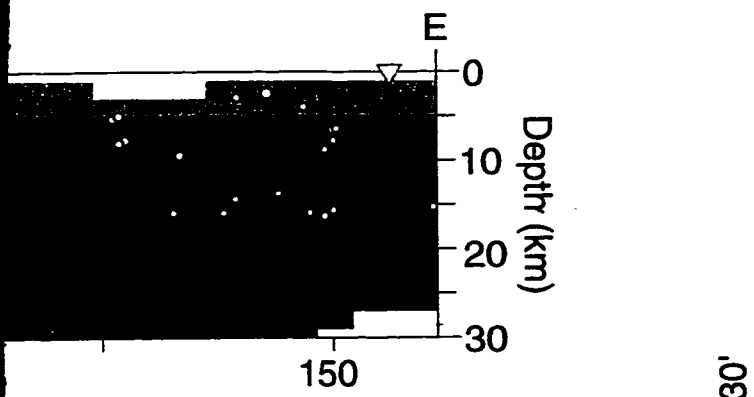
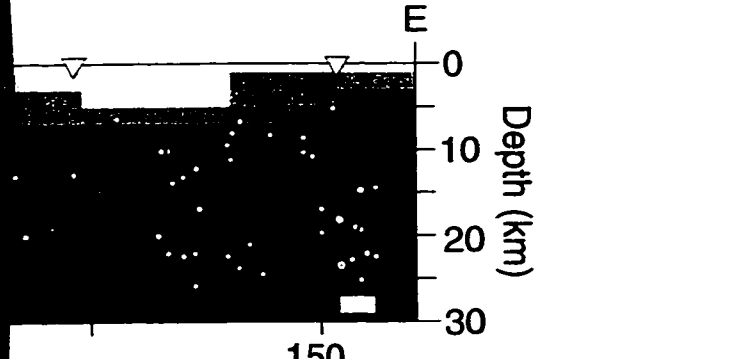
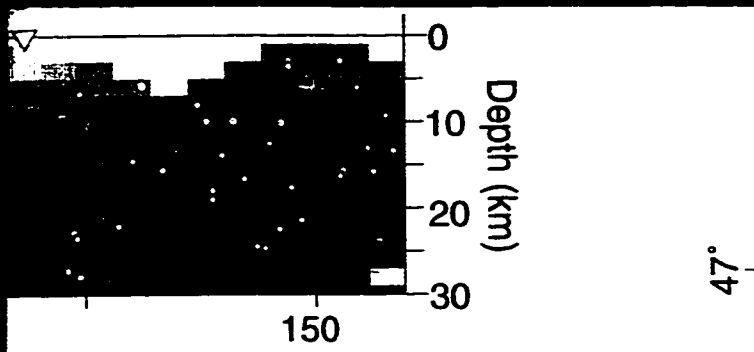


25

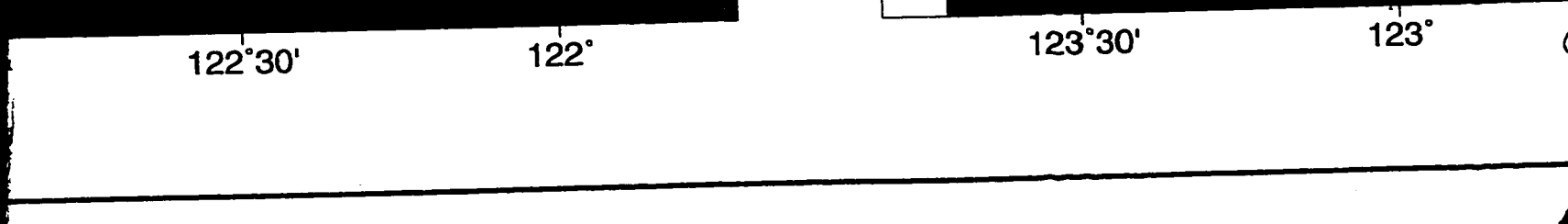
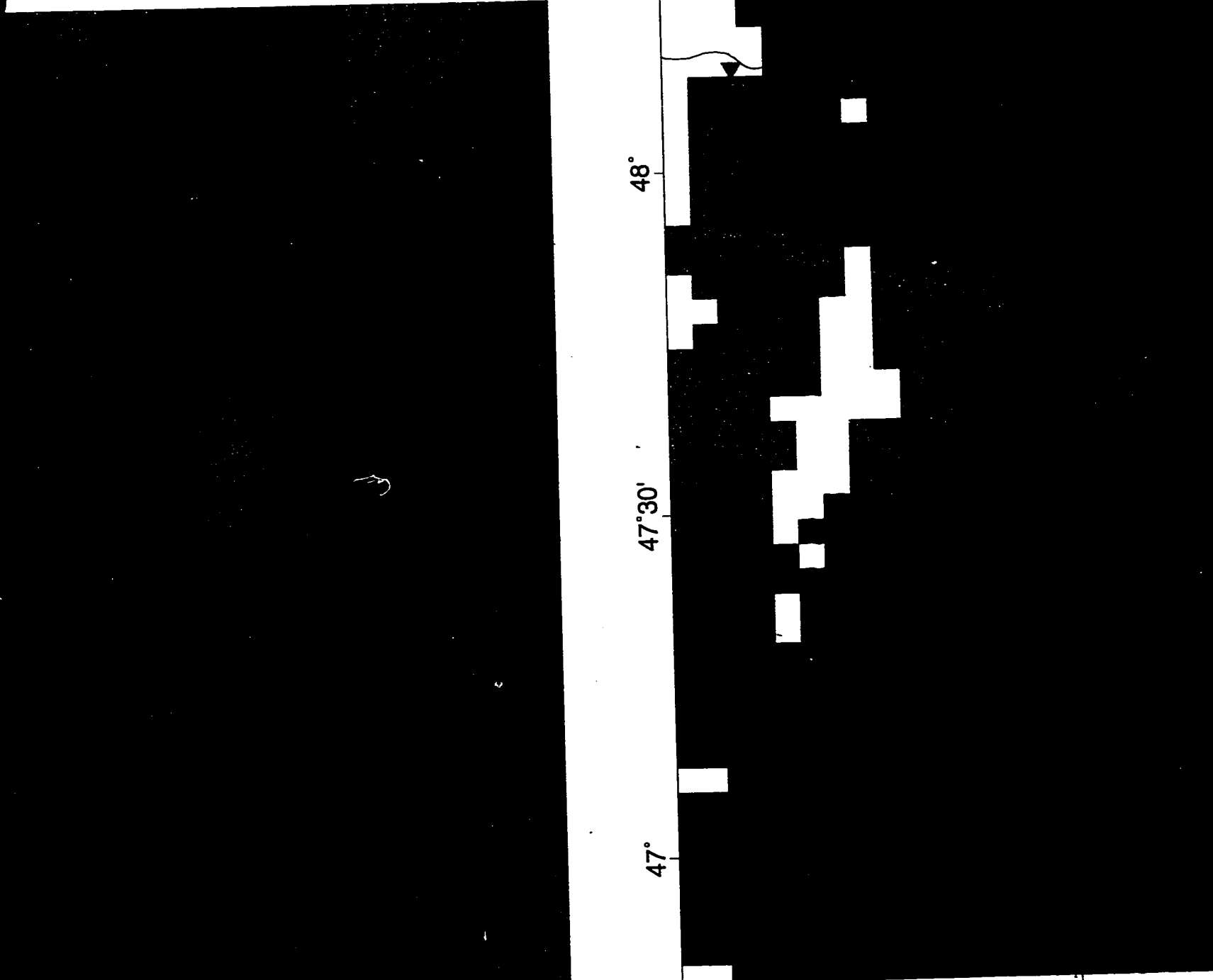
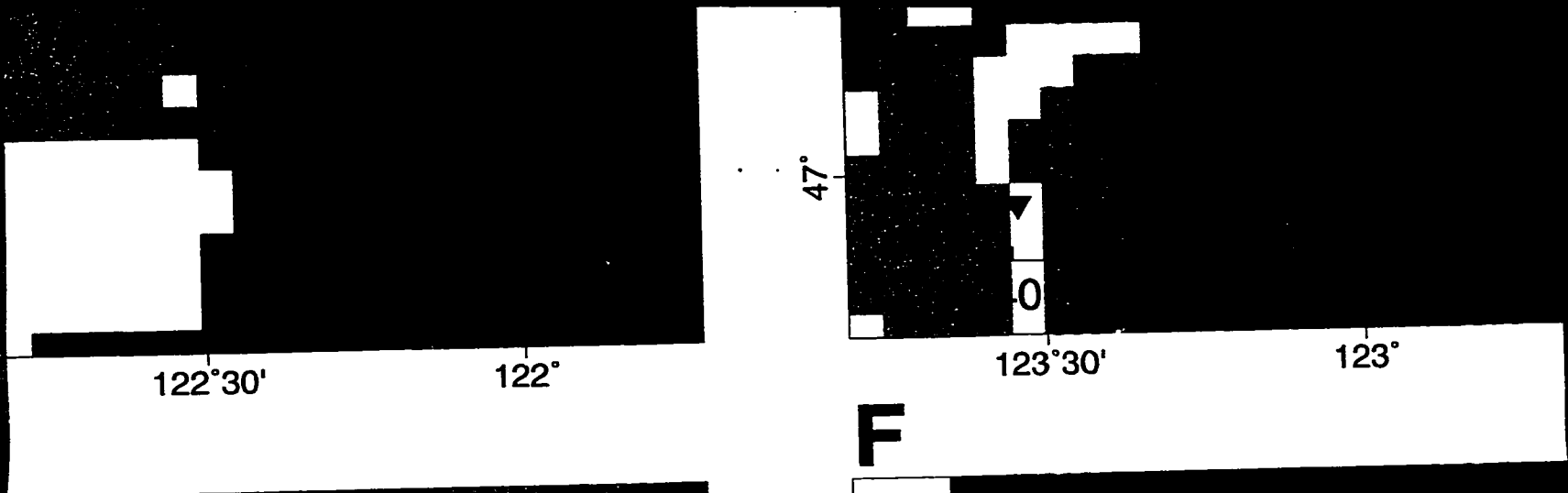
Horizontal Distance (km)



ctions through the 3-D velocity model discussed in
 consists of: 1004 earthquakes from the HQDS (Chap
 and 56 stacks from the SHIPS experiment (Chapt
 seismographs from the Pacific Northwest Seismo
 s sections created with Xmap8 (Lees, 95).



cussed in
 DS (Chapter 3);
 t (Chapter 6). The
 Seismograph



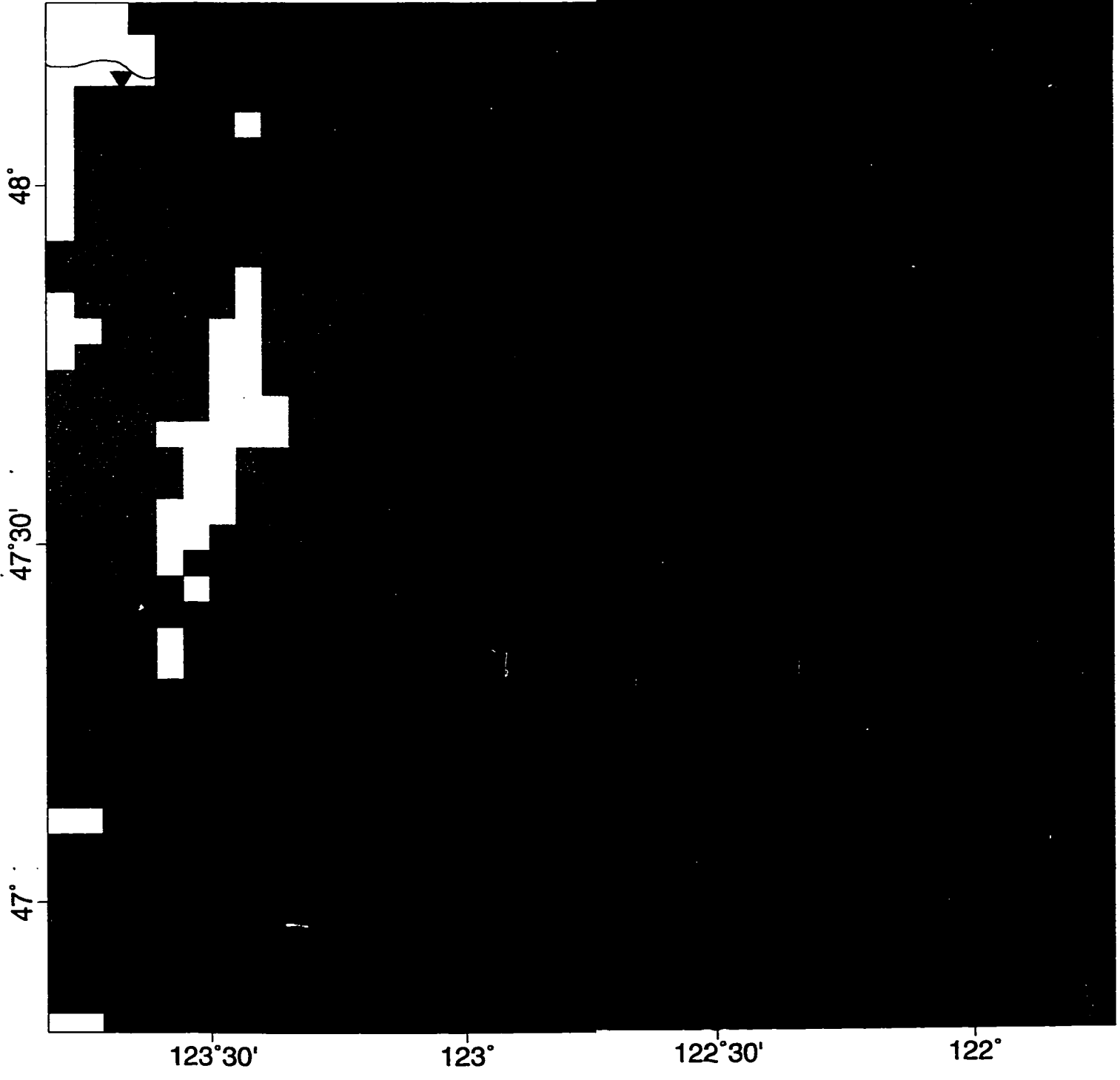
123°30'

123°

122°30'

122°

F



48°

47°30'

47°

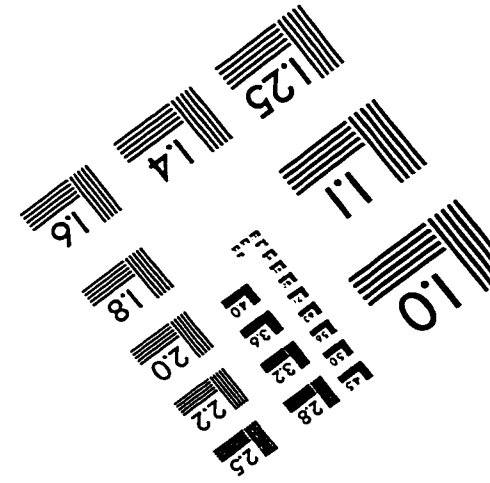
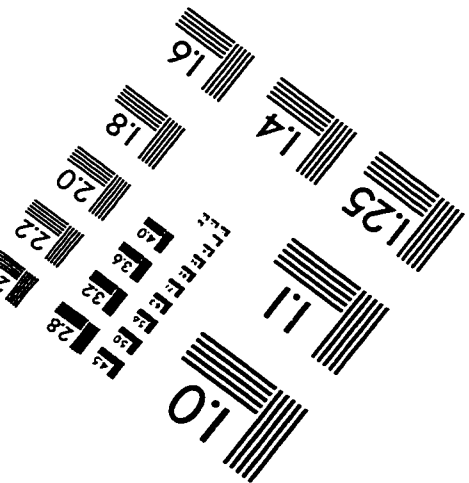
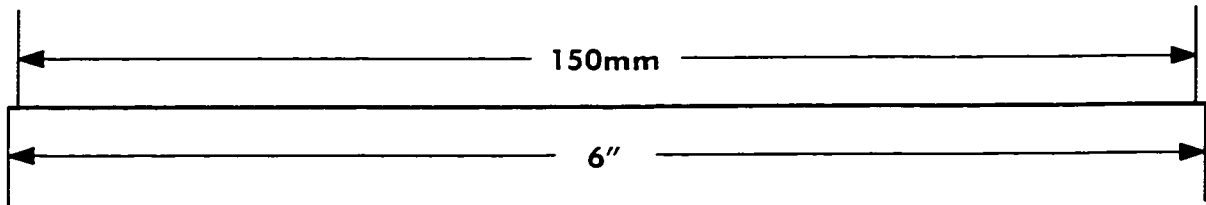
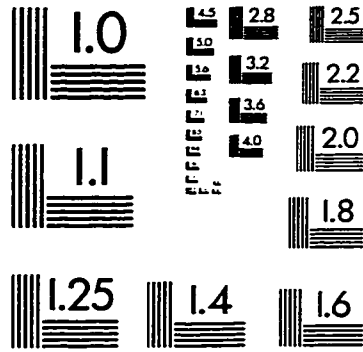
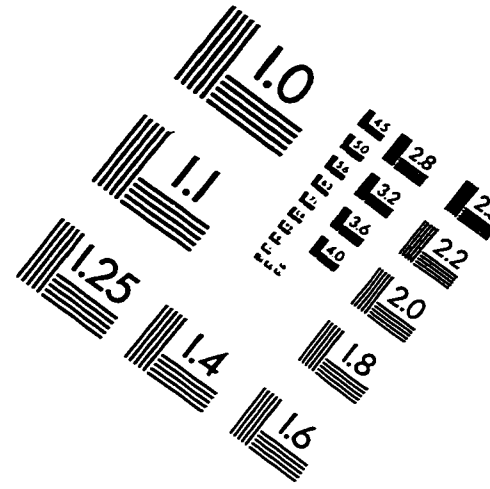
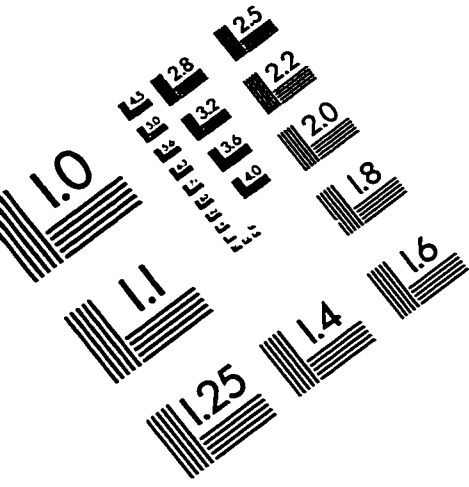
123°30'

123°

122°30'

122°

IMAGE EVALUATION TEST TARGET (QA-3)



APPLIED IMAGE, Inc
1653 East Main Street
Rochester, NY 14609 USA
Phone: 716/482-0300
Fax: 716/288-5989

© 1993, Applied Image, Inc., All Rights Reserved

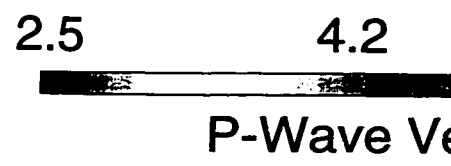
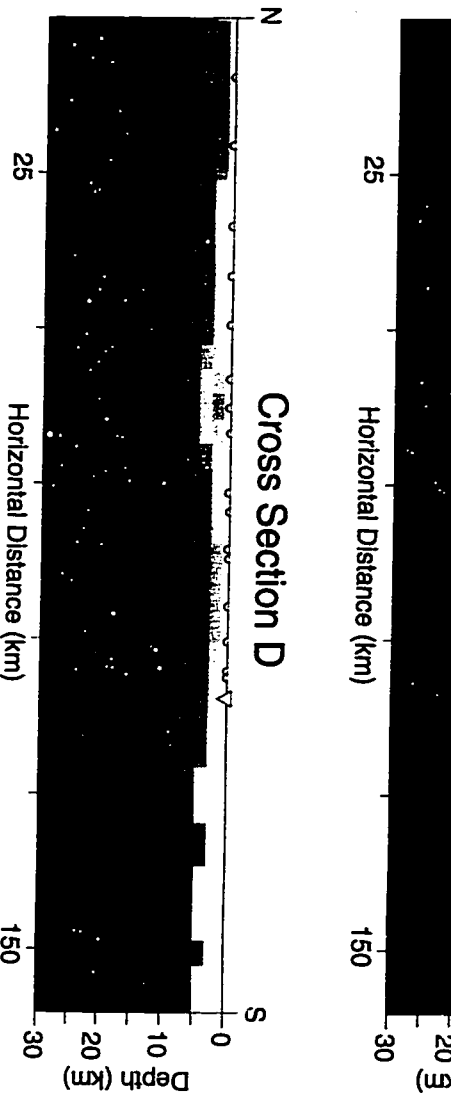
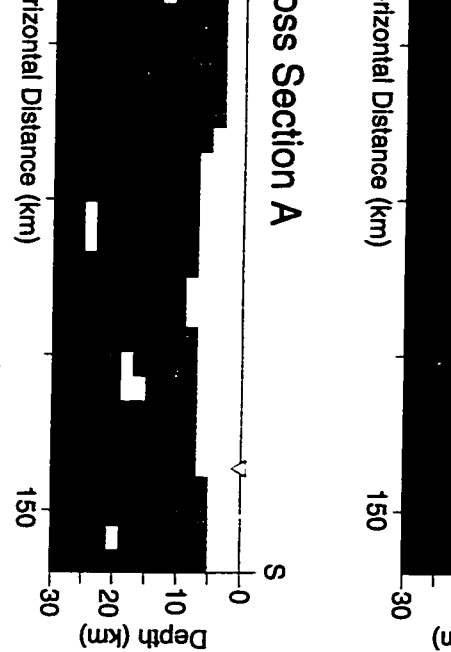


Plate 1: Seven maps
chapter 7. The data
20 explosions from
data has been record

